Studies of Higher Dimensional Black Holes with the ATLAS detector at the LHC

Robindra Prabhu

Department of Physics

University of Oslo

A thesis submitted for the degree of

Candidatus Scientiarum

June 2005

Abstract

In some theories involving extra dimensions and a TeV fundamental Planck scale, miniature black holes may produced at the Large Hadron Collider (LHC). Once produced, these black holes rapidly decay to a spectrum of particles through the Hawking evaporation process. This thesis explores various aspects of black hole production and decay within the context of the ATLAS experiment through a fast simulation study with the `CHARYBDIS` black hole generator. A parton level study is presented to shed light on characteristics of the generator decay model. Signatures of black hole events at the detector level are investigated and described. Finally the black hole hole discovery potential is evaluated using both a simple fixed-temperature, blackbody approximation to the black hole decay and a more refined model with a time-evolving temperature and greybody spectra.

Acknowledgements

This thesis would never appear in its present form without the generous help and support of a number of people.

I am indebted to my supervisors Prof. Farid Ould-Saada and Prof. Lars Bugge who both enthusiastically introduced me to the field and welcomed me to pursue a study on a topic of my own choice. Their continued guidance, support, patience and good spirits have been greatly appreciated.

I would also like to express my gratitude to Prof. Torbjörn Sjöstrand for his continued help and assistance with the interface of `CHARYBDIS` to `PYTHIA`, and to the HEP group at the Niels Bohr Institute for their kind hospitality during my stay there.

I thank the Experimental Particle Physics group at the University of Oslo for generously allowing me to attend several workshops and schools, and for providing me with many opportunities to present my work. All members deserve due recognition for creating a stimulating and friendly atmosphere. I especially thank Dr. Samir Ferrag for the many long hours spent teaching me the tools of the trade, good working habits and for helping me put my work in the right perspective. Dr. Børge K. Gjelsten, who has provided assistance in numerous ways and selflessly spent hours answering my many silly questions with both clarity and depth, also deserves special mention.

A very special thank you to my dear friend Marianne Johansen, who has brought zest and flare to the past few years and made them all the more worth while.

I must also thank my fellow master students Mustafa Hussain and Olav Mundal for the many good moments and witless conversations.

My heartfelt thanks to you all.

Contents

Nomenclature

M_P	Fundamental Planck mass
n	Number of extra dimensions
M_{BH}	Black hole mass
M_{BH}^{min}	Black hole production threshold
M_{BH}^{gen}	Generated black hole mass
M_{BH}^{rec}	Reconstructed black hole mass
M_{BH}^{cut}	Cut-off on reconstructed black hole mass

Preface

This thesis is organised in the following manner. Chapter 1 reviews the theoretical background for the studies presented in the later chapters. The first part provides a brief description of the current leading theory of elementary particles, the so called Standard Model, and highlights some of its shortcomings. The second part introduces a new class of models which, if realised in nature, may solve some of the problems ailing the Standard Model. One possible consequence of these models, is the production of tiny black holes at future colliders. The last part concerns itself entirely with the production and decay of these black holes.

Chapter 2 sets the experimental context for the studies presented in subsequent chapters. It provides a brief description of the Large Hadron Collider and a more extensive description of the ATLAS detector[1].

Chapter 3 describes the simulation tools employed in this thesis. In particular, it describes the black hole production and decay model used by the `CHARYBDIS` black hole event generator. A significant amount of time was spent trying to interface the `CHARYBDIS` black hole generator to the `PYTHIA` Monte Carlo program. This work culminated in the disclosure of a bug in one of the subroutines of `PYTHIA`. The problems encountered and the tests performed are therefore given some mention.

Chapter 4 presents the simulation studies performed after successfully interfacing `CHARYBDIS` to `PYTHIA`. The first part describes the parton level studies undertaken to check the performance of `CHARYBDIS` and to visulalise its black hole decay model. The second part focuses on black hole characteristics and observables in the context of the ATLAS experiment at the LHC. The third part presents an evaluation of the black hole discovery potential. This work is based on (1), but involves the use of an improved black hole generator and an evaluation of the impact of including new effects previously not considered. Finally, the various limitations of analyses are presented are discussed.

[1] This chapter is slightly modified version of term paper written for the course FYS4550.

Chapter 1

Theory

1.1 The Standard Model

The Standard Model (SM) of particle physics provides an exceptionally successful mathematical description of the elementary particles and the interactions between them. The theory seeks to describe matter and forces by way of fundamental point-like particles characterised by a spin quantum number (internal angular momentum) s. Particles are classified as either matter particles or force mediating particles. Matter is composed of $s = \frac{1}{2}$ *fermions*, while the forces between the fermions are mediated by integer spin gauge *bosons*.

The three fundamental forces of the SM include the electromagnetic, weak and strong forces. Electromagnetic interactions occur via massless photon exchange and are reserved for electrically charged fermions. In a similar manner the strong interactions occur only between fermions carrying a colour charge. The force carriers of the strong force are coloured gluons. The weak force is felt by all particles and mediated by three massive gauge bosons: $W^{\pm}$ and Z^0.

The fermions are further divided into quarks and leptons. The quarks represent the only class of fermions sensitive to the strong force and come in six different flavours: up, down, charm, strange, top and bottom. The leptons include three charged particles (the electron, muon and tau) and three corresponding uncharged neutrinos.

The fermionic content of the SM can be grouped in three *families* or *generations*. Each family exhibits similar properties, but differ in mass. Each leptonic

family consists of a charged lepton and its corresponding neutrino. Weak interactions between leptons are restricted to leptons within the same family. Unlike the leptons, the quark mass eigenstates are not eigenstates of the weak force. While a quark will, via the weak force, couple most strongly to its family member, charged weak interactions can occur between generations.

The SM fermions and gauge bosons are listed in Table 1.1 and Table 1.2 respectively.

Leptons			Quarks		
Family	Mass (GeV)	Electric charge	Family	Mass (GeV)	Electric charge
$\begin{pmatrix}\nu_e\\ e\end{pmatrix}$	$< 7 \times 10^{-9}$ 0.000511	0 -1	$\begin{pmatrix}u\\ d\end{pmatrix}$	0.005 0.01	$\frac{2}{3}$ $-\frac{1}{3}$
$\begin{pmatrix}\nu_\mu\\ \mu\end{pmatrix}$	< 0.003 0.106	0 -1	$\begin{pmatrix}c\\ s\end{pmatrix}$	1.5 0.2	$\frac{2}{3}$ $-\frac{1}{3}$
$\begin{pmatrix}\nu_\tau\\ \tau\end{pmatrix}$	< 0.03 1.7771	0 -1	$\begin{pmatrix}t\\ b\end{pmatrix}$	174 4.7	$\frac{2}{3}$ $-\frac{1}{3}$

Table 1.1: The fermionic content of the SM (2).

Interaction	Gauge bosons	Mass (GeV)	Electric charge
Electromagnetic	γ (photons)	0	-1
Weak	$W^{\pm}, Z^0$	80.22, 91.19	$\pm$1,0
Strong	g (gluons)	0	0

Table 1.2: The bosonic content of the SM.

1.1.1 The unbroken Standard Model

At the mathematical level, the SM is a collection of quantum field theories (QFT) where the elementary particles appear as excitations of the quantum fields. The electromagnetic interactions are described by quantum electrodynamics (QED), while quantum chromodynamics (QCD) depicts the strong interactions. Finally the electroweak theory provides a unified account of the electromagnetic and weak forces.

The particle content of the SM is closely connected to the symmetries of the lagrangian describing the physics. The gauge bosons which mediate the forces between fermions secure the invariance of the lagrangian under local gauge transformations such as:

$$\phi(x) \rightarrow \phi^{'}(x) = U(x)\phi(x) \tag{1.1}$$

While the lagrangian of a free fermion is not invariant under such a transformation, its invariance is salvaged by the introduction of vector fields which represent the force mediating gauge bosons.

The unbroken SM is a gauge field theory involving *massless* fermions which interact through three fundamental forces via *massless* vector boson exchange. Associated with each force, is a symmetry of the SM lagrangian. All of the fundamental interactions are described by a gauge theory and the symmetries imposed on the theory "result" in conserved currents and charges. The required number of mediating gauge bosons is precisely the number of generators of the corresponding symmetry group.

There are three principal symmetries of the SM:

- The $U(1)$ hypercharge symmetry is an Abelian symmetry with one gauge field B^{μ}. The associated conserved quantity is the so called *hypercharge* Y.

- The $SU(2)_L$ weak isospin symmetry is a non-Abelian symmetry with three associated gauge fields: W_1^{μ}, W_2^{μ} and W_3^{μ}. These gauge fields couple only to left handed fermions. The conserved charge is the third component of the weak isospin I_3.

- The $SU(3)_C$ is a non-Abelian symmetry of Quantum Chromodynamics (QCD) with eigth associated gauge fields A_a^{μ} (a=1,...,8). The conserved charge is *colour* and the eigth different $SU(3)$ gauge bosons (*gluons*) themselves carry colour charge.

Each of the three SM forces are associated with a local symmetry operation of a particular Lie-group.

The strong force is described in terms of QCD which has a local gauge invariance labelled $SU(3)_C$. The generators of $SU(3)_C$ give rise to eight massless

gluons which couple to quarks with a strength determined by the colour of the particles at a quark-quark-gluon vertex and the strong coupling constant α_s.

The unified electroweak theory is invariant under $SU(2)_L \times U(1)_Y$, where the symmetry group of the electromagnetic force enters as a subgroup of the electroweak sector. The three gauge fields of $SU(2)_L$ and the single generator of $U(1)_Y$ give rise to four mediators of the electroweak interactions.

The SM is then a gauge theory of three independent symmetry groups and is invariant under $SU(3)_C \times SU(2)_L \times U(1)_Y$. The three families of quarks and leptons in the SM each transform identically under these gauge groups. Table 1.3 lists the relevant gauge quantum numbers of the fermionic content of the SM.

The requirements of gauge invariance, Lorentz invariance and renormalizability imposed on all terms of the SM lagrangian leads to two further symmetries and consequently two conserved quantities. Baryon number (B) and lepton number (L) are both conserved by all terms of the SM lagrangian.

Families	Colour	I	I_3	Q	Y
$u_R, \quad c_R, \quad t_R$	$\bar{\mathbf{3}}$	0	0	$\frac{2}{3}$	$\frac{2}{3}$
$d_R, \quad s_R, \quad b_R$	$\bar{\mathbf{3}}$	0	0	$-\frac{1}{3}$	$-\frac{1}{3}$
$\begin{pmatrix} u \\ d \end{pmatrix}_L, \begin{pmatrix} c \\ s \end{pmatrix}_L, \begin{pmatrix} t \\ b \end{pmatrix}_L$	$\mathbf{3}$	$\frac{1}{2}$	$\frac{1}{2}$ $-\frac{1}{2}$	$\frac{1}{6}$	$\frac{2}{3}$ $-\frac{1}{3}$
$e_R \ , \ \mu_R \ , \ \tau_R$	$\mathbf{1}$	0	0	-1	-1
$\begin{pmatrix} \nu_e \\ e \end{pmatrix}_L, \begin{pmatrix} \nu_\mu \\ \mu \end{pmatrix}_L, \begin{pmatrix} \nu_\tau \\ \tau \end{pmatrix}_L$	$\mathbf{1}$	$\frac{1}{2}$	$\frac{1}{2}$ $-\frac{1}{2}$	$-\frac{1}{2}$	0 -1

Table 1.3: Relevant quantum numbers of the SM fermions.

1.1.2 Mass generation

The unbroken SM as described above is clearly incomplete as most particles are experimentally observed to be massive. The different families of quarks and leptons are observed with widely differing masses. Experiments have measured vector boson masses at ∼100 GeV and recently quark masses up to 178 GeV (3).

The addition of fermion and gauge boson mass terms to the unbroken SM lagrangian destroys the gauge invariance and results in non-renormalizable theories.

A remedy is provided through the *Higgs mechanism*, whereby an $SU(2)$ doublet with two complex scalars and a total of four degrees of freedom is added to the theory. This field is known as the Higgs field. If the Higgs field obtains a non-zero expectation value in the vaccuum state, it confers effective masses to most particles through their interactions with it.

The self-interactions of the Higgs field cause spontaneous electroweak symmetry breaking. As a result new mass eigenstates arise as linear combinations of the original gauge eigenstates of the gauge groups

$$W^{\pm} = \frac{(W_{\mu}^{1} \mp iW_{\mu}^{2})}{\sqrt{2}} \tag{1.2}$$

$$\begin{pmatrix} Z^{0} \\ \gamma \end{pmatrix} = \begin{pmatrix} \cos\theta_W \sin\theta_W \\ -\sin\theta_W \cos\theta_W \end{pmatrix} \begin{pmatrix} W_{\mu}^{2} \\ B_{\mu} \end{pmatrix} \tag{1.3}$$

where $\theta_W \equiv \tan^{-1}(g^{'}/g)$ is the Weinberg angle and $g^{'}$ and g are the coupling constants for the $U(1)$ and $SU(2)$ parts respectively.

After the electroweak symmetry breaking, three of the four degrees of freedom of the Higgs doublet field are spent in mass generation for the isosping gauge bosons $W^{\pm}$ and Z^{0}. The remaining degree of freedom gives rise to a massive neutral scalar, the so called Higgs boson ($s = 0$).

The SM fermions acquire their masses through Yukawa couplings to the Higgs field where the coupling is proportional to the mass. Recent experimental investigations suggest that neutrinos have non-vanishing masses ($\sim$few eV)(4; 5). Although the SM as described above renders the neutrinos massless, there are several ways of incorporating neutrino masses and neutrino mixing into the SM lagrangian.

The Higgs boson is the only SM particle which remains undetected. Particle masses are free parameters of the SM, as is the mass of the Higgs boson. Unitarity arguments related to the $W^{+}W^{-} \rightarrow W^{+}W^{-}$ scattering amplitude, place an upper limit on the Higgs mass of $m_H \sim$1 TeV. Direct experimental searches provide a lower bound of $m_H > 114.4$ GeV (95% CL). Loop corrections to the Higgs mass

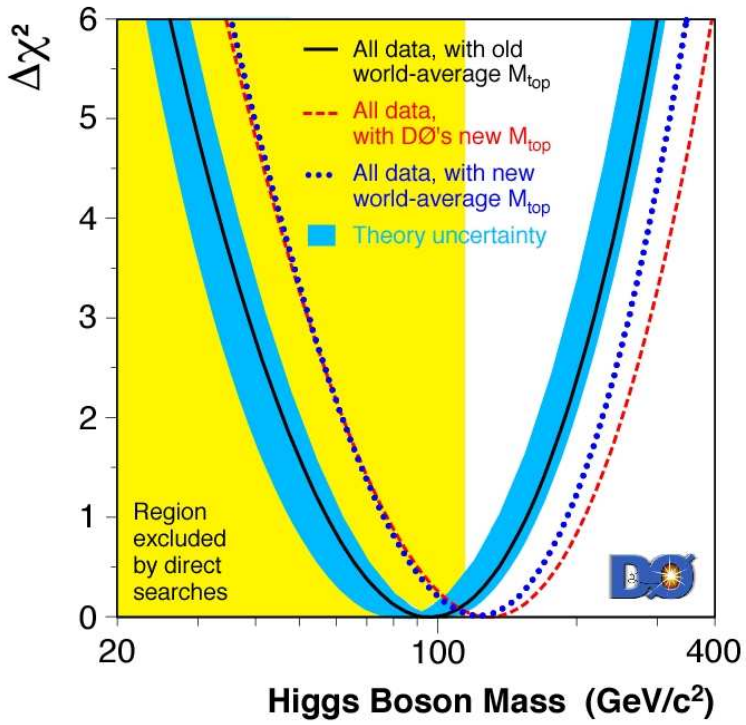

Figure 1.1: The $\Delta\chi^2$ global electroweak precision fit as a function of the Higgs mass. The vertical band indicates the region excluded by experiment (114.4 GeV at 95% CL). The dotted line shows the results with the improved top mass measurement ($m_t = 178.0 \pm 4.3$ GeV), and is seen to shift the most probable higgs mass out beyond the experimentally excluded region. Obtained from (3).

are sensitive to electroweak observables. Global fits to electroweak precision data favour a low Higgs mass. A recent electroweak precision fit (3), which favours a Higgs mass of 117 GeV, is shown in Figure 1.1. A central task of the LHC programme will be to search for this particle across the entire energy range.

1.1.3 Shortcomings of the Standard Model and new physics beyond

Although the SM has been extensively tested and found to agree with all confirmed experimental data, there are several reasons to believe that it is merely an effective theory restricted to a specific energy regime and not an ultimate theory

of fundamental interactions. Some of the shortcomings of the SM that motivate the search for new physics beyond the SM are briefly outlined below:

- The SM has at least 19 free parameters, whose value the theory offers no prediction, and which can only be determined through empirical investigations. These include the quark, charged lepton and weak boson masses $(6 + 3 + 2)$, the gauge couplings of the SM forces (3), the Cabibbo weak mixing angles (3) and the CP-violating parameters (2)[1].

- The SM fails to explain why there are precisely three families of quarks and leptons, as well as why the weak interactions mix in the peculiar way observed. The SM does not explain the origin of QCD confinement[2], nor the observed asymmetry between matter and antimatter in the universe.

- In order to unify the strong and electroweak interactions in a single gauge theory, the three associated gauge couplings must unify into a single value α_G. Beyond this unification scale all interactions will occur by way of a single force with strength α_G. So called *Grand Unified Theories* (GUT) predict that such a unification will occur at $\sim 10^{16}$ GeV. The particle content of a model determine the evolution of the gauge couplings with increasing energy. As shown in Figure 1.2, the SM couplings fail to unify, when extrapolated from experimental measurements to higher energies. Additional particle content (*e.g* as predicted by SUSY) or other new physics may serve to modify the running of the couplings to successfully achieve unification.

- Gravity is entirely emitted from the SM theory of fundamental interactions. At energies ~ 100 GeV, gravity can be safely neglected in a description of fundamental interactions on account of being orders of magnitude weaker than the SM forces. However, at the Planck scale $M_P \sim 10^{19}$ GeV, the effects of gravity can no longer be ignored and particle interactions must be described by a theory of quantum gravity. At high energies, the SM will therefore break down and need to be replaced by an alternative theory which includes a description of quantum gravity.

[1] Nine additional parameters must be introduced to account for neutrino oscillations.
[2] comment on quark-gluon plasma

- There appears to be a hierarchy of mass scales in particle physics. The electroweak mass scale ($M_W \sim 100$ GeV) of the SM is separated by orders of magnitude from the scale of gravity, the Planck scale ($M_P \sim 10^{19}$ GeV). In a fundamental theory all the mass scales would be expected to be of the same order. The question then arises as to why $M_W \ll M_P$, or alternatively why gravity is weak in comparison to the other gauge forces? This problem is commonly known as the *hierarcy problem*.

  The hierarchy problem originates in one-loop corrections to the higgs mass. Within the SM, such radiative corrections arise from quadratically divergent diagrams such as those shown in Figure 1.3. In order to regulate the divergences, a cutoff Λ is introduced in the loop momentum integral. The cutoff may be interpreted as the scale at which the SM breaks down and new physics becomes important. The one-loop corrections to the higgs mass squared are quadratically proportional to the cutoff of the theory:

$$\delta m_H^2 = \mathcal{O}(\Lambda^2) + \mathcal{O}(\ln \Lambda) + ... \tag{1.4}$$

  That is to say, that quantum corrections to m_H^2 are quadratically dependent on the mass scale of an underlying, more fundamental theory. The Planckian energy regime marks the entry of quantum gravity and the reduction of the SM to an effective field theory. If $\Lambda \sim M_P$, then the *bare* higgs mass would be forced to the same scale. However, if the Higgs mechanism is responsible for electroweak symmetry breaking, then the mass of the higgs boson should be related to the electroweak mass scale $M_W \sim 100$ GeV, as indicated by Figure 1.1. In order to reproduce a higgs mass of $m_H \sim 100$ GeV, the bare higgs mass would have to be precisely tuned to an accuracy of one part in 10^{16}.

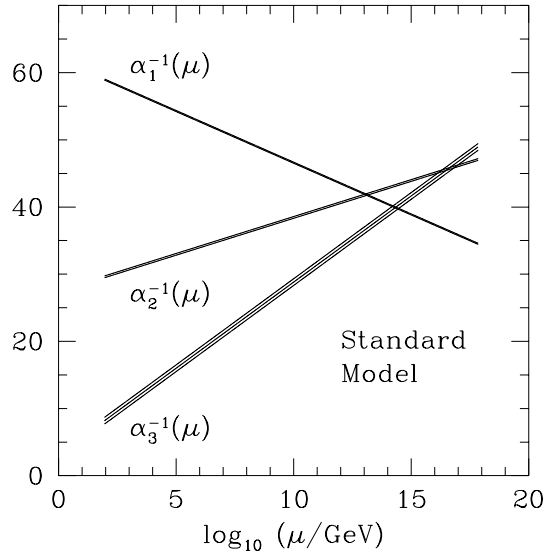

Figure 1.2: Evolution of the running gauge couplings of the SM (6).

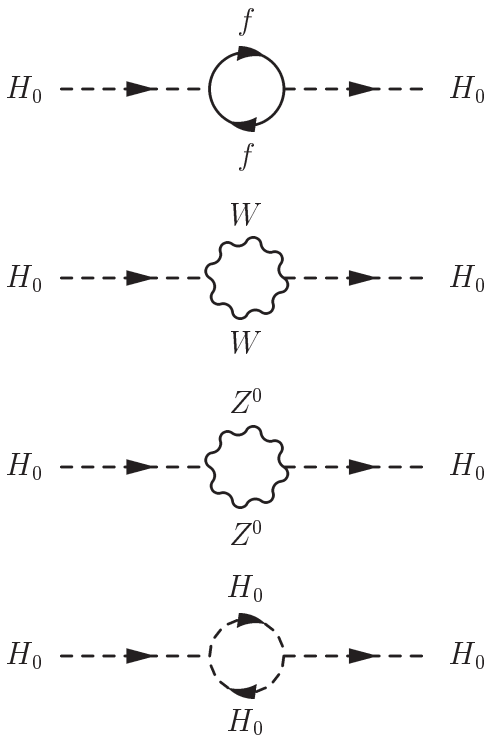

Figure 1.3: Feynmann diagrams for the loop corrections to the bare Higgs mass.

1.2 Extra Dimension Models

The recent years have seen a surge of interest in various models involving extra spatial dimensions. While the various models differ in their makeup, they all provide solutions to the hierarchy problem by invoking the geometry of spacetime whereby the presence of extra dimensions are believed to explain the large hierarchy between the electroweak and Planck scales. Although a wealth of different models have been constructed, most share some characteristic common features.

The SM and other non-gravitational fields are confined to a four-dimensional submanifold (*brane*) of the higher-dimensional spacetime (*bulk*)[1]. Gravitons are typically not constrained to the brane and are free to propagate throughout the higher-dimensional volume. At distances smaller than the size of the extra dimensions, gravity no longer abides by the Newtonian inverse-square force law. In order to recover the three-dimensional inverse-square law at distances larger than the size of the extra dimenions, the additional dimensions are usually compactified to small sizes. The compactification of the extra dimensions also serve to explain why they have escaped detection at earlier experiments.

The history of extra dimension models is usually traced back to the 1920's when T. Kaluza and O. Klein proposed a scheme to unify classical electromagnetism and general relativity by invoking one additional compactified dimension[2]. Failing to incorporate the quantum theories of QED and QCD, Kaluza-Klein (KK) theories fell into disinterest. In recent years however, extra dimension models have been revived and attracted considerable interest as alternative solutions to the hierarchy problem with intriguing potential experimental signatures at the TeV scale.

Extra dimension models can also be motivated by *superstring theory*. Superstring theory (ST) has emerged as the most promising candidate for a consistent theory of quantum gravity and involves 10 spatial dimensions, 6 of which are

[1] There are models in existence where the SM fields are not localised on the brane.

[2] Before the advent of General Relativity, G. Nordström tried to unify Newtonian gravity and classical electromagnetism in a five-dimensional theory of electromagnetism. In this scheme the fifth component of the vector potential was identified with the gravitational scalar potential. By contrast, the KK photon is a component of the higher-dimensional graviton.

compactified on small scales. In addition to strings, ST also predicts the existence of non-perturbative, higher-dimensional extended objects called Dirichlet branes (D-branes) which define the allowed set of endpoints of open strings. ST easily accomodates the localisation of SM fields on 3-branes and the hierarchy of scales: SM fields are represented by open strings with endpoints fixed to a brane. Gravitons, by contrast, are described by closed strings free to propagate in all spatial dimensions[1].

Different compactification models vary by way of size and geometry of the extra dimensions. Similarly the precise particle content confined to the brane or free to propagate throughout the higher-dimensional volume, differs from model to model. The many scenarios proposed to date may be categorised according to whether the $(4+n)$-metric (where $\mu, \nu = (0, ..., 3)$ and $i, j = (4, ..., n-1)$)

$$ds^2 = g_{ab}(x)dx^a dx^b = e^{2A(y)}dx^\mu dy^\nu \eta_{\mu\nu} + h_{ij}(y)dy^i dy^j \tag{1.5}$$

is factorizable ($A(y) = 0$) or not ($A(y) \neq 0$).

The principal extra dimension scenarios include *large extra dimensions* and *warped extra dimensions*. The work presented in this thesis is performed within the framework of the ADD model with large extra dimensions. This theory is outlined in further detail in Section 1.2.2.

1.2.1 Kaluza-Klein Theories

Before presenting the ADD model with large extra dimensions, it is instructive to first study a generic feature of theories with compactified extra dimensions.

Consider the simplest case of one additional dimension compactified on a circle of radius R such that the higher-dimensional coordinates satisfy the periodic identification $y = y + 2\pi R$.

The action of a massive scalar field $\Phi(x^\mu, y)$ is

$$S = \frac{1}{2}\int \mathcal{L} d^5x = \frac{1}{2}\int \Phi(x^\mu, y)(\Box_5 + m^2)\Phi(x^\mu, y)d^5x \tag{1.6}$$

[1] Although extra dimension models can be included in ST, they should be regarded as independent theories.

where $\Box_5$ is the five-dimensional d'Alembert operator

$$\Box_5 = \frac{\partial^2}{\partial x_0^2} - \frac{\partial^2}{\partial x_1^2} - \frac{\partial^2}{\partial x_2^2} - \frac{\partial^2}{\partial x_3^2} - \frac{\partial^2}{\partial y^2} \tag{1.7}$$

and Φ obeys the periodic boundary condition $\Phi(x^\mu, y) = \Phi(x^\mu, y + 2\pi R)$. Expanding the field in a Fourier series over the compactified dimension

$$\Phi(x^\mu, y) = \sum_{n\in\mathbb{N}} \phi_n(x^\mu)\chi_n(y) \tag{1.8}$$

where $\chi_n(y) = e^{iny/R}$ are the orthonormalized eigenfunctions of $\frac{\partial^2}{\partial y^2}$ acting on the compactified dimension[1],

$$\frac{\partial^2}{\partial y^2}\chi_n(y) = -\frac{n^2}{R^2}\chi_n(y) \tag{1.9}$$

inserting in Equation 1.6 and integrating over y, one obtains an effective four-dimensional action:

$$S = \frac{1}{2}\int d^4x \sum_{n\in\mathbb{N}} \phi_n(x^\mu)\left(\Box_4 + m^2 + \frac{n^2}{R^2}\right)\phi_n(x^\mu) \tag{1.10}$$

The action 1.10 describes a tower of states of increasing masses

$$m_n^2 = m^2 + \frac{n^2}{R^2} \tag{1.11}$$

with a mass splitting $1/R^2$ determined by the compactification radius of the extra dimension. Much like a particle in a box, the momentum of the field propagating in the bulk is quantized in the compactified dimension

$$\vec{p_5}^{\,2} = \frac{\bar{n}\cdot\bar{n}}{R^2} \tag{1.12}$$

such that from the perspective of an observer on the brane the set of allowed momenta in the compactified dimension apppears as a tower of massive KK excitations of the propagating field. From the five-dimensional perspective however, there is only *one* state of mass m.

[1] $\int dy \chi_m \chi_n = \delta_{m,n}$

1.2.2 Large Extra Dimensions (ADD models)

Models with large extra dimensions constitute perphaps the earliest and simplest class of extra dimension models. They are often called ADD models after N. Arkani-Hamed, S. Dimopoulos and G. Dvali who in 1998 spawned new interest in extra dimensions by proposing a novel solution to the hierarchy problem by way of a mechanism which served to reduce the Planck scale to the electroweak scale (7).

The original ADD proposal involved n toroidally compactified extra dimensins with radius R[1]. The SM fields are localised on a four dimensional brane embedded in a higher-dimensional spacetime and only the gravitational field is free to propagate in the bulk. The presence of n compact extra dimensions serve to modify classical gravity and alleviate the hierarchy between the electroweak and Planck scales.

The ADD mechanism is perhaps best illustrated by considering the gravitational force between two point masses, m_1 and m_2, separated by a distance r. If the separation between the point masses is smaller than the compactification radius ($r \ll R$) of the extra dimensions, then application of Gauss' Law in (4+n) dimensions gives the potential

$$V(r) = -G_{(4+n)} \frac{m_1 m_2}{r^{n+1}} \tag{1.13}$$

where G_{4+n} is the (4+n) dimensional gravitational constant. For large distances ($r \gg R$) the traditional Newtonian potential

$$V(r) \sim -\frac{G_{(4+n)}}{R^n} \frac{m_1 m_2}{r} = -G_4 \frac{m_1 m_2}{r} \tag{1.14}$$

is recovered, where R^n is the volume of the compactified n-dimensional manifold and G_4 is the effective four-dimensional gravitational constant

$$G_4 \sim \frac{G_{(4+n)}}{R^n} \tag{1.15}$$

Equation 1.15 clearly suggests that the weakness of gravity may be understood as a "leakage" into a bulk space of volume R^n. Rewriting equation 1.15 in terms

[1] This is tantamount to assuming a flat metric for the higher-dimensional space.

of the four-dimensional Planck mass $M^2_{P(4)} = (G_{(4)})^{-1} = (1.2 \times 10^{19}\ \text{GeV}\ )^2$ and a fundamental mass scale of the higher-dimensional theory $M^2_{P(4+n)} \equiv (G_{(4+n)})^{\frac{-2}{n+2}}$, one obtains

$$M^2_{P(4)} \sim R^n M^2_{P(4+n)} \tag{1.16}$$

which relates the effective four-dimensional Planck mass to the *fundamental* Planck mass $M_{P(4+n)}$ of the higher-dimensional theory. Relation 1.16 explictly shows that if the extra dimensions are sufficiently large as compared to the fundamental Planck mass, the latter may be as low as the electroweak scale. The ADD mechanism is thus seen to trade the hierarchy of scales by a new hierarchy in extra dimensions[1]

The experimental bounds on the size of the extra dimensions strongly depend on whether the SM fields are confined to brane or free to propagate in the bulk. If the latter be the case, then $R < 1\ \text{TeV}^{-1}$ as no signatures of extra dimensions have been observed at present or past accelerator experiments. If however, only gravity is free to access the higher-dimensional volume, direct test of the gravitational force at small distances permit extra dimensions as large as $R < 0.1$ mm. The size of the extra dimensions as a function of the number of extra dimensions is listed in Table 1.4, assuming $M_{P(4+n)} \sim M_W \sim 1$ TeV.

Table 1.4 indicates that the case of n=1 is clearly ruled out on account of yielding compactification radii comparable to the solar distance. Higher values of n (> 2) cannot just as easily be ruled out as direct tests of gravity have only probed distances down to $r \sim 10^{-4}$m. Experimental constraints on large extra dimensions are discussed in greater detail in Section 1.2.3.

1.2.3 Experimental limits on large extra dimensions

Current experimental bounds on the fundamental Planck mass $M^{n+2}_{P(4+n)}$ are derived from short-range tests of the gravitational force law, collider experiments

[1] This is arguably only a reformulation of the hierarchy problem. To fully resolve the hierarchy problem, an explanation would be required as to why the bulk has the precise volume that it has.

n	R [m]
1	$\sim 10^{13}$
2	$\sim 10^{-3}$
3	$\sim 10^{-8}$
4	$\sim 10^{-11}$
5	$\sim 10^{-12}$
6	$\sim 10^{-13}$
7	$\sim 10^{-14}$

Table 1.4: The approximate size of extra dimensions as a function of the number of extra dimensions assuming $M_{P(4+n)} \sim 1$ TeV.

and various astrophysical and cosmological considerations. Among these, the latter provide the most stringent constraints, but with large systematic errors. The collider limits are milder and more accurate.

The aim of this section is to briefly comment on recent experimental constraints on the ADD model. More exhaustive overviews of constraints on extra dimension models are provided in (8),(9),(6) and (10). (All values in this section are taken from (10)).

1.2.3.1 Limits from tests of the gravitational force law

Deviations from the four-dimensional inverse-square law of Newtonian gravity are expected at distances smaller than the compactification radius of the extra dimensions. Torsion-balance experiments performed by the EÖT-WASH collaboration have found no deviations from Newton's inverse-square down to distances of 150 μm.

In the conventions of this thesis (see Appendix), this results in a lower bound of $M^{2+2}_{P(4+2)}$ >1.5 TeV. For higher values of n, the extra dimensions become increasingly small and are consequently rendered inaccessible to mechanical experiments. At small scales gravity ceases to be the dominant force and gives way to contributions form Casimir forces, van der Waals forces, etc.

1.2.3.2 Limits from astrophysics and cosmology

Astrophysical and cosmological considerations provide the most stringent bounds on the fundamental Planck mass.

The emission of KK graviton modes in astrophysical processes are expected to affect the evolution of supernovae and neutron stars.

The graviton bulk emission rate must not be such as to violate the observed cooling rates of supernovae remnants. Observations of supernova SN1987A place constraints on the fundamental Planck mass listed in Table1.5

	n=2	n=3	n=4
$M_{P(4+n)}^{n+2}$	$\geq$45 TeV	$\geq$3 TeV	$\geq$ 1 TeV

Table 1.5: Limits on the fundamental Planck mass from the cooling of supernova SN1987A.

Large systematic errors accompany these estimates, the principal uncertainty being associtated with the temperature of the remnant core.

Massive KK-gravitons are also produced in the formation of neutron stars through the collapse of a supernova core. The collapse leaves behind a neutron star halo of gravitationally trapped KK-gravitons which decay into e^+e^-, $\gamma\gamma$ and $\nu\bar{\nu}$. These decay products in turn heat the neutron star through collisions. The requirement that neutron stars are not excessively heated by the decay particles of trapped KK-modes, places stringent bounds on the fundamental Planck mass. These bounds are listed in Table1.6

	n=2	n=3
$M_{P(4+n)}^{n+2}$	$\geq$1300 TeV	$\geq$30 TeV

Table 1.6: Limits on the fundamental Planck mass from neutron star surface temperatures.

KK gravitons produced in astrophysical processes may decay into SM particles, where $G \rightarrow \gamma\gamma$ is the favoured decay mode for low-mass KK-modes. Measurements of the cosmic diffuse gamma ray background by the EGRET and COMPTEL collaborations, indicate that the total energy emitted into gravitons

must not exceed ∼1% of the total energy emitted by all supernovae in the history of the universe. These considerations place bounds on the fundamental Planck mass listed in Table1.7

	n=2	n=3
$M_{P(4+n)}^{n+2}$	≥60 TeV	≥3 TeV

Table 1.7: Limits on the fundamental Planck mass from the cosmic diffuse gamma ray background.

ADD models facilitate black hole production at TeV energies. High-energy cosmic rays could potentially produce black holes through high energy collisions with nuclei in the atmosphere of the Earth, their subsequent decay to energtic showers detectable at ground based experiments. The nonobservation of such black hole events by the AGASA experiment have placed the limits $M_{P(4+n)}^{n+2}$ ≥0.4-0.6 TeV in the case of $n = 5$.

1.2.3.3 Limits from colliders

Searches for real graviton production provide lower bounds for the fundamental Planck mass. Such searches have been performed at the LEP, Tevatron and HERA colliders.

Even though the graviton coupling is small ($\sim 1/\sqrt{M_{P(4)}}$), the abundance of KK-modes at collider energies render graviton emission processes such as

$$e^+e^- \to \gamma/Z + G$$

$$q\bar{q} \to g + G$$

$$Z \to f\bar{f} + G$$

detectable where the graviton appears as missing energy in the detector.

The best limits from the L3 collaboration at LEP and CDF experiment at the Tevatron are listed in Table1.8.

Experiment	n=2	n= 4	n=6
L3 (LEP)	>1.3 TeV	>0.46 TeV	>0.25 TeV
CDF (Tevatron)	>0.95 TeV	>0.4 TeV	>0.28 TeV

Table 1.8: Limits on the fundamental Planck mass from collider experiments.

1.3 Higher-dimensional black holes

If extra dimension models are realised in nature and the fundamental Planck mass is suffiently low ($M_{P(4+n)} \approx 1$ TeV), the LHC will provide collision energies far in excess of $M_{P(4+n)}$. Amongst others, an exciting, plausible consequence is the production of tiny black holes. Such black holes are higher-dimensional quantum-scale objects and are somewhat different from their astrophysical analogues. The following sections describe the production and decay mechanisms of black holes at the LHC. (Most of the information is drawn from (6; 11; 12) and more thorough reviews can be found therein).
In this Section and throughout the remainder of this thesis, the fundamental Planck mass $M_{P(4+n)}$ will be denoted simply by M_P.

1.3.1 Transplanckian scattering and black hole production

If the fundamental Planck mass is sufficiently low, the LHC will enter the planckian energy regime and probe quantum gravity. An understanding of the planckian processes can only be attained throught a complete theory of quantum gravity. To date, such a theory is sadly lacking.

It is possible, however, to provide descriptions of gravitational effects in the *cisplanckian*($\sqrt{s} < M_P$) and *transplanckian* ($\sqrt{s} \gg M_P$) regions using model-independent general principles (13).

In the cisplanckian regime, single graviton emission provides a model-independent handle on graviton propagation in extra dimensions. The theory is described by an effective field-theory and graviton emission can be treated with perturbation theory.

Transplanckian collisions are believed to lend themselves to semi-classical treatment. A simple dimensional analysis (in units where $c = 1$ and $\hbar \neq 1$) may be considered to illustrate this characteristic of transplanckian kinematic regime (13; 14). Using the relation between the higher-dimensional Newton constant $G_{(4+n)}$ and the fundamental Planck mass

$$M_P^{n+2} \sim \frac{\hbar^{n+1}}{G_{(4+n)}} \tag{1.17}$$

the Planck length

$$\lambda_P^{n+2} \sim \frac{\hbar}{G_{(4+n)}} \tag{1.18}$$

can be constructed. The Planck length λ_P marks the distance below which the effects of quantum gravity become non-negligible. Similarly, the de Broglie wavelength

$$\lambda_B \sim \frac{\hbar}{\sqrt{s}} \tag{1.19}$$

specifies the quantum mechanical length scale of the particles colliding with center of mass energy $\sqrt{s}$. The Schwarzschild radius associated with this collision energy

$$r_S \sim (G_{(4+n)}\sqrt{s})^{\frac{1}{n+1}} \tag{1.20}$$

indicates the length scale where curvature effects become important. Two observations can now be made in the limit $\hbar \to 0$, keeping $G_{(4+n)}$ and $\sqrt{s}$ constant. Firstly, transplanckian energies ($\sqrt{s} \gg M_P$) are macroscopic and seen to relate to the classical limit because $M_P \to 0$. Secondly, r_S is found the be the scale that characterizes the dynamics in this regime, while λ_P and λ_B are both seen to vanish. The transplanckian regime is therefore essentially described by (semi-)classical general relativity, and insofar may provide a model-independent handle on large extra dimensions.

Physics in the transplanckian energy regime will depend on the parameter r_S/b, where b is the impact parameter of the collision. Collision with $b \gg r_S$ will result in gravitational elastic scattering, giving dijet events close to the beam with large center of mass energy (13). Such processes may be treated in the eikonal approximation, however this approximation breaks down when $b \sim r_S$ (14). In this regime gravity become strong and curvature-effects are non-negligible. No

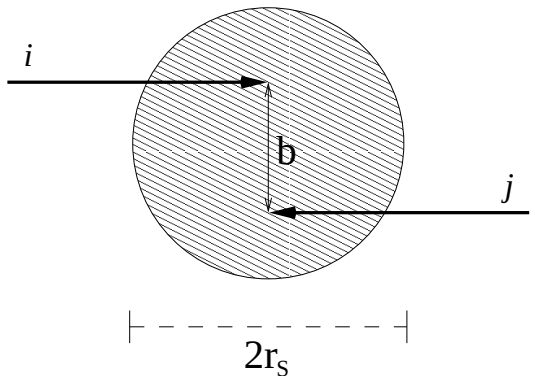

Figure 1.4: Schematic illustration of the black hole formation process. Two particles/partons i and j pass within the horizon associated with the collision energy $\sqrt{s}$. If the impact parameter is small $b < r_S$ a black hole will form.

exact solution is currently available for this regime. However, plausibility arguments suggest that collisions where $b \leq r_S$ are expected to result in gravitational collapse and black hole formation, because the initial state with energy $\sqrt{s}$ is trapped behind a radius r_S. Black hole formation is a generic nonperturbative feature of any theory involving gravity.

1.3.1.1 Black hole production

The colliding particles are typically described by two incoming gravitational shock waves with impact parameter b. In the limit where the speed of the particles approaches the speed of light, the particles are massless and curvature effects are negligible before and after shocks. The geometry is then examined for trapped surfaces (15).

Since the transplanckian black hole formation process is semi-classical, the cross-section is given by the geometric cross section of an absorptive black disk of radius r_S[1]:

$$\sigma_{ij\to BH}(s;n) = F_n(s)\pi r_S^2 \tag{1.21}$$

[1]The cross section is simply taken as the effective target area defined by the impact parameter b: $\sigma \sim \pi b^2 \sim \pi r_S^2$

as illustrated in Figure 1.4. Here, $F_n(s)$ is a dimensionless form factor of order $\mathcal{O}(1)$[1] which reflects the theoretical uncertainties related to the dynamics of the black hole production process, such as the amount of the collision energy $\sqrt{s}$ captured behind the horizon, the black hole mass distribution as a function of $\sqrt{s}$ and corrections to the geometrical cross-section (16). In this thesis, these corrections are neglected and $F_n(s)$ is set to unity.

Black hole production at the LHC would necessarily involve composite colliding particles, and the cross section must therefore involve a sum over all parton pairs carrying a sufficient fraction of the center of mass energy $\sqrt{s}$ to produce a black hole of lower mass M_{BH}^{min}:

$$\sigma_{pp\to BH(\tau_m,s)} = \sum_{i,j} \int_{\tau_m}^{1} d\tau \int_{\tau}^{1} \frac{dx}{x} f_i(x) f_j(\frac{\tau}{x}) \sigma_{ij\to BH}(\tau s) \tag{1.22}$$

Here, $f_i(x)$ are the parton distribution functions (see 2.1), $\tau = x_i x_j$ is the parton-parton center of mass energy squared fraction and $\sqrt{\tau_m s}$ is the minimum center of mass energy required for creation of the minimum black hole mass $M_{BH}^{min} \simeq \sqrt{\tau_m s}$ (for which the semi-classical cross-section is valid).

The black hole cross sections in Equations 1.21 and 1.22 merit some comments. Unlike cross sections of perturbative physics which decrease like $1/s$, the black hole cross section grows with center of mass energy. The event horizon forms before the partons come in causal contact and perturbative hard scattering processes are therefore hidden behind the horizon. Finally, the sum over parton pairs in Equation 1.22 does not discriminate between different particles types or flavours and enhances the black hole cross section greatly with respect to pertubative Standard Model processes. If M_P=1 TeV, proton-proton scattering at the LHC yields production cross sections of $\sim 10^5$ fb for M_{BH}^{min} =5 TeV (11). This relatively large cross section is comparable to that of $t\bar{t}$ event.

1.3.2 Properties of higher-dimensional black holes

In the absence of extra dimensions, the creation of semi-classical black holes requires such enormous center-of-mass energies that their production is rendered

[1] $F_0 = 0.647, F_7 = 1.883$ (6)

far beyond the technical capabilities of any accelerator experiment. The presence of extra dimensions however, facilitates black hole production in a two fold way; on the one hand by lowering the scale of quantum gravity and on the other by providing a larger Schwarzschild radius r_S for a given center of mass energy $\sqrt{S}$, thereby improving access to the black hole creation regime $b \leq r_S$.

In what follows, the treatment of higher-dimensional black holes will make use of two simplifying assumptions. Firstly that the Schwarzschild radius is smaller than the size of the extra dimensions $r_S \ll R$, such that the black hole is completely submerged in the higher dimensional spacetime. Secondly, that the black holes resulting from parton collisions are non-spinning (spherically symmetric). Such a higher-dimensional black hole would be surrounded by a gravitational background given by the generalized Schwarzschild line-element

$$ds^2 = \left(1 - \left(\frac{r_S}{r}^{n+1}\right)\right) dt^2 - \left(1 - \left(\frac{r_S}{r}^{n+1}\right)\right)^{-1} dr^2 - r^2 d\Omega_{2+n}^2 \tag{1.23}$$

where n is the number of extra dimensions and $d\Omega_{2+n}^2$ is the area of the (2+n)-dimensional unit sphere

$$d\Omega_{2+n}^2 = d\theta_{n+1}^2 + \sin^2\theta_{n+1}(d\theta_n^2 + \sin^2\theta_n(... + \sin^2\theta_2(d\theta_1^2 + \sin^2\theta_1 d\varphi^2)...)) \tag{1.24}$$

with $0 < \varphi < 2\pi$ and $0 < \theta_i < \pi$ for $i = 1, ..., n+1$.

The Schwarzschild radius of a higher-dimensional black hole, may then be found by extending the four-dimensional calculation into the (4+n)-dimensional spacetime using Gauss' law:

$$r_S = \frac{1}{\sqrt{\pi} M_P} \left(\frac{M_{BH}}{M_P}\right)^{\frac{1}{n+1}} \left(\frac{8\Gamma(\frac{n+3}{2})}{n+2}\right)^{\frac{1}{n+1}}. \tag{1.25}$$

Clearly the presence of extra dimensions ($n \neq 0$) renders the relation between the Schwarzschild radius r_S and the black hole mass M_{BH} non-linear. The radius is also larger in $n \neq 0$ than it is in $n = 0$. It is the presence of the fundamental Planck mass M_P in Equation 1.25, rather than the four dimensional Planck mass $M_{P(4)}$ which allows for the production of low-mass black holes.

In (11) it is shown that for $M_P = 1$ TeV, a 5 TeV black hole will have a size $r_S \sim 10^4$ fm. That is to say that a parton collision with center of mass energy $\sqrt{\hat{s}} \geq 5$ TeV will result in black hole formation, provided the partons collide within a distance of $\sim 10^4$ fm, a sub-nuclear distance well within the reach of the LHC.

The properties of (4+n)-dimensional, spherically symmetric Schwarzschild black holes differ somewhat from their four dimensional counterparts. The Hawking temperature

$$T_H = \frac{(n+1)}{4\pi r_S} \tag{1.26}$$

is inversely related to the Schwarzschild radius r_S and hence much lower in $n \neq 0$ than it is in $n = 0$. A black hole with temperature T_H emits thermal radiation and decays through the emission of ordinary particles. The radiation spectrum for this decay is roughly that of a blackbody peaking at energies close to its temperature. LHC black holes are expected to have temperatures of the order of a few hundred GeV.

The rate of the black hole decay increases with the black hole Hawking temperature and high temperatures correspond to a short lifetimes. However, the lifetime of higher-dimensional black holes

$$\tau \sim \frac{1}{M_P}\left(\frac{M_{BH}}{M_P}\right)^{\frac{(n+3)}{n+1}} \tag{1.27}$$

is extended by a low-scale M_P, making them more long-lived than four-dimensional black holes of equal mass.

All in all, higher-dimensional black holes are larger (greater r_S), colder (lower T_H) and have longer lifetimes than their four-dimensional counterparts.

Even so, higher-dimensional black holes with masses of a few TeV have lifetimes of just $\mathcal{O}(10^{-26})$sec, thus decaying instantaneously on LHC detector timescales. The black hole decay process is discussed in greater detail in Section 1.3.3

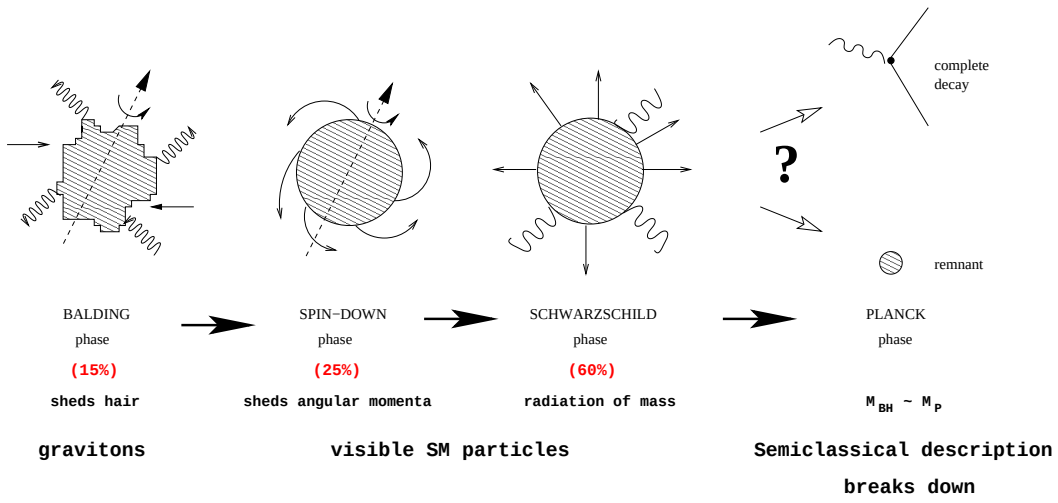

Figure 1.5: The different phases of the black hole decay.

1.3.3 Decay of Higher-dimensional Black Holes

1.3.3.1 Decay Phases

The decay process is assumed analogous to that of four-dimensional black holes and takes place in a series of different phases (12), each of which is given brief mention below.

1. *Balding Phase*
   Initially, the excited black hole state will carry gauge quantum numbers inherited from the incoming parton pair. Furthermore, the inital horizon is very asymmetric as consequence of the violent production process. In a brief balding phase the black hole sheds 'hair' (multipole momenta) inherited from the black hole forming partons and the asymmetry resulting from the violent production process, chiefly through the emission of gravitational radiation. In four dimensions the mass loss by way of gravitational radiation in the balding phase is estimated at $\sim 16\%$ (11) [1]. After balding, when the black hole has shed most of its 'hair', it is described by a spinning Kerr solution in terms of its mass and angular momentum.

[1] This estimate can increase significantly depending on the value of the impact parameter and the dimensionality of spacetime (11).

2. *Spin-down Phase*
   Since the incoming partons typically collide with non-zero impact parameters the resulting black hole will carry angular momentum directed perpendicularly to the collision axis. During the spin-down phase the black hole sheds angular momenta by Hawking radiating Standard Model particles on the brane. In four dimensions the spin-down phase is estimated to account for some 25% of the total mass loss (11). At the end of the phase, the black hole state is described by a non-rotating spherically symmetric Schwarzschild solution.

3. *Schwarzschild Phase*
   After the spin-down phase the decaying black hole (**J=0**) enters the Schwarzshild phase wherein it continues to lose mass by Hawking emission of SM particles. As the black hole decays, its mass gradually decreases while its characteristic Hawking temperature increases. Since the radiation spectrum peaks around the Hawking temperature, it is expected that later emission will typically be of higher energy than earlier emissions. The Schwarzschild phase is the longest of the decay phases and is expected to account for the majority of the mass loss (60%) (11).

4. *Planck Phase*
   Once the mass of the black hole (and/or its temperature) approaches the fundamental Planck scale $M_{BH} \sim M_P$ the semi-classical description breaks down and the properties of the black hole become complex and "stringy". A full-fledged theory of quantum gravity is required to fully understand the terminal stages of the black hole decay. However it has been argued that upon approaching the fundamental Planck mass the black hole will decay completely through the emission of a few quanta of the order of the Planck scale (12). Alternatively a stable relic may form (15).

The various phases of the black hole decay are schematically shown in Figure 1.5. It is important to note that the above mass loss estimates for the different decay phases are all derived in four dimensions. In higher-dimensional spacetime

these figures may alter significantly[1]. Further analyses are required to shed light on the nature of the decay of higher-dimensional black holes.

Another point of interest is the relative proportion of emission to the bulk and to the brane. In (17) it is argued the black hole decays primarily to modes on the brane. Since the wavelength corresponding to the Hawking temperature is larger than the size of the black hole ($\lambda = \frac{2\pi}{T_H} = \frac{8\pi^2}{n+1} r_S$), the black whole may be viewed as a point radiator emitting mostly s-waves. Because only the radial coordinate is accessible to the black hole it does not make use of any additional angular bulk modes. Consequently black holes decay equally in all modes, both in the bulk and the brane. In the simplest ADD model, SM fields are confined to the brane and only gravitonspropagate in the bulk. Hence the number of available modes for emission on the brane exceeds the number of modes available for bulk emission. The majority of the mass loss is therefore expected to take place through the emission of visible Standard Model particles on the brane.

Apart from the spin-down and Schwarzschild phases[2], the dynamics of the black hole decay is poorly understood. The remainder of this thesis will concern itself only with the Schwarzschild phase. The characteristics of this phase is discussed in Section 1.3.3.2.

1.3.3.2 The Schwarzschild decay phase

Black hole mass loss in the Schwarzschild phase occurs through the Hawking evaporation mechanism (18). The process of Hawking radiation may be understood in terms of the creation of virtual particle pairs close to the black hole horizon. The particle with positive energy escapes the gravitational pull of the black hole, while its partner carrying the same magnitude "negative" energy is absorbed by the black hole thereby decreasing the mass of the latter by the same amount carried away by escaping particle. As already mentioned, the resulting black hole radiation spectrum is blackbody-like and described by the characteristic Hawking temperature (1.26).

[1] It has been argued that, depending on the impact parameter and dimensionality of space-time, the mass loss through gravitational radiation during initial balding may be as high as 55% of the total energy (11).

[2] These two phases are often collectively referred to as the Hawking evaporation phase.

The energy spectrum[1] for a higher-dimensional spherically symmetric black hole is given by:

$$\frac{dE^{(s)}(\omega)}{dt} = \sum_j \sigma^{(s)}_{j,n}(\omega) \frac{\omega}{[\exp(\omega/T_H) \pm 1]} \frac{d^{n+3}k}{(2\pi)^{n+3}} \tag{1.28}$$

In the above, s is the spin of the degree of freedom emitted by the black hole while j is its angular momentum quantum number. The denominators contain a spin statistics factor which is -1 for bosons and +1 for fermions. Massless particles ($|k| = \omega$) reduce the phase-space integral to an integral over the particle energy ω. For massive particles ($|k|^2 = \omega^2 - m^2$) however, the rest mass appears in the energy ω in the denominator to the effect that a Hawking temperature $T_H \geq m$ is required for the emission of a particle with rest mass m.

As the decay progresses the black hole mass decreases and its Hawking temperature rises. The radiation spectrum is therefore expected to harden, such that later emission will typically be more energetic. This time-evolution of $T_H(t)$ assumes the validity of the so called quasi-stationary decay model, where the black hole has time to equilibrate at a new temperature between successive emissions. By contrast, the rapid decay approximation (19) assumes that T_H remains fixed througout the decay.

The term $\sigma^{(s)}_{j,n}(\omega)$ in Equation 1.28 distorts the black hole radiation spectrum from that of a perfect blackbody. Suitably, it is called the *greybody factor*. This factor is seen to depend on the energy of the emitted particle (ω), its spin (s), its angular momentum (j) and also dimensionality of spacetime. The greybody modification of the particle emission spectra may be understood in the following qualitative terms:

Unlike radiation emitted from a blackbody in flat spacetime, a particle emitted by a black hole will necessarily have to traverse a very strong gravitational background before reaching the observer at infinity. The number of particles successfuly reaching infinity (and hence also the radiation spectrum) will depend on the energy of the propagating particle and the shape of the gravitational barrier it has to traverse.

[1] The energy emitted per unit time, derived from the number of particles emitted combined with the energy they carry.

Particle	d_s
Quarks	72
Gluons	16
Charged leptons	12
Neutrinos	6
Photons	2
Z^0	2+1
$W^{\pm}$	4+2
Higgs	1
TOTAL	118

Table 1.9: Degrees of freedom (d_s) associated with elementary particles of the SM.

The greybody factors then signify the transmission cross-section for a particle propagating in the gravitational background surrounding the black hole, or in other words represent the probability for particle transmission through curved spacetime outside the black hole horizon. The greybody factor will yield slightly different spectra for different particle species, moreover its dependency on the number of extra dimensions entails information on the spacetime structure surrounding the black hole. Higher-dimensional greybody factors have recently been computed, the procedure for which is described in (11) and (6).

It is important to note that it is the individual *degrees of freedom* rather than elementary particles that enter Equation 1.28, the latter of which may contain more than one polarization. Table 1.9 lists the number of degrees of freedom associated with SM particles[1], where for each of the massive gauge bosons one of the degrees of freedom come from the Higgs mechanism (6). The relative proportions and energies of different elementary particles emitted by the black hole can then be computed by combining the necessary degrees of freedom with their corresponding flux/power spectra (6).

[1] Table 1.9 does not take the possible existence of right-handed neutrinos into account.

1.3.4 Experimental Signatures

The black hole decay process described in 1.3.3 gives rise to characteristic experimental signatures which provide for the identification of black hole events at the LHC. These signatures are extensively discussed in (16). Some of the most distinctive experimental features of black hole events at collider experiments are listed below:

- ***Large Production Cross Sections***
  Black hole production enjoys unusually large cross sections for exotic processes. Because the cross section grows with energy (at a rate determined by the dimensionality of spacetime), this is particularly true at high $\sqrt{s}$.

- ***Ratio of hadronic to leptonic activity of roughly 5:1***
  The Hawking evaporation gives a ratio of hadronic to leptonic activity of approximately 5:1. Black hole events will exhibit only a very small fraction of missing energy in the detector.

- ***Large multiplicity***
  Black hole events are typically characterised by large multiplicities with many hard jets and hard prompt leptons.

- ***High sphericity***
  Since most black holes are believed to be produced with only a moderate boost factor in the laboratory frame, black hole events are expected to exhibit highly spherical topologies[1].

- ***High*** E_T
  The total energy deposited is a considerable fraction of the beam energy. The high sphericity of black hole events implies visible transverse energy of the order $\sim \frac{1}{3}$ of the total deposited energy[2] (12).

[1] Complete sphericity is only achieved in events corresponding to the completely inelastic collision $ij \to BH$ producing a non-spinning black hole at rest in the laboratory frame.

[2] In completely spherical events the transverse energy accounts for $\frac{1}{2}$ of the total energy.

- ***Suppression of hard perturbative scattering processes***
  Black hole production at high energies is a non-perturbative process which suppresses hard perturbative scattering processes by cloaking the latter behind the event horizon formed during collision. (Such a suppression should become visible in *e.g* Drell-Yan or two jet cross sections at transplanckian energies (12).)

Based on the above characteristics of black hole events at high energy colliders, experimental cuts have been proposed to select black hole events with negligible Standard Model background. The experimental cuts employed in this analysis are discussed in Section 4.3.2.

Chapter 2

Experiment

2.1 The Large Hadron Collider

When completed, the Large Hadron Collider (LHC), currently under construction at the CERN laboratory near Geneva, will be the most powerful particle accelerator to date. Two operative modes are forseen, one using protons as colliding particles, the other heavy ions. Only the former is considered in this thesis.
With the intent to advance our understanding of fundamental physics and constrain existing theoretical models, the LHC will collide proton-on-protons with a center of mass energy of 14 TeV. To achieve such high collision energies, the full chain of accelerators at CERN is employed (2.1). The protons are initially extracted from hydrogen gas using a deoplasmatron and subsequently accelerated to energies of 50 MeV in the LINAC2 linear accelerator. The protons are then given an additional boost to 1.4 GeV in the Proton Synchrotron Booster (PSB) before injection into the Proton Synchrotron (PS) complex. The PS "groups" the protons into *bunches* of $n_b \sim 10^{11}$ protons. Separated by ~ 25 ns, each bunch is accelerated to 25 GeV and passed on to the Super Proton Synchrotron (SPS) where the energy is increased further to 450 GeV. Finally, the proton bunches are injected into the LHC ring to form two counter rotating beams of 7 TeV. The beams are made to collide at four different points along the ring around which different detector installations are constructed. The ATLAS and CMS detectors are general-purpose experimens with wide physics programmes, while LHCb and ALICE are dedicated to B-physics studies and heavy ion physics, respectively.

The work in this thesis is performed within the framework of the ATLAS experiment. The ATLAS detector is therefore described in greater detail in Section 2.2.

With a bunch frequency of $f_b \approx 40$ MHz and transverse spread $\sigma_b \approx 16\mu$m, the LHC is designed to operate at a luminosity of

$$\mathcal{L} = \frac{1}{4\pi}\left(\frac{n_b^2}{\sigma_b^2}\right) f_b \approx 10^{34} cm^{-2} s^{-1} \tag{2.1}$$

This is orders of magnitude higher than any previous or current accelerators[1]. (In the first three years of running, during the "low luminosity phase", the LHC will operate at $\approx 10^{33} cm^{-2} s^{-1}$). The LHC design luminosity corresponds to a staggering 10^9 events produced per second, a small fraction of which will correspond to hard scattering interactions between two partons of the incoming protons, as shown in Figure 2.2.

The colliding partons (A,B) each carry a fraction of the proton momentum (x_a,x_b), and hence collide at center of mass energies $\sqrt{\hat{s}} = \sqrt{x_a x_b s} < 14$ TeV. In order to produce a 5 TeV object, the colliding partons must therefore each carry a momentum fraction $x \sim 0.35$ (20). The momentum fraction carried by the constitutent partons at a given momentum transfer Q^2 is dictated by the parton distribution functions. The CTEQ5M parton distributions is shown as a function of x in Figure 2.3[2]. Hard scattering events at the LHC are dominated by the production of QCD jets, and these provide a challenging background to many interesting signals at the LHC, including black hole events.

The large majority of events at the LHC will however not be hard scattering events, but rather so called "soft events" resulting from large distance interactions, where the colliding particles are scattered at small angles and most of the collision energy is lost down the beamline. Such events are called *minimum bias* events and though they are largely unintersting from a theoretical point of view, they still present a formidable challenge to the experimental apparatus. A black hole event produced in a given bunch crossing will on average be overlapped by 25 minimum bias events, an effect known as *pile up*. In order to study black holes

[1] By comparison, the Tevatron ($p\bar{p}$ collider) delivers peak luminosities of $\sim 10^{32}$ cm^{-2}s^{-1}

[2] Note that CTEQ5L, rather than CTEQ5M have been used in the analyses presented in this thesis.

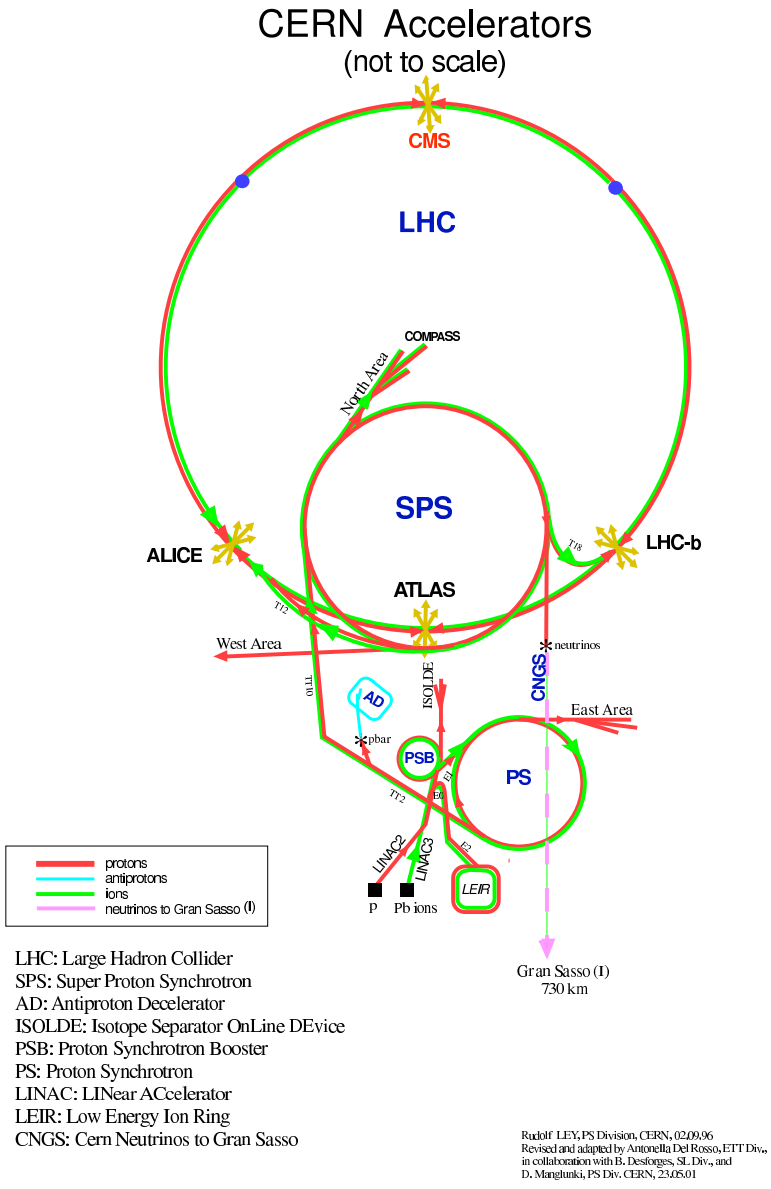

Figure 2.1: The CERN accelerator complex. (From CERN webpages).

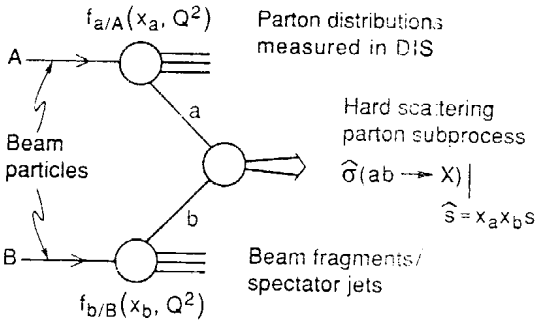

Figure 2.2: Hard scattering process at the LHC (20).

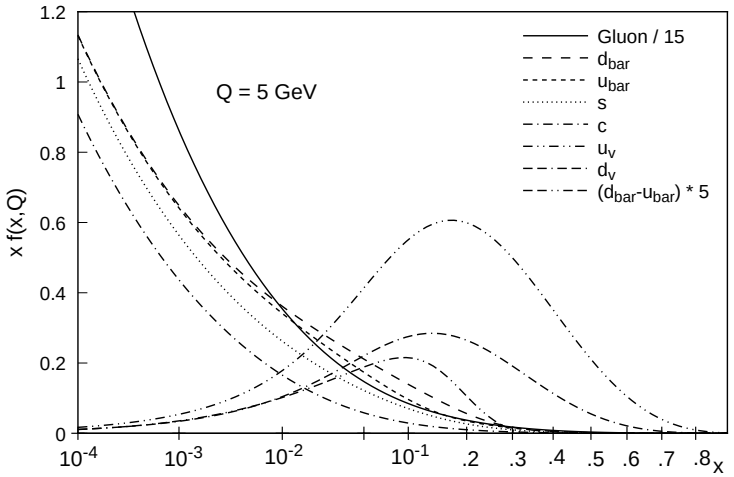

Figure 2.3: CTEQ5M parton distributions evaluated at $Q = 5$ GeV (21)

at the LHC, the black hole events must not only be distinguished from the QCD background, but must also be "extracted" from pile-up. Pile-up effects impact the design of the LHC detectors in a threefold way:

- fast response times are required to avoid integrating over serveral consecutive bunch crossings and thereby increase pile-up
- fine readout granularity is required to allow for the separation of signal and pile-up
- radiation hard material is required to withstand the high flux of particles from both hard scattering and pile-up.

The rest of this chapter will discuss the design of the ATLAS detector in more detail.

2.2 The ATLAS detector

The ATLAS detector is a general purpose detector designed to take full advantage of the physics potential at the LHC. Its ambition is to operate at full LHC luminosity ($10^{34} cm^{-2} s^{-1}$) and provide precision measurements over a range of different physics channels. The ATLAS physics program has a wide scope and includes:

- Various Higgs bosons searches and exploration of electroweak symmetry breaking.
- Searches for physics beyond the Standard Model, such as SUSY and extra dimension scenarios.
- Precision measurements of the t quark and W boson masses, including electroweak gauge boson couplings.
- QCD measurements of α_S and parton distribution functions over a large Q^2 range

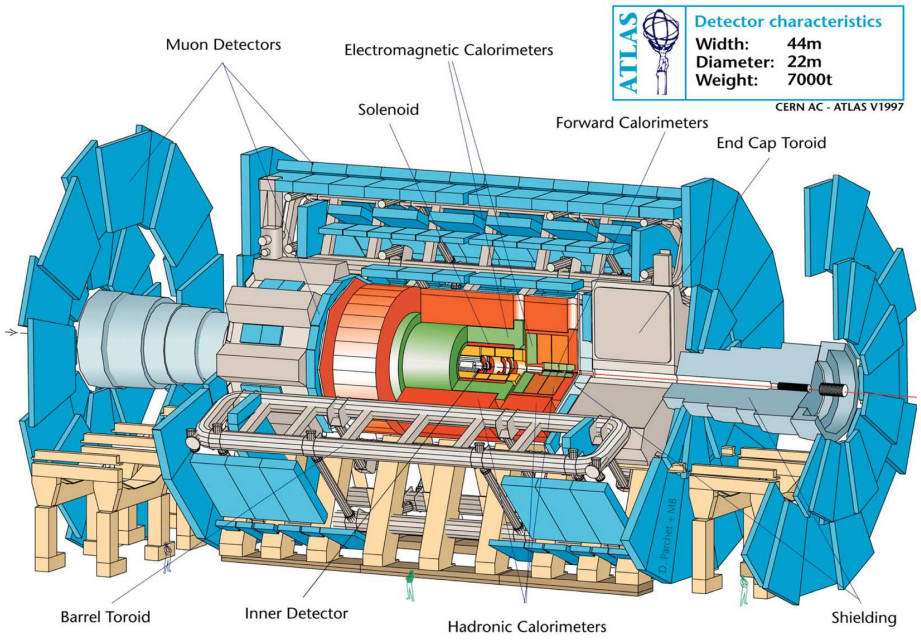

Figure 2.4: Cutaway view of the ATLAS detector revealing its various subdetectors (From (22)).

- B-physics studies including precision measurements of CP-violating B-meson decays.

The study of the above physics is performed by identifying and measuring relevant properties of decay products registered in the ATLAS detector and finally interpreting these measurements within the context of the theoretical model of interest.

Figure 2.4 shows a cutaway view of the ATLAS detector with its three principal subdetectors: a tracking chamber (Inner Detector) closest to the beam pipe surrounded by calorimeters and finally a muon spectrometer in the outermost layer. A brief description of each of these detector subsystems is given below. In addition, ATLAS possesses two superconducting magnet systems; a central solenoid providing a 2 T magnetic field to the Inner Detector and several air-core toroids operating in the muon spectrometer. All in all, the ATLAS detector measures a stunning 44 m in length and 22 m in diameter.

2.2.1 ATLAS Geometry

ATLAS is roughly cylindrically symmetric about the beamline and centered at the interaction point, with the z-axis defined by the beam direction. The x-axis points from the interaction point to the centre of the LHC ring with the y-axis pointing upwards. The cylindrical symmetry renders a R, ϕ, z coordinate system more convenient, where R measures the transverse distance from the beamline and ϕ measures the azimuthal angle around the beam. The polar angle θ is then measured as the angle from the beam axis, allowing for a definition of the pseudorapdity $\eta = -\ln\left(\tan\left(\frac{\theta}{2}\right)\right)$. Particle momenta are commonly described by the η, ϕ, and p_T coordinates, where the latter reflects the particle's momentum in the transverse plane, $p_T = \sqrt{p_x^2 + p_y^2}$.

2.2.2 The Inner Detector

Placed in the inner regions of the ATLAS detector, the Inner Detector (ID) is designed for high-precision track and vertex reconstruction of charged particles, measuring both primary and secondary vertices. In addition, the ID will provide measurements of particle momenta and charge and contribute to particle identification. This tracking effort requires numerous precision measurements of a particle's positions along its track. For these points to allow for accurate reconstruction, all the individual active elements must in turn be able to detect particles with high efficiency. Fine granularity (and low occupancy) detector modules ensures efficient reconstruction of a given hit pattern into tracks.

The typical LHC interaction is expected to yield a very high track density in the regions close to the interaction point. The high multiplicity character of black hole decays makes efficient and accurate track reconstruction all the more important (Figure 2.5). However, the ID introduces material between interaction point and the surrounding calorimetry system. Accurate tracking thus comes at the cost of degraded energy measurements. Consequently the total number of precision layers in the ID is restricted by the conflicting desires for accurate energy measurements and high-precision tracking.

The ID comprises three subsystems:

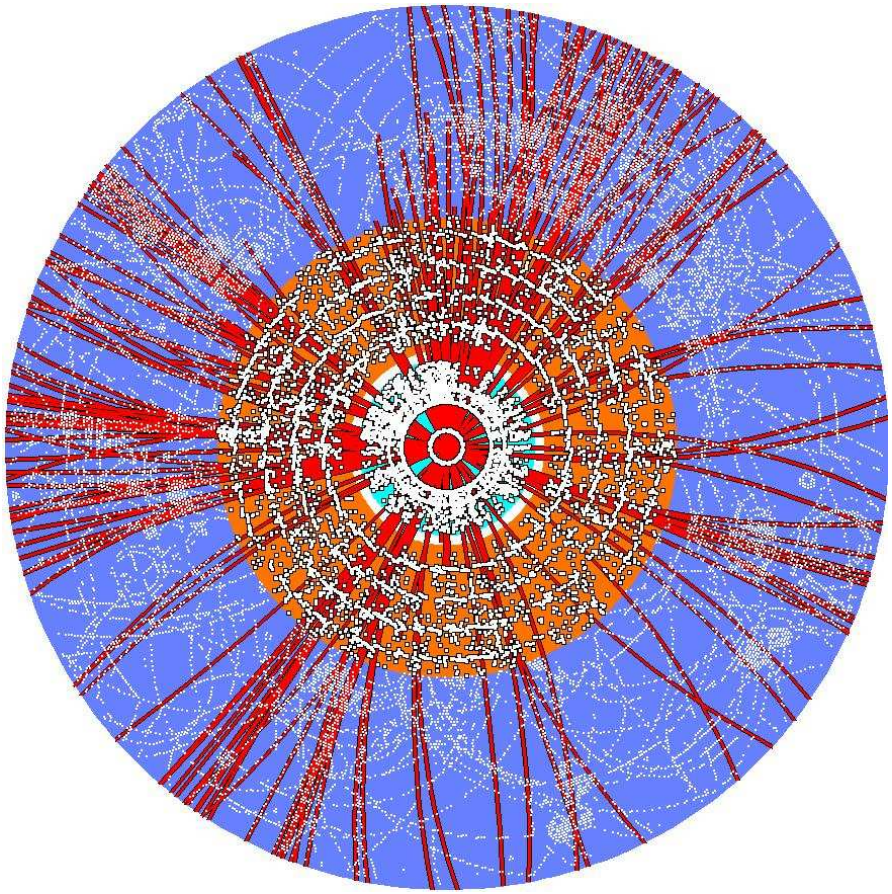

Figure 2.5: Simulation of a BH event showing the high track density in the ATLAS Inner Detector region. The Pixel Detector is marked in turqoise, the SCT in orange and the TRT in purple (X-Y projection).

- The Silicon Pixel Detector
- The Semiconductor Tracker
- The Transition Radiation Tracker

each of which consists of a central "barrel" region with two "endcaps" at larger $|z|$ (Figure 2.6). Furthermore, all three subsystems are specially designed to endure the very high radiation levels suffered in the ID region. The entire system forms a cylindrical volume (7 m $\times$ 1.5 m) contained within a solenoidal magnetic field of 2T directed along the beam axis. Tracks of charged particles passing through the detector will consequently be bent into the transverse plane.

Brief mention of the subdetectors is given below.

2.2.2.1 The Pixel Detector

The Pixel Detector provides high-precision tracking and vertexing in regions close to the interaction point. It determines impact parameters which in turn help to identify particles produced at secondary vertices as daughters of b-quarks and τ-leptons[1].

The close proximity to the interaction point and the high occupancy environment requires radiation hard detectors and read-out electronics. The Pixel Detector barrel comprises three concentric cylindrical layers, the innermost at a radius of 5 cm. Five disks on either side of the barrel form the barrel endcaps, providing angular coverage out to $|\eta|$=2.5. A particle track with $|\eta|$ <2.5 will therefore be precisely measured in three active layers. Both barrel and endcaps are made up of modules of size 62.4 mm $\times$ 21.4 mm. The sensitive part of the module is a silicon wafer instilled with 61 440 50 pixel elements with dimensions μm $\times$ 350 μm. The entire system comprises more than 2000 such modules, providing the high density of active elements required for tracking in a high occupancy environment.

[1] b-tagging/τ-tagging

2.2.2.2 The Semiconductor Tracker

Not unlike the Pixel Detector, the the Semiconductor Tracker (SCT) measures particle positions by detecting electrical charges liberated by charged particles passing through a silicon diode. While its technology is similar to that of the Pixel Detector, its design is modified by its operation at larger radii with lower track densities. At the SCT distance from the beam pipe, a measurement of ϕ yields a higher p_T resolution than would a measurement of η (23). Lower track densities and greater area of coverage favours silicon microstrip detectors with fewer read-out channels and less material than found in the Pixel Detector.

The SCT barrel comprises four central layers and two endcaps, the latter made from wedge-shaped modules. The modules of the SCT barrel are made up from silicon wafers instilled with 768 read-out strips of 6 cm aligned along $|\eta|$ and arrayed in ϕ at a 80 μm pitch. Each module consists of four one-sided p-n detectors (silicon wafers) bonded back-to-back in pairs. The detector (wafer) pairs in a module are placed one above the other, with the upper wafer misaligned by a 40 mrad stereo angle w.r.t. the lower wafer to provide some resolution in η (Figure 2.8). Inside the SCT barrel, the strips of the back plane (lower wafers) are placed parallel to the beam axis. The R-ϕ component is then accurately measured from the hit strip while the second track coordinate is determined from the slight misalignment of the two detector planes.

All in all, the SCT will provide eight precision measurements of each track, thereby contributing to momentum, impact parameter and vertexing measurements.

2.2.2.3 The Transition Radiation Tracker

The Transition Radiation Tracker occupies the bulk of the ID volume. It is a drift tube system designed to provide numerous measurements of charged particle postions and to contribute to their identification.

The TRT is a gas filled straw detector comprising over 370 000 conducting straws, each of which consists of a thin wire anode immersed in a $Xe/O_2/CO_2$[1]

[1]The original proposal(22) involved a $Xe/CH_4/CO_2$ gas mixture. This has since been modified (24).

(70:20:10) gas mixture. Aluminium straw walls act as cathodes. A potential difference of 1.6 kV is maintained between wire and straw to collect charge liberated by charged particles passing through the gas mixture.

The space between the straws is filled with polypropylene/polyethylene fibres, a medium with abruptly varying refractive index. Traversing electrons emit transition radiation (soft x-rays) detectable in the straw tubes. Using a lower charge collection threshold for sufficiently ionising particles and a higher threshold for electrons and associated transition radiation, the TRT is able to perform elementary particle identification tasks such as discriminating electrons from pions.

The TRT comprises roughly 5300 axially oriented straws in the barrel and 320000 radially oriented straws in the endcaps. Hence a particle with $|\eta|$ <2.5 (and p_T >0.5 GeV) will cross an average of 36 straws generating 36 low energy hits per track. The large number of measurements compensates for reduced precision and facilitates improved tracking and momentum resolution.

2.2.3 ATLAS Calorimetry

The ATLAS calorimetry measures electron, photon and jet energies by completely stopping incident particles and measuring the energy loss of the deceleration process. It also contributes to E_T^{miss} measurements and triggering.

Particles incident on the calorimeters lose energy through various processes creating a shower of low energy particles whose energy is measured by the calorimeters. The total energy of a shower is equal to that of the incident particle. Accurate E_T^{miss} measurements therefore rely on a hermetically sealed calorimeter system.

ATLAS will make use of only sampling calorimeters. The deposited energy is measured in active layers interleaved with dense absorber layers. The energy fraction deposited in the active layer is used to determine particle energies, while the absorbers are used to bring particles to a hault.

Black hole events are typically characterized by a large number of energetic particles and low missing energy. Accurate measurements of jet, electron and photon energies are essential for an accurate black hole reconstruction (Figure 2.12).

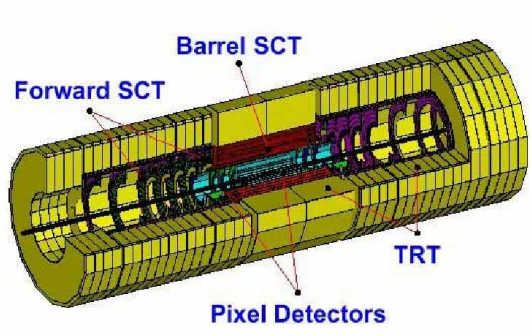

Figure 2.6: The ATLAS Inner Detector (From ATLAS webpages).

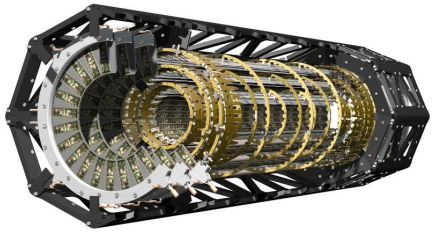

Figure 2.7: Cutaway view of the Pixel Detector revealing its three active layers (From ATLAS webpages).

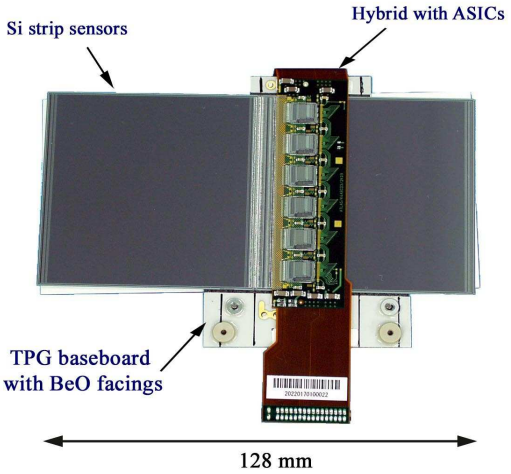

Figure 2.8: An SCT module with a stereo rotation of the upper wafer (From ATLAS SCT webpages).

Figure 2.9: The TRT endcap with radially oriented straws (From ATLAS webpages).

The ATLAS calorimetry consists of two subdetectors,

- The Electromagnetic Calorimeter (ECAL)
- The Hadronic Calorimeter (HCAL)

each of which are given brief mention below.

2.2.3.1 The Electromagnetic Calorimeter

Electrons and photons are stalled sooner than hadrons. The Electromagnetic Calorimeter therefore forms the innermost detector of the ATLAS calorimetry.

The barrel calorimeter contains three sampling layers. Lead and liquid argon (LAr) are used as absorber and active material, respectively. To ensure continuous azimuthal (ϕ) coverage and hermeticity, the absorber and active layers in each sampling are folded into an accordian geometry, a novel technique first utilized at large scale in ATLAS.

The ID, solenoid and cryostat provide $\sim$2 radiation lengths of material in front of the main calorimeter. To correct for energy losses in material upstream of the calorimeter, a presampler ($|\eta| < 1.8$) is placed in front of the ECAL barrel.

The preshower and first sampling enhance particle identification, providing good π^0/γ and e/π separation. Electrons are identified by way of shower shapes and track information from the ID.

The second sampling is transversely segmented into square towers sized $\triangle\eta \times \triangle\phi = 0.025 \times 0.025$ ($\sim$4cm$\times$4cm at η=0). The third sampling has a twice coarser granularity.

The high granularity region may be used to separate pions, electrons and photons, while the coarser regions may assist in E_T^{miss} measurements and jet reconstruction.

2.2.3.2 The Hadronic Calorimeter

The Hadronic Calorimeter is designed to identify jets and measure their energy and direction. In addition, it will perfrom E_T^{miss} measurements and enhance the particle identification capabilities of the ECAL by measuring leakage, etc.

The HCAL may be divided into three subdetectors,

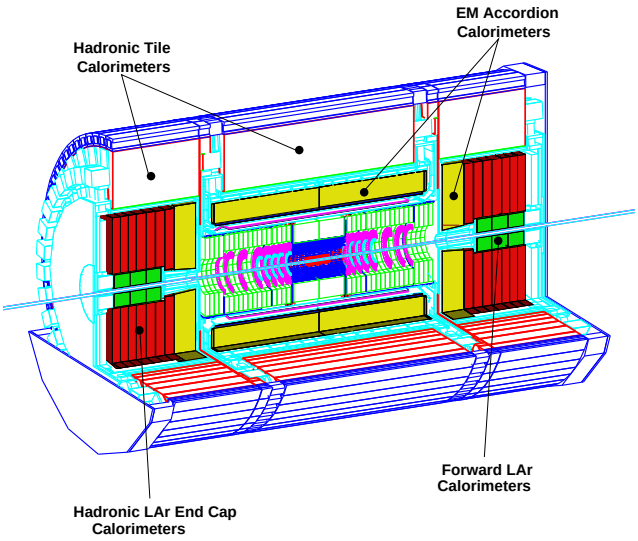

Figure 2.10: The ATLAS calorimetry (Adapted from (25)).

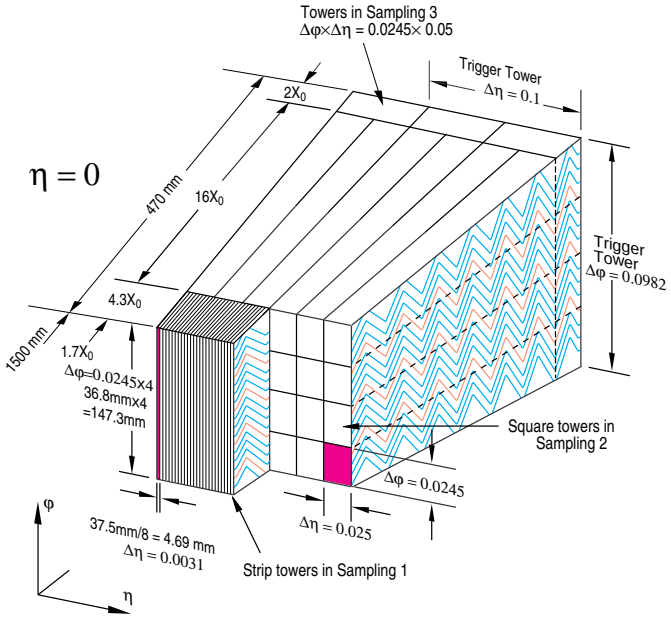

Figure 2.11: An ECAL module with its characteristic accordian geometry (From (25)).

- The Hadronic Tile Calorimeter ($|\eta| < 1.7$)
- The Hadronic Endcaps ($1.5 < |\eta| < 3.2$)
- The Forward Calorimeter ($3.2 < |\eta| < 4.9$)

The *Hadronic Tile Calorimeter* covers the barrel and "extended barrel" regions and consists of steel absorber plates interspersed with plastic scintillator tiles. The scintillating material emits light when traversed by incoming radiation. The scintillator light is collected by photomultiplier tubes and converted to electronic signals. The Tile Calorimeter is divided into two sections, the barrel ($|\eta| < 1$) and the "exteded barrel" ($0.8 < |\eta| < 1.7$) separated by a small gap to allow for feed-out of electronics from the inner regions of ATLAS. The scintillator tiles are subdivided into cells arranged nearly constant in η and placed perpendicularly to the beamline.

The endcaps are required to withstand higher radiation levels than the barrels. The *Hadronic Endcaps* therefore consist of parallel copper absorber plates filled with LAr. The *Forward Calorimeter* face the highest radiation levels and is therefore made up of three dense compartments: one Cu and two tungsten absorber matrices with regularly spaced high-voltage rods subsumed in grounded tubes. The rods are separated from the tube walls by a thin active layer of LAr. It measures high-rapidity ($3.2 < |\eta| < 4.9$) hadronic and electromagnetic activity, thereby contributing to p_T^{miss} and forward jet detection.

The HCAL must be of sufficient thickness to contain hadronic showers and reduce leakage into the muon system to a minimum. At η=0 the thickness totals 11 interaction lenghts (λ) ($\sim$2 m) where $\sim 10\lambda$ suffices for a good high energy jet resolution. This thickness alongside its wide η coverage will also enable the HCAL to provide good E_T^{miss} measurements.

2.2.4 The Muon Spectrometer

The ATLAS calorimeter is surrounded by the Muon Spectrometer, designed to identify muons and perform high-precision muon momenta measurements. Muons are relatively long-lived and heavy with no strong interactions, and therefore lose energy mainly by way of ionization processes. Unlike the large majority of

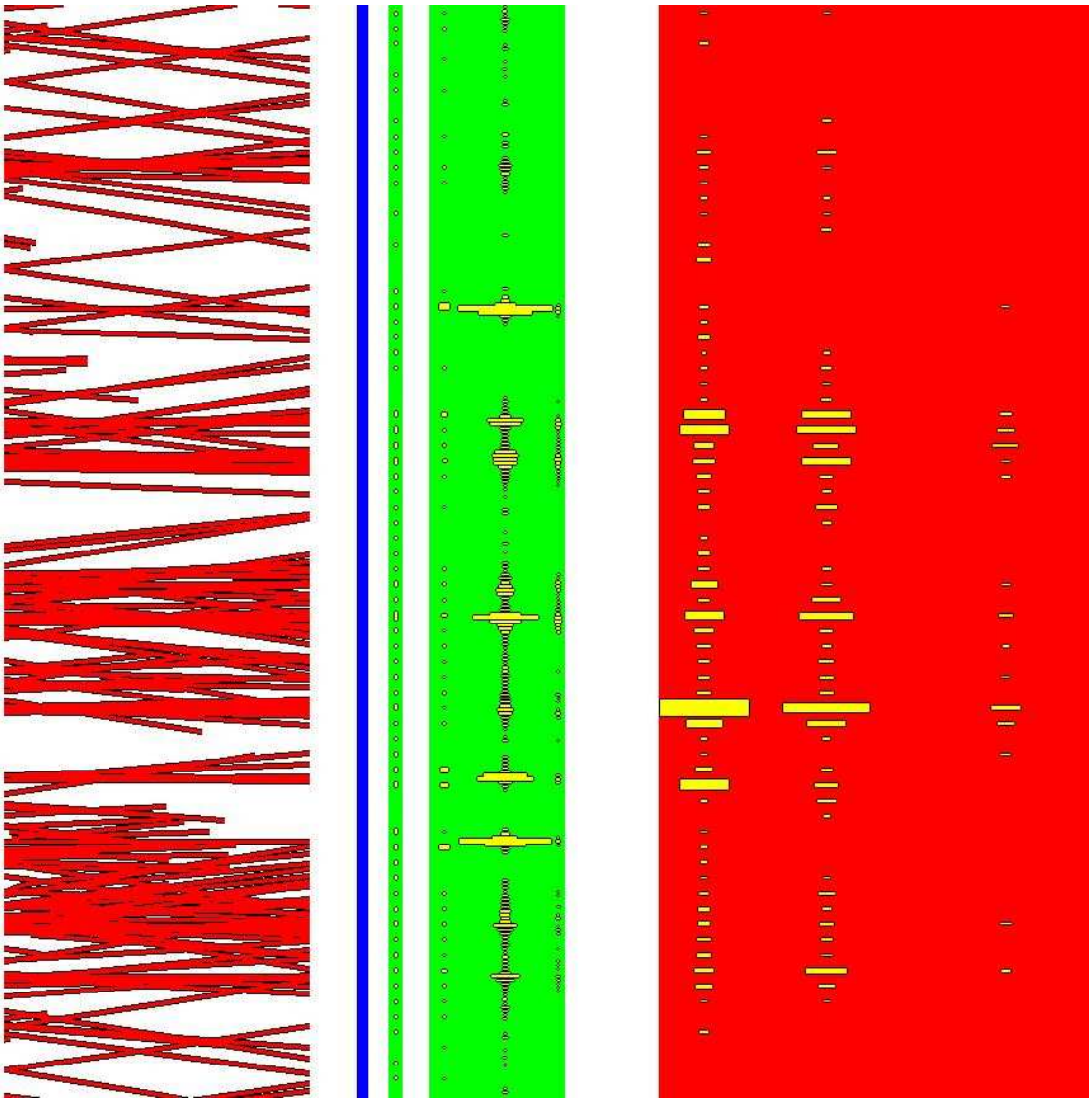

Figure 2.12: R-ϕ projection of a black hole event in the ATLAS calorimeter system. The presampler and ECAL are marked in green, while the hadronic calorimeter is marked in red. A coarser granularity is clearly observed in the latter. The far left column shows simulated tracks in the ID region.

particles, far reaching muons pass through the ATLAS calorimetry making them available for detection in the Muon Spectrometer.

The Muon Spectrometer is the largest of the ATLAS detector subsystems. It is immersed in a toroidal magnetic field sustained by 8 superconducting air core toroids arranged radially about the beam axis to produce a magnetic field directed perpendicularly to the muon trajectory. The resulting bending of the muon tracks improves the accuracy of the ID momentum measurements which are limited by the relatively small size of the ID.

Precise determinations of muon momenta require measurements of track position in the bending plane of the magnetic field. The muon spectrometer's precision measurements therefore consists of *Monitored Drift Tube* chambers (MDT) aligned symmetrically about the beamline in the barrel and vertically in the end-caps.

Closer to the interaction point and around the beamline ($2< |\eta| <2.7$), the MDTs are replaced by high-granularity multiwire proportional chambers with cathode strip read-out designed to cope with higher rates.

Since the drift tube charge collection time exceeds the 25 ns LHC bunch spacing, the Muon Spectrometer requires an independent trigger system. The trigger system consists of *Resistive Plate Chambers* in the barrel and *Thin Gap Chambers* (cathode strip) in the end-caps, arranged so that a muon track will pass through three such trigger chambers with positions optimized to match the acceptance of the precision chambers. The trigger information may therefore supplement the measurements of the precision chambers with an extra coordinate (ϕ) to assist in track fitting and pattern recognition. The trigger system extends out to $|\eta| <2.4$ and triggering is achieved with >6 GeV muons with a time resolution of $\sim$4 ns. There is therefore ample opportunity to connect the event to its corresponding bunch crossing.

2.2.5 The Trigger

The ATLAS detector has a staggering $\sim 10^8$ electronic channels and a bunch crossing frequency of 40 MHz. If all events were read out this would yield 40 terabytes of data per second. This is an amount beyond our storage capabilities,

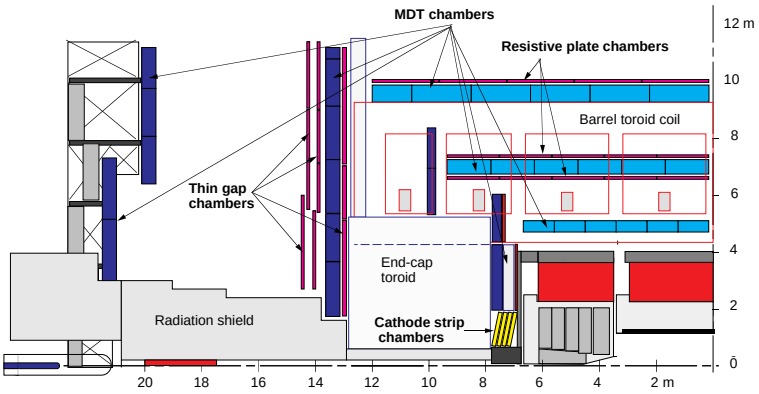

Figure 2.13: Side view of one quadrant of the muon spectrometer (From (26)).

moreover the speed at which an event may be written to storage is only of the order of 10 Hz. Clearly a fast and powerful event selection is required, which also retains excellent efficiency for rare new physics, including black hole events.

The ATLAS Trigger is designed to remove minimum bias events to enable data storage without loss of interesting physics. It reduces the event rate by a factor of 10^7, thereby reducing the data rate from 40 TB/s to 100 MB/s. The trigger system comprises three trigger levels of online event selection. Each subsequent level faces a lower event rate and can thus afford a higher level of sophistication than the previous level.

The *first level trigger* (LVL1) reduces the event rate from 40 MHz to less than 100 kHz using reduced granularity data from the calorimeter and muon spectrometer. LVL1 looks for high p_T leptons and photons, jets, $\tau \rightarrow$ hadrons, large E_T^{miss} and ΣE_T and passes the selected events on to the next trigger level.

The *second level trigger* (LVL2) has the full precision and granularity data availabe, including tracking data from the ID. However, it focuses on so called *regions-of-interest* (RoI) preselected by LVL1, thereby reducing the data rate to $\sim$1 kHz.

The *third level trigger* (*Event Filter*) terminates the online selection process and reconstructs the complete event, making use of all the total data set from all the subdetectors. Sophisticated algorithms based on physics criteria decide whether the event is to be kept or discarded. Selected events are passed on for permanent storage, along with the latest alignment and calibration data.

Chapter 3

Simulation Software

Simulation studies form a critical part of any experiment in high energy physics. They serve to guide the design and construction of detectors and provide the reference required for a proper analysis of recorded data, both before, during and after the running of an experiment. To best serve their purpose, the simulation tools employed in an experiment like ATLAS are continually improved and calibrated with experimental data.

The simulation of physical processes in ATLAS may be conveniently thought of as a three stage process involving the *event generation, detector simulation* and *reconstruction*.

The event generation is typically handled by general-purpose Monte Carlo programs and involves the "construction" of events as seen by a perfect and flawless detector, from the initial interactions of the colliding particles to the subsequent decay of new particles produced, including radiation emitted by both initial and final state particles.

The response of the detector to the event is simulated using a GEANT (27) based framework which provides an extensive description of the detector design and geometry as well as the many different interactions of particles with matter at the relevant energies. The stable particles of the generated event pass through this detector and interact with its various parts leaving behind a trail of hits in the tracking devices and energy deposits in the calorimetry. From the hits and deposits, the event is *digitized* and stored in the same format provided by the electronic read-out of a real event.

Finally the original event is *reconstructed* from the digitized data. This process is initially performed separately in each subdetector where hits are translated into charged tracks, particle momenta are determined, energy deposits are combined to form jets and so on. Finally the event is reconstructed in its entirety by combining information from all the subdetectors.
While such detailed "full simulations" of particle passage through a detector agree well with experiment, they are typically CPU intensive and very time-consuming[1]. For many studies it is legitimate to trade the full simulation with the less accurate, but far more rapid, "fast simulation" whereby the detailed detector simulation is exchanged for a simplified parametrization of the overall detector performance. Indeed the relatively high statistics required in the this study, render fast simulations more appropriate.
This section provides brief descriptions of the simulation tools employed in this thesis: the PYTHIA (28) event generator, the CHARYBDIS (29) black hole event generator and the ATLFAST (30) fast simulation program.

3.1 Event Generation: PYTHIA

PYTHIA is a general-purpose Monte Carlo event generator which includes an extensive library of subprocesses, parton showering, underlying event simulation and hadronization. This machinery is employed when simulating the evolution of an event. The structure of a typical generated LHC event is shown schematically in Figure 3.1 with time ordering from bottom to top.

Initially two protons are brought to collide. One parton is resolved from each of the protons at a scale Q and momentum fraction x dictated by the parton distribution functions (PDFs) $f(Q, x)$. The two partons produce a heavy, short lived state which subsequently decays to lighter particles. This part of the event is called the *hard subprocess* and corresponds to the lowest order hard interaction.

Since the incoming partons of the hard subprocess are coloured and charged, higher order QCD (/QED) effects such as gluon (/photon) radiation introduce significant contributions to the event topology. These effects are implemented in

[1] Processing speeds are today increased with the advent of grid technologies.

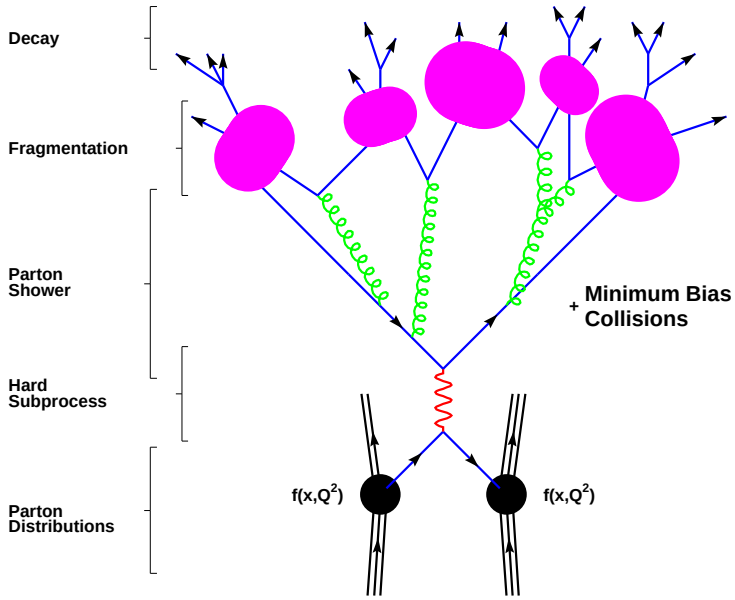

Figure 3.1: The evolution of a generated event. See text for details. Adapted from (31) and modified.

PYTHIA through the *parton shower* method, whereby the initial and final state partons of the hard subprocess initiate a sequence of branchings $a \to bc$ (*e.g* $q \to qg$ and $q \to q\gamma$) which evolves into a shower of partons. Showering initiated by the incoming partons is labeled *initial state radiation* (ISR), while showering from final state partons is called *final state radiation* (FSR). The incoming partons also carry a small *primordial transverse momentum* ($k_\perp$) acquired from the motion of the partons in the original proton.

After parton showering, the event contains

- hard final state partons
- soft gluon and some quarks and photons from ISR and FSR
- remnants of the colliding protons which do not take part in the hard interaction and largely move in opposite directions along the beam pipe.

Colour confinement requires all free quarks, antiquarks and gluons be grouped into colourless, composite hadrons. In the confinement regime, perturbative

QCD breaks down and various phenomenological models[1] are employed to group coloured partons into hadrons. This process is known as *fragmentation*[2] The proton remnants are colour-connected to the hard subprocess and must therefore be included in the fragmentation system of the rest of the event.

In PYTHIA, fragmentation takes place through a successful framework known as the "Lund string fragmentation model". This model assumes a linear confinement potential where coloured partons are colour connected by colourless objects called strings. The string may be thought of as colour flux tube with a behaviour similar to that of a spring. The simplest system corresponds to a $q\bar{q}$ pair moving apart, thereby increasing the potential energy of the string until it finally breaks by the production of a new $q'\bar{q}'$ pair resulting in two systems $q\bar{q}'$ and $q'\bar{q}$. The string-breaking terminates once all string pieces have masses sufficiently small to prevent further breakup and convert into hadrons.

The final step of the event generation involves the decay of unstable hadrons produced in the fragmentation process to lighter particles. In this process the average particle mass is decreased, but the multiplicity of particles significantly increased, leaving only particles that ultimately traverse the detector, such as protons, neutrons, pions, kaons, photons, electrons, muons, neutrinos and their antiparticles.

3.2 Black Hole Simulation: CHARYBDIS

Black hole production and decay is not included in the library of subprocesses provided by general purpose event generators such as PYTHIA or HERWIG(32). A few simple event generators have been developed for the purpose of simulating the production and decay of miniature black holes at hadron colliders. TRUENOIR(33) is one such a Monte Carlo package written as a plug-in module to PYTHIA[3]. It

[1] These models commonly make use of several non-physical parameters tuned to experimental data.

[2] This process is also often referred to as *hadronization*. In this thesis, hadronization understood as the combination of fragmentation and subsequent decay of unstable particles.

[3] I am indebted to K.Baker for providing me with the TRUENOIR code.

simulates black hole in the "rapid decay approximation" where the Hawking temperature remains fixed throughout the decay. The decay is assumed "democratic", but required to conserve baryon and lepton numbers as well as colour.

CHARYBDIS(29) is an improved black hole event generator which includes higher-dimensional greybody effects, time-evolution of the Hawking temperature, black hole recoil against emitted particles and lepton number violation. It simulates black hole production and decay, and interfaces to PYTHIA (or HERWIG) via the Les Houches accord (34) for parton showering, hadronization and decay. The various features of the generator are described in greater detail below.

3.2.1 Model and assumptions

CHARYBDIS (29) is a black hole event generator which uses a simplified model of black hole production and decay which may perhaps allow for an adequate simulation of black hole events, despite the many uncertainties that plague the theory. CHARYBDIS models black hole production as a semi-classical process ($M_{BH} \gg M_P$) in a higher dimensional spacetime with large extra dimensions (where $R \gg r_S$). Black holes are formed when two partons pass within the horizon radius of a Schwarzschild black hole set by their center of mass energy $\sqrt{\hat{s}}$:

$$r_S(\sqrt{\hat{s}}) = \frac{1}{\sqrt{\pi} M_P} \left(\frac{M_{BH}}{M_P} \right)^{\frac{1}{n+1}} \left(\frac{8\Gamma\left(\frac{n+3}{2}\right)}{n+2} \right)^{\frac{1}{n+1}} \tag{3.1}$$

CHARYBDIS employs the semi-classical parton-level cross section

$$\hat{\sigma}(\sqrt{\hat{s}} = M_{BH}) = \pi r_S^2 \tag{3.2}$$

thereby neglecting the balding phase where a fraction of $\sqrt{\hat{s}}$ is expected lost through the emission of gravitational radiation.

CHARYBDIS attempts to model only the Schwarzschild phase and treats only non-spinning black holes. The energy spectrum of the black hole decay products is either greybody corrected or plain blackbody [1]. The energy spectrum of the

[1] CHARYBDIS provides recently calculated greybody factors and greybody modified emission probabilities.

decay particles has a characteristic Hawking temperature T_H:

$$T_H = \frac{n+1}{4\pi r_S} \tag{3.3}$$

which is allowed to vary as the decay progresses to the effect that later emissions will be more energetic. If the time variation of T_H is switched on, T_H is recalculated after every emission. If it is switched off the initial Hawking temperature is maintained throughout the decay (35). The time evolution of T_H presumes the validity of a quasi-stationary approach to the black hole decay, whereby after each particle emission, the black hole has time to equilibrate at a new temperature before emitting a new particle [1].

CHARYBDIS also implements the recoil of the black hole against emitted particles. The black hole recoil leaves subsequent emissions in a boosted frame, more so in the later stages of the decay as the black hole gets lighter.

The black hole decays to all SM particles including the Higgs boson[2] [3]. Any mass loss through emission of gravitons or other non-SM particles is neglected. If greybody effects are switched off, particles are sampled from a blackbody spectrum and the probability of emitting a given particle species is dictated by the associated degrees of freedom (see Table 1.9). If greybody effects are switched on, particles are emitted according to greybody modified emission spectra and probabilities. Thus far the decay may be regarded "democratic", however constraints arise from various conservation laws.

To conserve overall charge, the charged particles emitted are selected in such a way that the magnitude of the black hole charge decreases. CHARYBDIS also conserves baryon number, even though black hole decays may involve baryon number violation. Colour charge is also conserved. Lepton number however, is violated.

Although CHARYBDIS does not model the final Planck phase, it provides various options for terminating the black hole decay process. The termination of the decay is controlled by the switch KINCUT. If KINCUT is switched on, the decay is

[1] (6) indicates that the quasi-stationary approach may be invalid for $n \geq 3$.

[2] Throughout this analysis, the mass of the Higgs boson is set to 130 GeV.

[3] The production spectra of heavy particles may be unreliable if the particle rest mass exceeds the initial Hawking temperature (29).

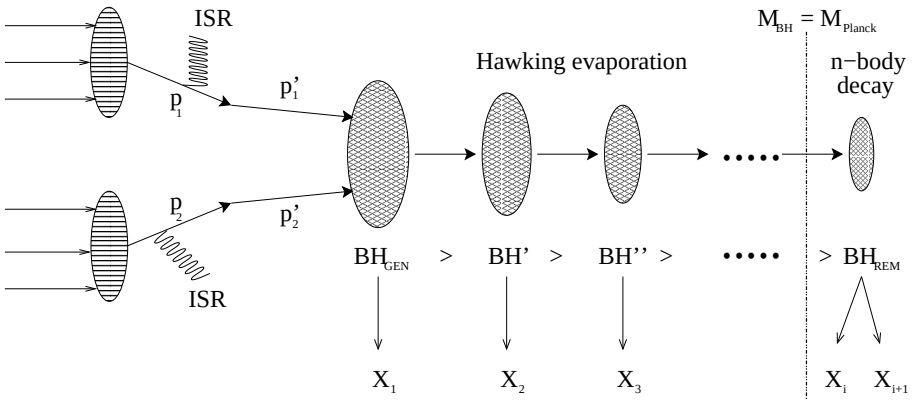

Figure 3.2: The CHARYBDIS-PYTHIA black hole decay model. Two partons (p_1 and p_2) are resolved from the colliding protons. After ISR emissions, the two partons ($p_1^{'}$ and $p_2^{'}$) collide to form a black hole BH_{GEN}. The generated black hole emits a SM particle through the process $BH_{GEN} \rightarrow BH^{'} + X_1$, thereby decreasing its mass to $M_{BH'} < M_{BH_{GEN}}$. This process continues until the mass of the black hole drops below the Planck mass $M_{BH} < M_P$. At this point a 2-body decay is performed on the black hole *remnant* BH_{REM}. The decay products $X_1, X_2, ..., X_i, X_{i+1}$ are finally passed on to PYTHIA for showering and hadronization.

terminated when the energy chosen for the emitted particle is excluded by the kinematics of a two-body decay. If it is switched off, particles are emitted according to the specified energy spectrum until the black hole mass M_{BH} drops below the Planck mass. The latter option is used in all analyses presented in this thesis.

Upon termination, an isotropic NBODY decay is performed on the remnant, where particles are chosen according to the same probabilities used in the first part of the decay. The parameter NBODY may be set between 2 and 5. If the particles selected for the NBODY decay conserve overall charge and baryon number the decay is accepted; otherwise a new set of particles are selected. If charge and baryon number is not conserved after NHTRY selections the whole decay is rejected and a new decay generated. If the whole decay fails after MHTRY attempts, the whole black hole state is discarded and a new state is generated.

A two-body decay (NBODY=2) of the black hole remnant is used throughout this analysis.

The CHARYBDIS decay model employed in this thesis is schematically illustrated in Figure 3.2.

3.2.2 Switches and controls

CHARYBDIS provides the user with several parameters and switches to control the modeling of the black hole production and decay. These features are detailed in (29). For ease of reference, a few of the parameters and switches frequently referred to in this analysis are summarized in Table 3.1[1]. (Note that the parameters MPLNCK and MINMSS allow the user to stipulate the region of validity for the semi-classical cross section given by Equation (3.2)).

Switch	Description	Value
MINMSS	Minimum black hole mass M_{BH}^{min}	x
MAXMSS	Maximum black hole mass M_{BH}^{max}	14000 GeV
MPLNCK	Fundamental Planck mass M_P	x
TOTDIM	Total number of dimensions	x
TIMVAR	Time evolution of T_H	x
GRYBDY	Greybody effects	x
KINCUT	Kinematic cut-off on decay	.FALSE.
NBODY	Number of to which remnant decays	2

Table 3.1: Switches that govern the production and decay of the generated black holes. Values given are fixed throughout the analysis. If the parameters are varied, an x is given instead.

3.2.3 Running CHARYBDIS with PYTHIA

CHARYBDIS relies on PYTHIA for showering, hadronization and decays and interfaces to the latter through the Les Houches accord. A Les Houches compliant version of PYTHIA is therefore required for simulating black holes with CHARYBDIS.

An error in PYTHIA 6.225 (Les Houches compliant) disturbed the interface to CHARYBDIS disrupting simulations of high multiplicity event topologies. After some investigation, the error was found to originate in the PYTHIA subroutine

[1]For all remaining CHARYBDIS parameters not mentioned above, default settings as described in (29) are used throughout this thesis.

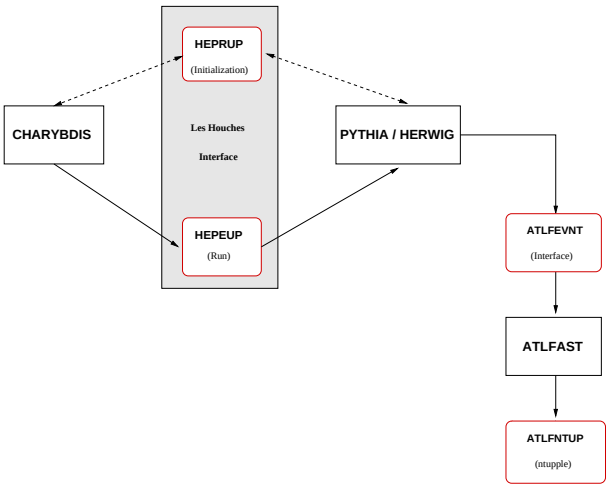

Figure 3.3: The CHARYBDIS interface to PYTHIA.

PYSHOW and the bug-fix has later been implemented in PYTHIA versions 6.226 and above[1]. This section summarizes the work done to ensure a stable interface.

Communication between CHARYBDIS and PYTHIA occurs in two steps. First upon initialization to establish the basic parameters of the run, then for each new event transferred from CHARYBDIS to PYTHIA. These two steps correspond to two distinct Fortran common blocks:

HEPRUP: 'User Process' Run Common Block

HEPEUP: 'User Process' Event Common Block

both of which are described in detail in (34). The common blocks have associated dummy routines UPINIT and UPEVNT which are called from PYTHIA. These subroutines then fill their corresponding common block with information drawn from the output of CHARYBDIS. After the black hole decay, the hard subprocess information is written into the HEPEUP common block and passed on to PYTHIA for showering and hadronization.

When the lower mass (MINMSS) of the generated black holes was set to a value different from the Planck mass (MPLNCK), *e.g.*:

[1]I am indebted to T.Sjöstrand for help and assistance on running CHARYBDIS with PYTHIA.

```
MPLNCK = 1000.0D0
MINMSS = 5000.0D0
```

PYTHIA eventually aborted the simulation with the error message[1]:

```
Error type 2 has occured after       48 PYEXEC calls:
(PYPREP:) colour rearrangement failed
Execution will be stopped after listing of last event!
```

The problem was not observed when MPLNCK and MINMSS were set to the same value. Another interesting point of observation was that the abortion did not occur when generating events with a large number of extra dimensions. Both the reduction in black hole mass (with respect to the Planck mass) and an increase in the number of extra dimensions, result in a reduction in average particle multiplicity. [2] This observation led to the suspicion that PYTHIA fails to handle the large number of primary partons produced in black hole events. However, while Les Houches compliant Pythia 6.200 restricted the number of outgoing particles to 7, PYTHIA versions 6.220 and above should ideally fully support the Les Houches accord and allow the user-defined system to contain upto 80 new particles. Most CHARYBDIS events do not exceed 25 particles.

To check for the number of particles produced in the event PYTHIA fails to handle, a call to PYLIST(7) was introduced in the CHARYBDIS subroutine CHEVNT in order to obtain a listing of the black hole decay products as they are fed into the HEPEUP event record. These listings are reproduced in Appendix B

Two points of comment are in order:

1. The decay products in lines 33 and 34 of the final event listing (before aborting simulation) point to the top quark in line 20. The correct decay products of the top enter lines 25 and 26.

2. The entries of the HEPEUP common block enter the final PYTHIA listing after line number 4. While the mass values are identical, the four-momenta

[1] The precise event that PYTHIA failed to handle would necessarily depend upon the initial random generator seed used.

[2] I am indebted to P.Richardson for his comments and discussion.

ISR (MSTP(61))	on	off	off	on	on	off	off	on
FSR (MSTP(71))	on	off	on	off	on	off	on	off
$k_\perp$ (MSTP(91))	on	off	on	on	off	on	off	off
Simulation	**Abort**	Run	Hang	Run	Hang	Run	**Abort**	Run
4-momenta match	No	Yes	N/A	No	N/A	No	Yes	No

Table 3.2: Effects of switching off ISR, FSR and primordial $k_\perp$

sometimes differ by > 100 GeV (*e.g.* the τ^+ in line 11). (A similar offset in values was observed when comparing a PYLIST(7) and PYLIST(1) for an event that runs).

The erratic behaviour in mother-pointers was found to owe itself to inconsistent documentation. It is ascribed to a PYTHIA bookkeeping error that does not relate to the error messages issued. The solution is implemented in PYTHIA 6.224.

The offset in the four-momenta are attributable to the effects of ISR, FSR, and primordial $k_\perp$. Explicitly switching off these effects (MSTP(61)=0, MSTP(71)=0 and MSTP(91)=0) cause the final PYTHIA four-momenta listings to agree precisely with the input values. Moreover, it avoids the crash and no error messages are produced. The listings are reproduced in Appendix B.

The individual and combined effects of ISR, FSR and primordial $k_\perp$ are summarized in Table 3.2. Table 3.2 indicates that the final PYTHIA four-momenta match the input values from HEPEUP only when ISR and $k_\perp$ are both switched off. This is expected since in PYTHIA the evolution of these is performed in "reverse time-order"[1]. Moreover, PYTHIA aborts the simulation only when FSR is *not* explicitly switched off. A further curious point of observation is that the program comes to a halt without producing error messages ("hangs") when either ISR or $k_\perp$ are switched off and all other settings are left unchanged.

3.2.3.1 Compiler optimization level

It was suggested that the problem of running CHARYBDIS with PYTHIA might relate to the optimization level of the compiler or some other compiler-related problem

[1] The incoming partons are selected from PDFs which include ISR and primordial $k_\perp$ effects. ISR and $k_\perp$ effects are then implemented through a backwards evolution algorithm.

such as *e.g.* the alignment of double precision variables. Options were originally not set to force optimization. An attempt was still made to relax optimization further by lowering the optimization level of the f77 compiler from the default value `-O3` to `-O1` and `-O0`. No changes were observed.

3.2.3.2 Entry by Entry

To establish whether the source of the problem originated in `CHARYBDIS`, the interface to `PYTHIA` or within `PYTHIA` itself, the contents of the `HEPEUP` common block of the event causing the abortion was fed into `PYTHIA` entry-by-entry for subsequent showering and hadronization. While the `PYTHIA` four-momenta did not agree with the `HEPEUP` values to the last decimal, the same event still ran 10^4 times without aborting the simulation or producing any error messages. Clearly, the event as generated by `CHARYBDIS` and read into `HEPEUP` was not at fault.

The origins of the problem were most likely to be found in the interface between `CHARYBDIS` and `PYTHIA`.

3.2.3.3 Pythia Bug-fix

The error was eventually found to be "Les Houches-related" and to originate in the `PYTHIA` subroutine `PYSHOW`. The subroutine allows the user-defined `HEPEVNT` system to shower. It contains switches that control the emission of gluons and photons from the user-defined particles. Normally these switches should first be reset to 0 and then set to 1 for those particles whose emission `PYTHIA` knows how to handle.

In compliance with the Les Houches accord the user-defined system was expanded to contain a total of 80 particles. In expanding from a maximum of 7 to 80 user-defined particles in one and the same showering system, the initial resetting was not expanded accordingly. Consequently, `HEPEVNT` entry number 11 onward were never reset properly[1]. If entry 11 of a given event contained a quark and the same entry of a subsequent or later event contained a *e.g* a Z^0,

[1] The first four entries include the two incoming protons and the two resolved partons before ISR emission.

the latter would now be free to emit a gluon and hence disrupt the colour flow, thereby causing PYTHIA to abort the simulation.

The problem is easily solved by resetting the relevant switches(ISCOL(IR), ISCHG(IR) and KSH(IR)) to zero in the subroutine PYSHOW as indicated in Figure 3.4. The bug-fix is implemented in PYTHIA subversion 6.226 and above.

3.3 Detector Simulation: ATLFAST

ATLFAST is a fast simulation program for the ATLAS detector. It aims to capture the overall detector response and resolution without tracing in detail the passage of each particle through the various layers of the detector. In particular, ATLFAST strives to accord with the full simulation results with respect to:

- mass resolution for all important physics channels
- jet reconstruction efficiencies (in particular b-jets)
- E_T^{miss} resolution

and most parameters are tuned to the results of full simulations.

In ATLFAST the detector is "replaced" by a grid in (η, ϕ) space representing calorimetric cells. The resolution of each cell resembles the average resolution of the detector:

$$\Delta\eta \times \Delta\phi = \begin{cases} 0.1 \times 0.1 & |\eta| < 3 \text{ (barrel)} \\ 0.2 \times 0.2 & 3 < |\eta| < 5 \text{ (forward)} \end{cases}$$

Using the event record supplied by the event generator, ATLFAST deposits the p_T of all stable particles (save muons and neutrinos) within the detector acceptance, in the appropriate calorimetric cell in the (η, ϕ) grid.

After all appropriate cells are filled, ATLFAST groups the cells into *clusters* using a simple cone algorithm. Cells with $p_T > 1.5$ GeV are located in decreasing order and marked as potential initiators of cell clustering. If the total p_T deposited in a cone with half angle $\Delta R \equiv \sqrt{(\Delta\eta)^2 + (\Delta\phi)^2} = 0.4$ of the initiator with the

```
C...Check on phase space available for emission.
      IREJ=0
      DO 140 J=1,5
        PS(J)=0D0
  140 CONTINUE
      PM=0D0
      KFLA(2)=0
      DO 160 I=1,NPA
        KFLA(I)=IABS(K(IPA(I),2))
        PMA(I)=P(IPA(I),5)
C...Special cutoff masses for initial partons (may be a heavy quark,
C...squark, ..., and need not be on the mass shell).
        IR=30+I
        IF(NPA.LE.1) IREF(I)=IR
        IF(NPA.GE.2) IREF(I+1)=IR

c***NEW:RESET SWITCHES HERE
         ISCOL(IR)=0
         ISCHG(IR)=0
         KSH(IR)=0
c***END NEW

        IF(KFLA(I).LE.8) THEN
          ISCOL(IR)=1
          IF(MSTJ(41).GE.2) ISCHG(IR)=1
```

Figure 3.4: Corrections to the PYTHIA subroutine PYSHOW required for its proper interface to CHARYBDIS. See text for details.

highest p_T is greater than 10 GeV, the a cluster is formed comprising all cells within the cone[1].

The next step is particle identification, where the event record is scanned first for muons, then electrons and finally photons. The four-momenta of these particles are smeared according to an energy-, luminosity- and particle-dependent parametrization, (which also accounts for noise and pile-up effects at design luminosity). Particles satisfying the acceptance criteria

$$|\eta| < 2.5 \quad \text{and} \quad p_T > \begin{cases} 6 \text{ GeV} & \text{for } \mu \\ 5 \text{ GeV} & \text{for } e, \gamma \end{cases}$$

after smearing are kept, while those who fail are discarded.

To complete the reconstruction, two separate isolation criteria are imposed:

- The smeared position of the particle must be separated from all other clusters by a distance $\Delta R > 0.4$.
- The total p_T deposited in cells within a cone $\Delta R < 0.2$ surrounding the particle must not exceed 10 GeV (not counting the smeared p_T) of the particle itself).

Particles satisfying these isolation criteria are then deemed as "reconstructed" and their four-momentas are recorded. Clusters belonging to electrons and photons are removed from the list of clusters so as to not take part in the reconstruction of the rest of the event. A particle failing to meet the requirements of isolation is labeled non-isolated if it is a muon, and discarded if it is an electron or a photon.

The next step is jet reconstruction. After the removal of electron and photon clusters, the remaining unidentified clusters with $p_T > 10$ GeV are labeled as jets and smeared with a typical hadronic resolution according to an energy and luminosity dependent parametrization (which again accounts for noise and pile-up at design luminosity). The momenta of non-isolated muons situated within a jet cone are added to the jet momenta. After all appropriate non-isolated muons

[1] While a cluster is always centered on the initiator cell, the position of the cluster is taken as the weighted barycentre of the cluster cell deposits.

have been added to a jet, the jets are reexamined and considered "reconstructed" if found to satisfy $|\eta| \leq 5.0$ and $p_T > 15$ GeV.

Lastly, p_T^{miss} is determined by summing vectorially over all the visible momenta in the event. This includes the p_T of all jets, isolated leptons and photons, non-isolated muons not associated with jets and any cells which were never incorporated into clusters. (The latter are first smeared according to the same resolution applied to jets and included in the sum only if found to contain smeared p_T above a certain threshold). The negative of this sum is then the p_T^{miss} returned by ATLFAST.

Lepton and photon reconstruction efficiencies in ATLFAST are not optimised for agreement with the full simulation results. Apart from those described above, other effects likely to modify the lepton and photon efficiencies such as misidentifying a jet for e/γ are lacking and should ideally be added by hand (36). The lepton efficiency is usually estimated to 90%.

For lack of knowledge, appropriate corrections to lepton and photon efficiencies in ATLFAST have unfortunately been omitted in this thesis.

The ATLFAST low luminosity option has been employed throughout this thesis. A cone based jet algorithm was chosen, with cone size ΔR =0.5. Otherwise, only ATLFAST default settings have been used.

Chapter 4

Simulation Studies

This chapter concerns itself with the simulation studies performed with CHARYBDIS and PYTHIA. The first part presents a parton level study to shed light on the CHARYBDIS black hole model and the properties of the generated black holes. The second part aims to visualise black hole events at the level of the ATLAS detector and studies the characteristic features of black hole events. The third part presents an evaluation of the potential to discover black holes with the ATLAS detector and briefly discusses some of the uncertainties and limitations of the analysis.

4.1 Parton Level Studies

Parton level simulations provide a quick means of determining event topologies by way of primary partons and leptons. The partons and heavy leptons undergo no hadronisation; parton level studies are therefore unable to draw accurate pictures of detector response. They are, however, very well suited for examining the performance of the event generator.

This section provides a study of the performance and output of the CHARYBDIS black hole event generator. Unless otherwise stated, CHARYBDIS default settings are used throughout this analysis.

Particle species	Blackbody (%)	Greybody (%)			
		$n = 2$	$n = 3$	$n = 5$	$n = 7$
Quarks	56.5	61.8	59.6	57.0	55.5
Gluons	16.8	12.2	14.1	16.3	17.5
Charged leptons	9.4	10.3	9.9	9.5	9.3
Neutrinos	4.7	5.2	5.0	4.8	4.6
Photons	2.1	1.5	1.8	2.0	2.2
Z^0 bosons	3.1	2.6	2.8	3.1	3.3
$W^{\pm}$ bosons	6.3	5.3	5.8	6.2	6.6
Higgs	1.1	1.1	1.1	1.1	1.1

Table 4.1: Theoretical blackbody and greybody emissivities. Values are given to one decimal place.

4.1.1 Particle Emissivities

`CHARYBDIS` emits different types of SM particles according to preset theoretical probabilities. This section compares the generator output to the preset theoretical values. As discussed in Section 1.3.3.2, the relative numbers of different SM particles emitted from a black hole can be computed from the number of degrees of freedom associated with each particle. These considerations give rise to a predicted ratio of hadronic to leptonic activity of roughly 5:1. If greybody effects are switched on, particles are emitted according to greybody modified emission probabilities (which vary according to particle type and the dimensionality of spacetime). If greybody effects are switched off, particles are emitted according to constant blackbody emission probabilities. For ease of reference, the theoretical blackbody and greybody particle emissivities (emission probabilities) are shown in Table 4.1.

Primary partons emitted from generated black hole events were counted for various sets of initial parameter settings (M_P [TeV], M_{BH}^{min} [TeV], n). Table 4.2 shows the parton emission ratios obtained with event topology (2,2,3).

The generated blackbody emissivities are seen to agree with theoretical probabilities to within $\sim 10\%$. A sizable deviation ($> 30\%$) is however observed for charged leptons. Deviations from theoretical values may be attributed to several

factors. Firstly, the values in Table 4.2 include the remnant decay partons. With default settings `CHARYBDIS` terminates the black hole decay when the black hole mass M_{BH} falls below the Planck mass, upon which a 2-body decay is performed on the remnant. The remnant decay partons are assigned the same emission probabilities as the early emissions, but the remnant decay is constrained by the requirement that overall black hole charge and baryon number be conserved. Since the generated black holes may often have fractional charges (see Table 4.7), charge conservation may prevent charged leptons from being emitted in the final stage of the black hole decay[1].

The blackbody emission ratios of the unconstrained decay (excluding the remnant decay) and of the 2-body remnant decay for the same topology presented in Table 4.2, are shown in Table 4.3.

Contrary to expectations, Table 4.3 indicates that the unconstrained decay exhibits more radical deviations from the theoretical emissivities than the constrained remnant decay. These deviations are symptomatic of the chosen initial parameters and may be understood in terms of the low multiplicity of decay particles in the unconstrained decay. When the lower black hole mass limit (M_{BH}^{min}) is set at the Planck mass (`MINMSS=MPLNCK`) the generated black holes will on average only emit *one* particle before $M_{BH} < M_P$ after which an `NBODY` decay is performed on the black hole remnant, where `NBODY` may be set to any value between 2 and 5. In such cases, a choice of `NBODY=2` will therefore typically give a total of 3 decay partons, while `NBODY=3` will give 4 and so on. Increasing values of the parameter `NBODY` therefore increase parton level decay multiplicities correspondingly. Table 4.4 shows the relative particle emissivities (remnant included) for `NBODY`=2,3,4 and 5 with all other parameters as quoted in Table 4.2.

Table 4.4 suggests that the simulated particle emissivities tend toward the theoretical emission probabilities when the multiplicity of decay particles increases.

Independently of the chosen value of the parameter `NBODY`, the multiplicity of decay products may be augmented by increasing the threshold for black hole production M_{BH}^{min} and/or lowering the number of extra dimensions n.

[1] I am indebted to M.J.Palmer for his comments.

Particle species	Blackbody	
	Theory	Generator
Quarks	0.5654	0.5885 (+4%)
Gluons	0.1675	0.1857 (+11%)
Charged leptons	0.0942	0.0613 (-35%)
Neutrinos	0.0471	0.0405 (-14%)
Photons	0.0209	0.0229 (+10%)
Z^0 bosons	0.0314	0.0347 (-10%)
$W^{\pm}$ bosons	0.0628	0.0551 (-12%)
Higgs	0.0105	0.0113 (+8%)

Table 4.2: Relative emissivities of primary partons from generated black holes for the topology (M_P, M_{BH}^{min}, n) =(2,2,3). Bracketed values show percentage deviation from the theoretical emissivities.

Table 4.5 lists the particle emissivities obtained for event topology (2,9,3), as well as the extreme (2,13.9,2)[1].

Table 4.5 indicates that the relative proportions of particle types approach the theoretical values when increasing the multiplicity of primary partons emitted from the generated black hole. Deviations in high multiplicity events are found to be typically $< 10\%$ and may be attributed to the imposed conservation of charge and baryon number as well as kinematic constraints on massive particles (6).

It is important to bear in mind however, that a choice of initial parameters yielding a low average multiplicity per event may significantly constrain the black hole decay and alter the relative proportions of decay particles. If `CHARYBDIS` is permitted to generate black holes with masses down to the Planck scale (`MINMSS`=`MPLNCK`) only *one* particle is on average emitted before the remnant decay, giving a typical average total decay multiplicity of ∼`NBODY`+1. For the choice of parameters (2,2,3) an offset of $> 30\%$ is observed for charged leptons.

[1] These topologies are not intended to be indicative of typically black hole events at the LHC. They are "tools" to study the generator performance.

Particle species	Theory	Unconstrained decay	2-body remnant decay
Quarks	0.5654	0.4234 (-25%)	0.5334 (-6%)
Gluons	0.1675	0.2381 (+42%)	0.1982 (+18%)
Charged leptons	0.0942	0.0853 (-9%)	0.0816 (-13%)
Neutrinos	0.0471	0.0421 (-11%)	0.0413 (-14%)
Photons	0.0209	0.0312 (+49%)	0.0189 (-10%)
Z bosons	0.0314	0.0485 (+54%)	0.0372 (+18%)
$W^{\pm}bosons$	0.0628	0.0955 (-52%)	0.0719 (+15%)
Higgs	0.0105	0.0159 (+51%)	0.0124 (+18%)

Table 4.3: Relative blackbody emissivities of the unconstrained decay (decay excluding the remnant) and the remnant decay for initial parameters (M_P, M_{BH}^{min}, n) =(2,2,3). Bracketed values show percentage deviation from theoretical emissivities.

Particle species	Theory	NBODY			
		2 (10^5)	3 (10^4)	4 (10^3)	5 (10^2)
Quarks	0.5654	0.5885	0.5846	0.5729	0.5285
Gluons	0.1675	0.1857	0.1817	0.1849	0.2055
Charged leptons	0.0942	0.0613	0.0675	0.0715	0.1060
Neutrinos	0.0471	0.0405	0.0435	0.0480	0.0375
Photons	0.0209	0.0229	0.0230	0.0239	0.0147
Z bosons	0.0314	0.0347	0.0323	0.0312	0.0310
$W^{\pm}bosons$	0.0628	0.0551	0.0556	0.0564	0.0636
Higgs	0.0105	0.0113	0.0119	0.0113	0.0131

Table 4.4: Relative blackbody emissivities of primary partons for different `NBODY` terminations of the decay, with initial parameters (M_P, M_{BH}^{min}, n) =(2,2,3). Bracketed values indicate the number of events generated with each value of `NBODY`. (For `NBODY`>2 `CHARYBDIS/PYTHIA` is unstable with certain events causing the simulation to hang without error messages.)

Particle species	Theory	A	B
Quarks	0.5654	0.5981 (+6%)	0.5789 (+1%)
Gluons	0.1675	0.1641 (-2%)	0.1670 (-.3%)
Charged leptons	0.0942	0.0760 (-9%)	0.0869 (-8%)
Neutrinos	0.0471	0.0435 (-8%)	0.0466 (-1%)
Photons	0.0209	0.0205 (-2%)	0.0202 (-3%)
Z bosons	0.0314	0.0318 (-1%)	0.0318 (+1%)
$W^{\pm}bosons$	0.0628	0.0558 (-11%)	0.0586 (-7%)
Higgs	0.0105	0.0103 (-2%)	0.0100 (-5%)

Table 4.5: Relative emissivities of the decay products in two high multiplicity topologies: A:(M_P, M_{BH}^{min}, n) =(2,9,3) and B:(M_P, M_{BH}^{min}, n) =(2,13.9,2). Bracketed values show percentage deviation from theoretical emissivities.

PDG code	Particle species
1	d quark
2	u quark
3	s quark
4	c quark
5	b quark
6	t quark
11	e^-
12	ν_e
13	μ^-
14	ν_μ
15	τ^-
16	ν_τ
21	gluon
22	photon
23	Z^0 boson
24	W^+ boson
25	higgs boson

Table 4.6: Particle species and their PDG codes. Antiparticles have the corresponding negative values.

4.1.2 Charge Asymmetry

The relative proportions of primary partons emitted from the decaying black hole is discussed in 4.1.1. The distribution of different particle types (PDG codes) emitted from the black hole for the topology (M_P, M_{BH}^{min}, n) =(3,3,2) is plotted in Figure 4.1. The various particles and their PDG codes are listed in Table 4.6.

Two asymmetries are apparent in Figure 4.1. Firstly, there is an asymmetry between the number of quarks and antiquarks. Secondly, there is an excess of u,c and t quarks in the quark sector.

The quark-antiquark asymmetry may be understood as a charge asymmetry. Black holes are formed primarily from valence quarks and most black holes will therefore carry non-zero electric charge and baryon number. Table 4.7 provides a sample listing of five generated black hole events along with the charge (Q) and baryon number (B) of the incoming parton, the resulting black hole and the emitted decay particles.

Table 4.7 indicates how the imposed baryon number conservation creates a quark-antiquark asymmetry in the distribution of emitted particles. The first pair of events are of the form:

- $q\bar{q} \rightarrow BH \rightarrow x_1 + x_2 + ...$
  When the black hole is formed by a quark and an antiquark, $B_{BH} = 0$ and baryon number conservation requires an equal number of quarks and antiquarks in the decay.

The second pair of events are of the form:

- $qq \rightarrow BH \rightarrow x_1 + x_2 + ...$
  When the black hole is formed by a pair of quarks, $B_{BH} = 2/3$ and baryon number conservations requires the total decay to include at least two more quarks than antiquarks.

The last event is of the form:

- $qg \rightarrow BH \rightarrow x_1 + x_2 + ...$
  When the black hole is formed by a gluon and a quark, $B_{BH} = 1/3$ and baryon number conservation requires the total number of quarks in the decay to exceed the total number of antiquarks by at least one.

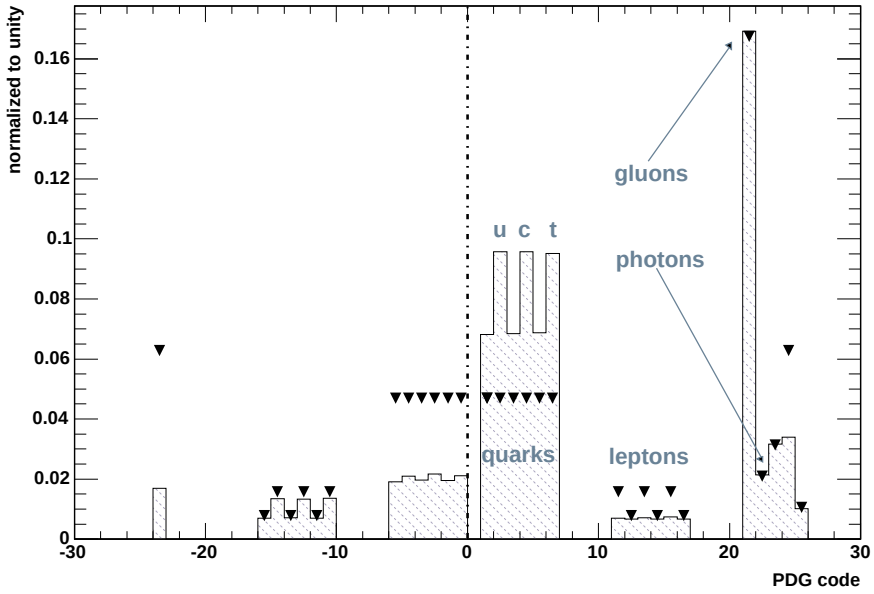

Figure 4.1: PDG code distributions of decay particles from generated black holes with initial parameters (M_P, M_{BH}^{min}, n) =(3,3,2). Triangles mark the theoretical blackbody emissivities.

.

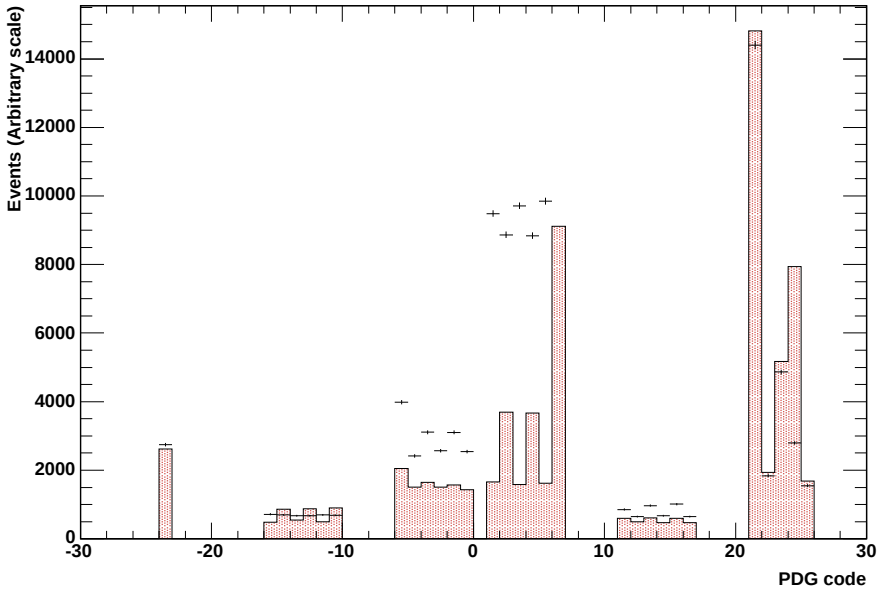

Figure 4.2: PDG code distributions of the unconstrained decay (cross-hatched) and the remnant decay (ticks) from generated black holes with initial parameters (M_P, M_{BH}^{min}, n) =(3,3,2).

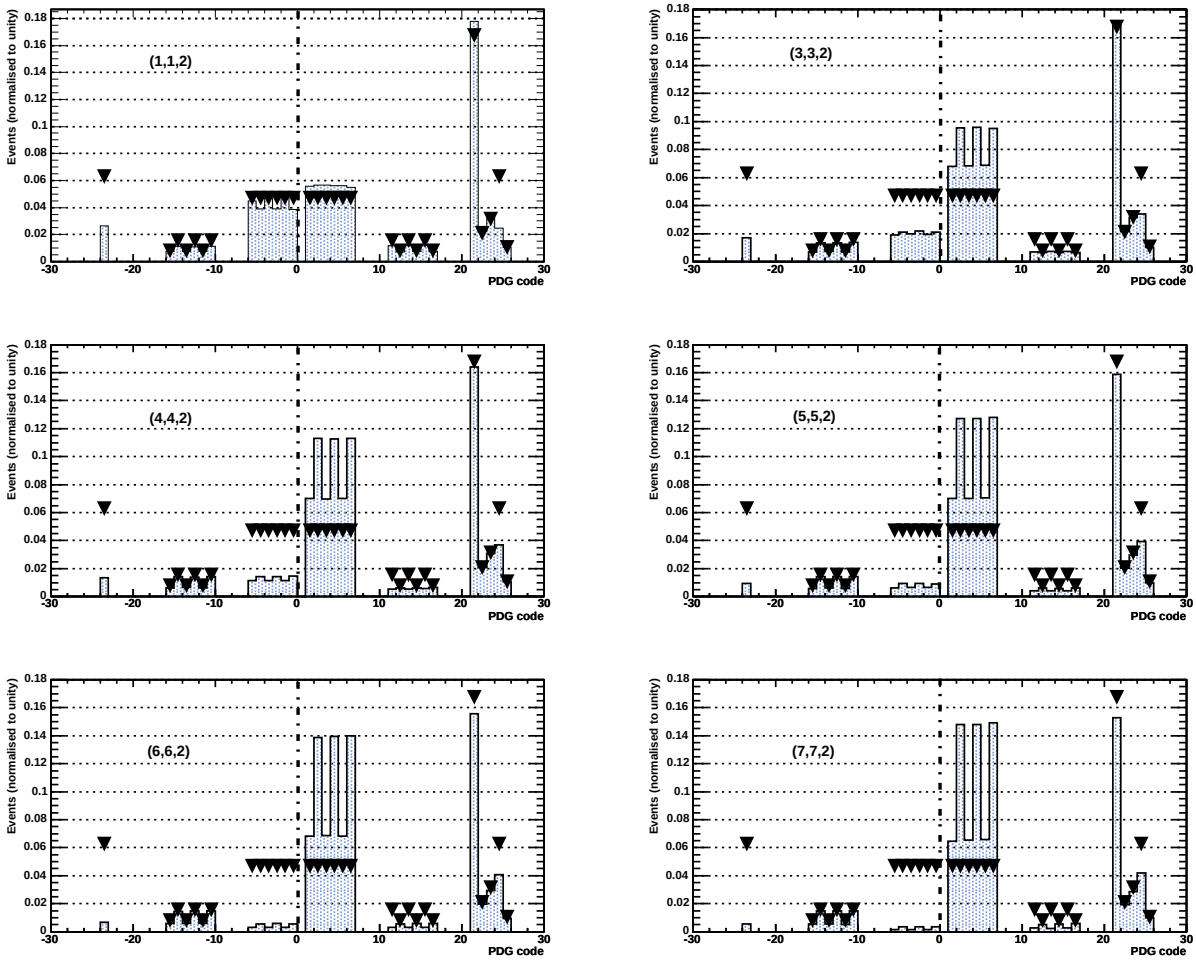

Figure 4.3: PDG code distributions of decay particles from black holes generated with different initial parameters (M_P, M_{BH}^{min}, n). Triangles mark the theoretical blackbody emissivities.

Event		Incoming partons			Emitted decay particles			
		d	$\bar{t}$	BH	e^-	$\bar{b}$	d	
1	Q	$-\frac{1}{3}$	$-\frac{2}{3}$	-1	-1	$+\frac{1}{3}$	$-\frac{1}{3}$	
	B	$+\frac{1}{3}$	$-\frac{1}{3}$	0	0	$-\frac{1}{3}$	$+\frac{1}{3}$	
		$\bar{b}$	u	BH	$\bar{d}$	g	u	
2	Q	$+\frac{1}{3}$	$+\frac{2}{3}$	+1	$+\frac{1}{3}$	0	$+\frac{2}{3}$	
	B	$-\frac{1}{3}$	$+\frac{1}{3}$	0	$-\frac{1}{3}$	0	$+\frac{1}{3}$	
		u	u	BH	W^+	t	b	
3	Q	$+\frac{2}{3}$	$+\frac{2}{3}$	$+\frac{4}{3}$	+1	$+\frac{2}{3}$	$-\frac{1}{3}$	
	B	$+\frac{1}{3}$	$+\frac{1}{3}$	$+\frac{2}{3}$	0	$+\frac{1}{3}$	$+\frac{1}{3}$	
		u	u	BH	Z^0	g	c	u
4	Q	$+\frac{2}{3}$	$+\frac{2}{3}$	$+\frac{4}{3}$	0	0	$+\frac{2}{3}$	$+\frac{2}{3}$
	B	$+\frac{1}{3}$	$+\frac{1}{3}$	$+\frac{2}{3}$	0	0	$+\frac{1}{3}$	$+\frac{2}{3}$
		u	g	BH	g	t	$\bar{\nu_\tau}$	
5	Q	$+\frac{2}{3}$	0	$+\frac{2}{3}$	0	$+\frac{2}{3}$	0	
	B	$+\frac{1}{3}$	0	$+\frac{1}{3}$	0	$+\frac{1}{3}$	0	

Table 4.7: Sample listing of charge and baryon number in five generated black hole events.

Baryon number conservation is seen to constrain the decay and generate an asymmetry in the number of quarks and antiquarks.

In a similar manner, the slight excess of u, c and t quarks may be understood in terms of the conservation of electric charge. Being formed largely from valence quarks, the black hole will normally carry a (fractional) electric charge. The remaining proton charge is expected to disappear along the beam pipe or at high $|\eta|$ (35). As described in Section 3.2, `CHARYBDIS` employs a charge bias to conserve overall black hole charge. During the black hole decay, if a charged particle is selected for emission, it is chosen so that the magnitude of the black hole charge decreases (6). Finally, the remnant decay is only accepted if it conserves overall charge *and* baryon number.

The second pair of events serve to indicate how a slight excess in u, c and t quarks arises. In both events the total black hole charge is $+\frac{4}{3}$. If `CHARYBDIS` decays the generated black hole by emitting a charged particle, it will preferentially select a positively charged particle in order to reduce the magnitude of the black hole charge. Furthermore, baryon number conservation requires the net decay to contain at least two more quarks than antiquarks. This leaves open the following options for the 2-body decay of the remnant with charge Q_{rem}:

- if $Q_{rem} = +\frac{4}{3}$, any pair combination of $u/c/t$ may be emitted
- if $Q_{rem} = +\frac{2}{3}$, either of $u/c/t$ may be emitted
- if $Q_{rem} = +\frac{1}{3}$, either of $u/c/t$ may be emitted together with either of $d/s/b$
- if $Q_{rem} = +1$, either of $e^+/\mu^+/\tau^+/W^+$ may be emitted

Figure 4.2 shows the PDG distribution of emitted particles of the decay excluding the remnant and the distribution of the 2-body remnant. The former indicates no d, s and b quark-antiquark asymmetry, as no baryon number conservation is imposed on this part of the decay. The excess quantities of u, c and t quarks, arise from the charge bias. The remnant distribution displays a slight excess of d, s and b quarks and a more prominent quark-antiquark asymmetry.

Figure 4.3 show distributions of decay particles from black holes generated with different lower production thresholds $M_{BH}^{min} = M_P$. The quark-antiquark

asymmetry and the $u/c/t$ substructure is seen to become more prominent at high energies, a pattern which reflects the parton distributions (PDFs) at high energies.

4.1.3 Parton Level Distributions

This section presents distributions of various properties and characteristics of the generated black holes and their decay products. Unless stated otherwise, time-variation and greybody effects are always switched off.

4.1.3.1 Black hole invariant mass distributions

The invariant mass of the generated black holes may be expressed as

$$M_{BH}^2 = (E_i + E_j)^2 - (\vec{p_i} + \vec{p_j})^2 \tag{4.1}$$

where i, j are the colliding partons.

Figure 4.4 shows invariant mass distributions of black holes generated with three different production thresholds. A range of masses are produced. In all cases, the threshold is set at the Planck mass ($M_{BH}^{min} = M_P$). Insofar, a strong dependence on M_P is observed. The distributions are seen to rise sharply at the production threshold[1] and fall off rapidly with increasing black hole mass. The majority of the generated events have masses within ~ 1 TeV of the production thresholds. It is worth noting that if $M_P = 1$ TeV and the region of semi-classical validity ($M_{BH} \gg M_P$) is interpreted to imply $M_{BH}^{min} \geq 5$ TeV, then Figure 4.4 indicates that only a very small fraction ($\sim 10^{-4}$) of events generated with a production threshold $M_{BH}^{min} \geq 1$TeV may be safely regarded as semi-classical.

Figure 4.5 shows that the invariant mass distributions depend only very weakly on the dimensionality of spacetime.

[1] The sharp rise is clearly artificial and reflects the need for theory of quantum gravity.

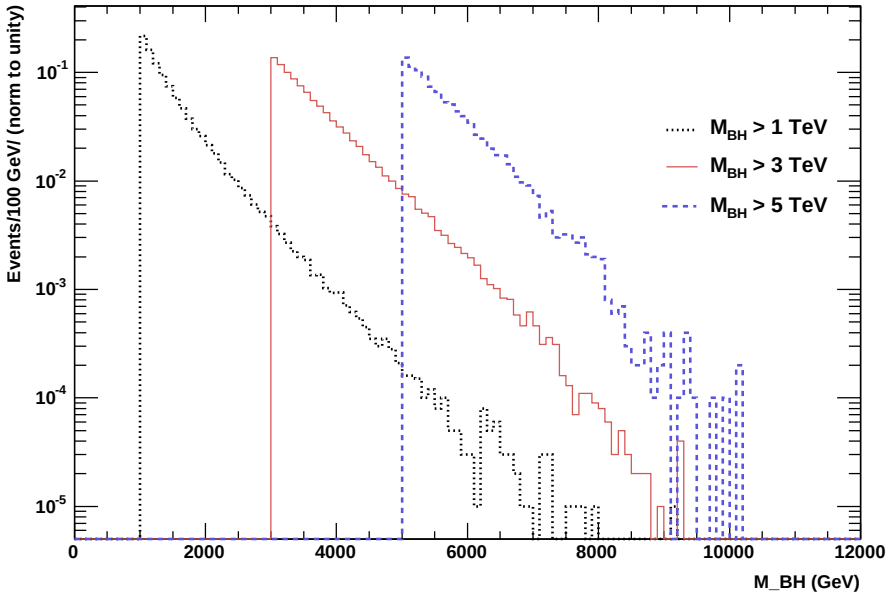

Figure 4.4: Invariant mass distributions for black holes generated with three different production thresholds: $M_{BH}^{min} \geq 1$ TeV (black-dotted), $M_{BH}^{min} \geq 3$ TeV (red-solid) and $M_{BH}^{min} \geq 5$ TeV (blue-dashed). In all cases, $M_{BH}^{min} = M_P$ and $n = 3$.

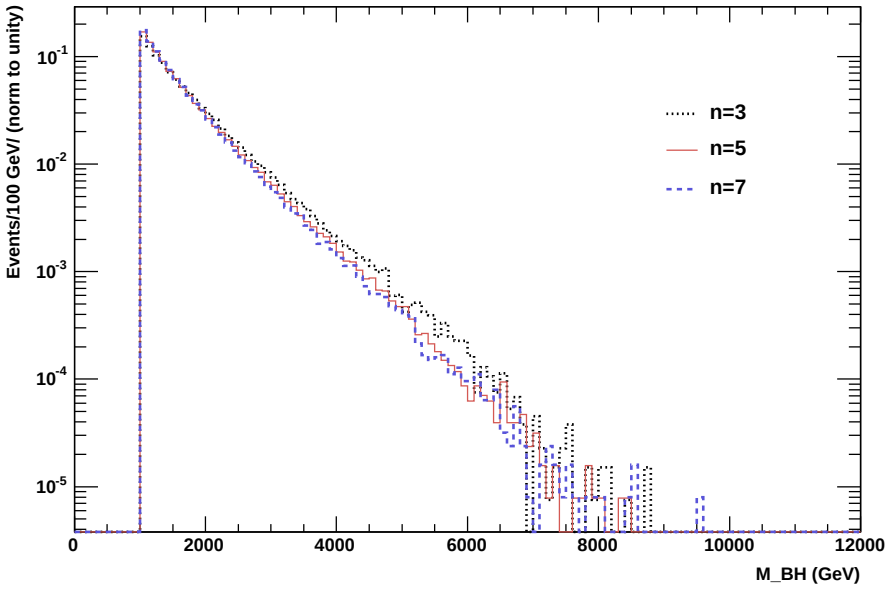

Figure 4.5: Invariant mass distribution for $n = 3$ (black-dotted), $n = 5$ (red-solid) and $n = 7$ (blue-dashed). In all cases, $(M_P, M_{BH}^{min}) = (1, 1)$.

4.1.3.2 Black hole charge (Q_{BH}) and baryon number (B_{BH})

The generated black holes inherit their charge from the incoming partons[1]. Figure 4.6 shows charge distributions for four different black hole production thresholds M_{BH}^{min}. Low production thresholds ($\sim$ 1 TeV) are seen give black holes with a range of different charges. Higher production thresholds shift the distributions toward $\langle Q_{BH} \rangle \sim +\frac{4}{3}$. This pattern reflects the CTEQ5L PDFs at high x, where the u valence quark distribution is most dominant. By contrast, high energy, hard scattering interactions at the LHC are expected to occur mainly through valence u quarks and gluons. The average black hole charge at the LHC is therefore estimated at $\langle Q_{BH} \rangle \sim +\frac{2}{3}$.

The black hole baryon number shows a similar PDF governed energy dependence. Baryon number distributions for the same topologies shown in Figure 4.6, are plotted in Figure 4.7. With high production thresholds, the majority of generated black holes carry a baryon number of $+\frac{2}{3}$.

4.1.3.3 Multiplicity of decay products

The average multiplicity of particles emitted by a black hole in the Hawking evaporation phase, may be approximated by (33):

$$\langle N \rangle \approx \frac{M_{BH}}{2T_H} \tag{4.2}$$

For any fixed M_P and n, the multiplicity of decay products will grow with increasing black hole mass, as shown in Figure 4.9. Conversely, for any fixed M_P and M_{BH} the decay multiplicity decreases with increasing numbers of extra dimensions. The latter effect may be attributed to the fact that high-dimensional black holes are hotter (have higher Hawking temperatures) and hence by Equation 4.2 have lower average multiplicities. Figure 4.8 shows multiplicity distributions for various n with (M_P, M_{BH}^{min}) =(1,1). Although a range of masses are generated, the majority lie close to the production threshold and the number of decay particles is seen to drop significantly with increasing n.

[1] In a real black hole forming collision, the resulting black hole would inherit its charge from whatever is trapped behind the horizon.

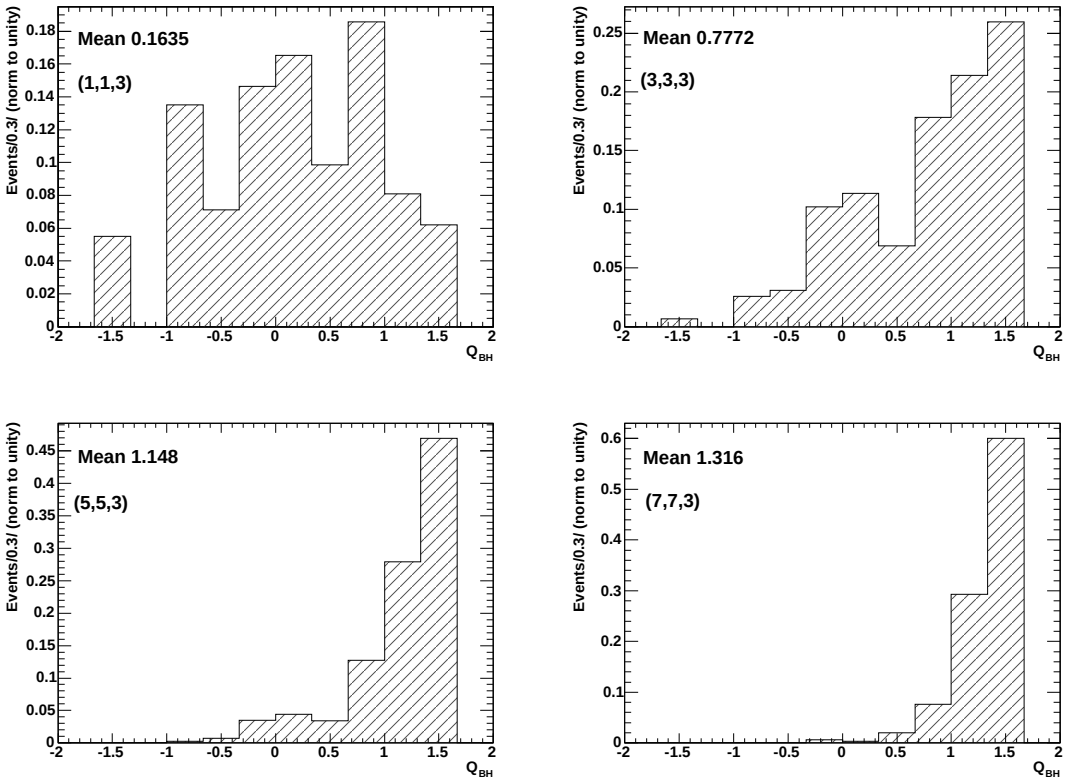

Figure 4.6: Black hole charge (Q_{BH}) distributions for various parameters (M_P, M_{BH}^{min}, n).

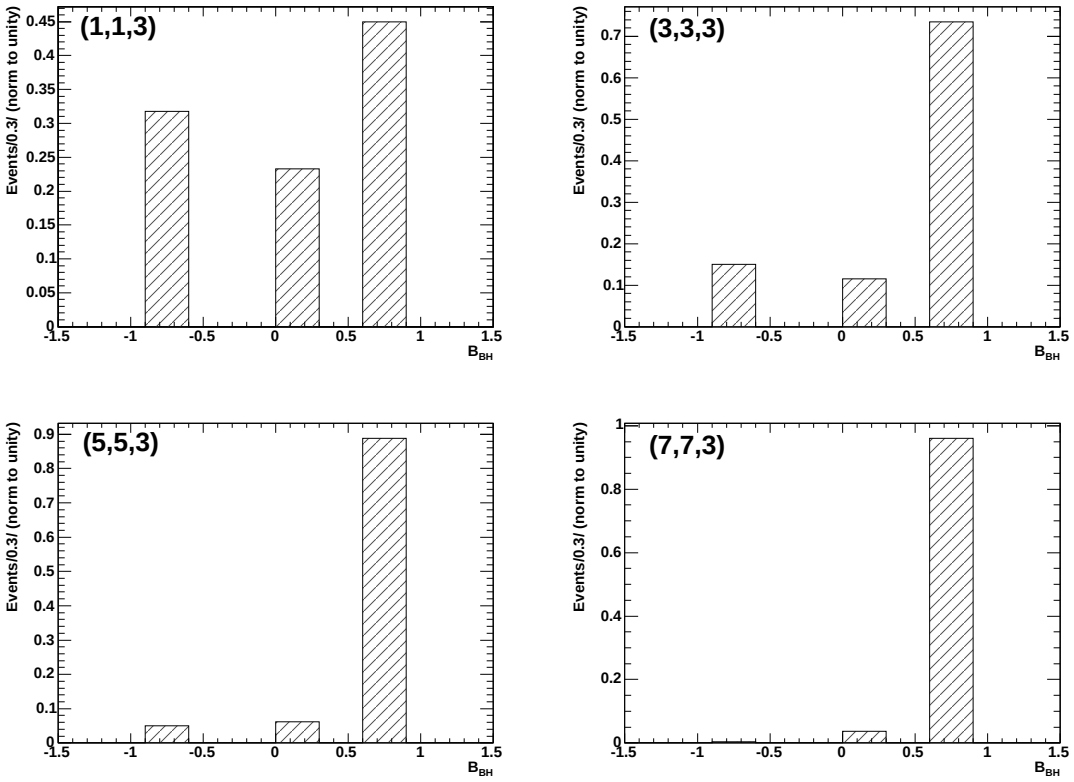

Figure 4.7: Black hole baryon number (B_{BH}) distributions for various parameters (M_P, M_{BH}^{min}, n).

Black holes generated in the semi-classical regime $M_{BH} \gg M_P$ will typically yield high multiplicity (> 10) and high sphericity events. Figure 4.9 indicates that black holes with masses close to the fundamental Planck mass will typically yield much lower multiplicities and are further expected to be dominated by quantum gravity effects. To avoid the uncertainties of the quantum gravity regime, it is clear that an analysis of black hole events at the LHC should limit itself to events with large multiplicities. These considerations are guiding for the analyses presented in later sections.

4.1.3.4 Decay p_T distributions

Figure 4.11 shows the distribution of transverse momenta for particles emitted by black holes generated at three different production thresholds. Even relatively light black holes will produce decay products with transverse momenta of several hundred GeV. As the black holes become more massive, the p_T distribution stretches to higher p_T values, giving decay products with transverse momenta in the TeV range. A large total transverse momentum is a characteristic feature of black hole decays at the LHC.

4.1.3.5 Time variation and Greybody effects

As discussed in Section 1.3.3.2, the black hole temperature T_H increases as the Schwarzschild decay phase evolves. Since energy distribution of the emitted particles peaks at $\sim T_H$, the time evolution of T_H is expected to harden the parton level energy spectra.

Greybody factors quantify the probability that an emitted particle of a given energy will successfully escape the gravitational pull of the black hole. Their spin dependence implies that the spectral changes will differ for particles of different spin. The effect of time variation and greybody factors is discussed in (6; 29), and some of the plots produced therein are replotted here for illustrative purposes.

Figure 4.10 shows the impact of these effects on the parton level energy spectra of spin-0 Higgs bosons, spin-$\frac{1}{2}$ $e^{\pm}$ and spin-1 γ from the decay of black holes generated in the restricted mass range 5 TeV $\leq M_{BH} \leq$ 5.5 TeV with $M_P = 1$ TeV. The inclusion of greybody effects is seen to slightly soften the spectra of

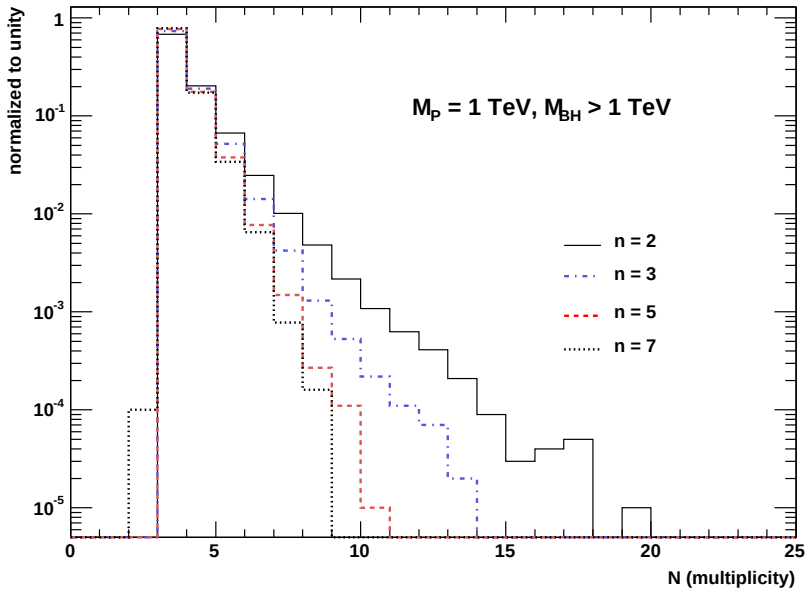

Figure 4.8: Decay multiplicities for various n with (M_P, M_{BH}^{min}) =(1,1).

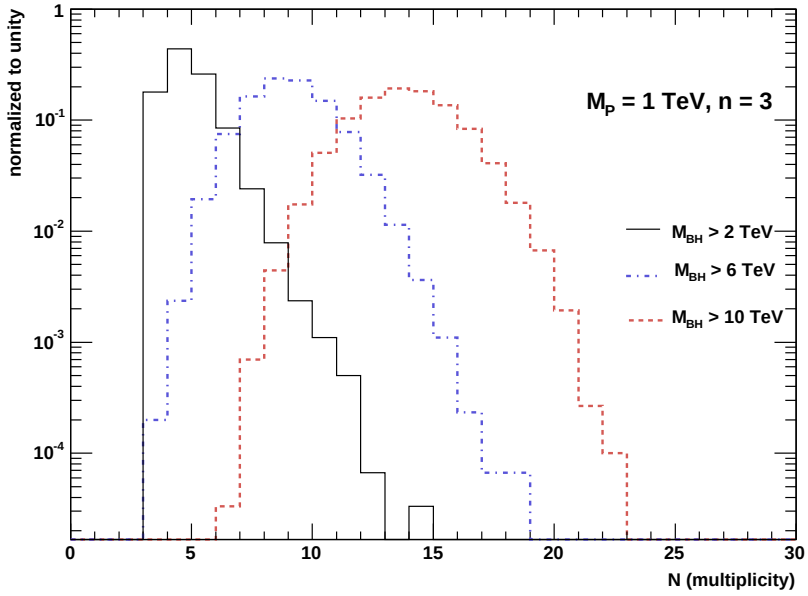

Figure 4.9: Decay multiplicities for various lower production thresholds (M_{BH}^{min}) with (M_P, n) =(1,3).

scalars and fermions, while hardening the spectra of gauge bosons. The effect of time variation is to slightly harden the spectra of all particle species, as expected. These spectral changes are exacerbated in a wider (unrestricted) black hole mass range, as is shown in Figure 4.12.

Figures 4.10 and 4.12 indicate that analyses which aim to make use of the black hole energy spectra to derive information about the original black hole state, cannot fully disregard the effects of a time-evolving T_H and greybody modified emission spectra. These considerations are discussed in greater detail in (35). They are however less important for discovery. Their impact on the ATLAS sensitivity to black holes is treated in Section 4.4.

4.2 Black hole decays in ATLAS

While Section 4.1.3 focused on the characteristics of black hole events at the parton level, the current section will discuss black hole signatures at the level of the ATLAS detector. After hadronisation, fragmentation and decay, the generated events are passed through the `ATLFAST` parametrization of the ATLAS detector, as described in Section 3.3. `ATLFAST` is unfortunately not optimized, nor tuned to the high energies characteristic of black hole events and further full simulation studies are required to draw more accurate pictures of detector response and resolutions in this regime. Even so, `ATLFAST` simulations should adequately capture the overall features of black hole observables in ATLAS. The aim of this section is to trace some of the expected experimental signatures discussed in Section 1.3.4 on the detector level.

4.2.1 Multiplicity

Black hole events are characterised by large multiplicities. On the level of the ATLAS detector, the multiplicity of an event is understood as the total number of jets, electrons, muons and photons in the event[1]. As seen in Figure 4.13, the multiplicity of a black hole event will depend on the relative mass of the

[1] The detector level multiplicity should not be confused with the number of particles emitted by the black hole at the parton level.

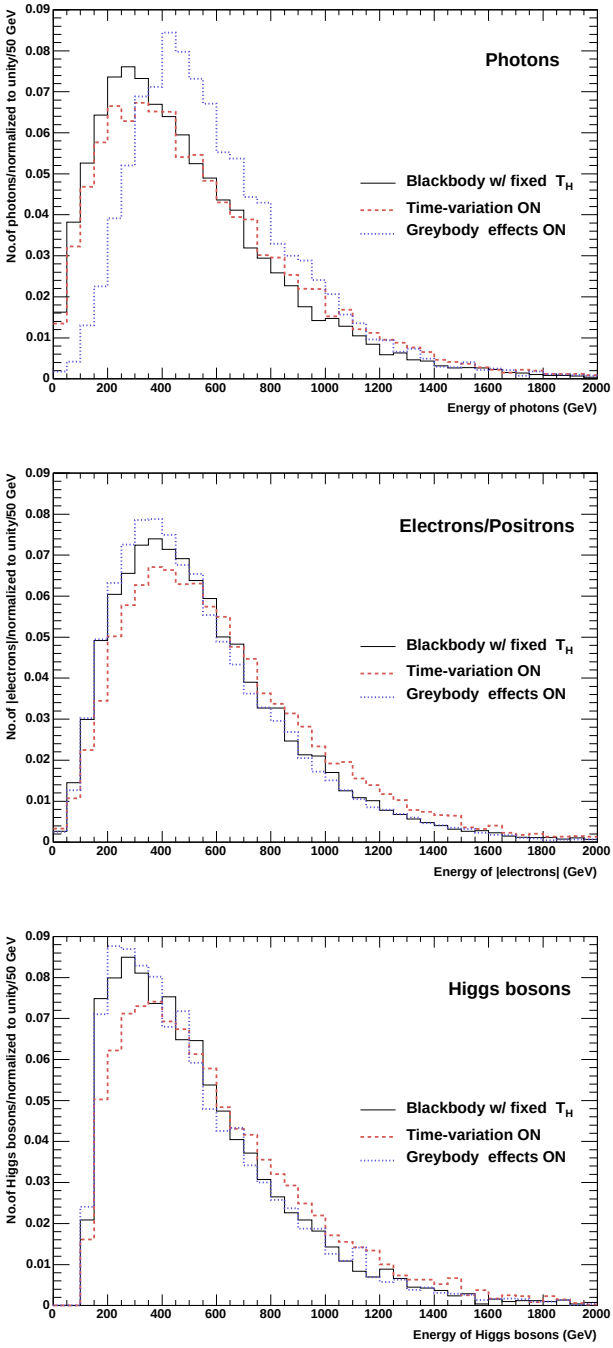

Figure 4.10: Impact of a time-evolving T_H and greybody effects on the parton level energy spectra of spin-1 photons (top), spin-$\frac{1}{2}$ electrons/positrons (middle) and spin-0 Higgs bosons (bottom) emitted by ~ 5 TeV black hole with $M_P = 1$ TeV and $n = 2$. Black-solid lines depict blackbody spectra with fixed T_H, red-dashed lines depict blackbody spectra with time-varying $T_H(t)$ and blue-dotted lines show greybody spectra with fixed T_H.

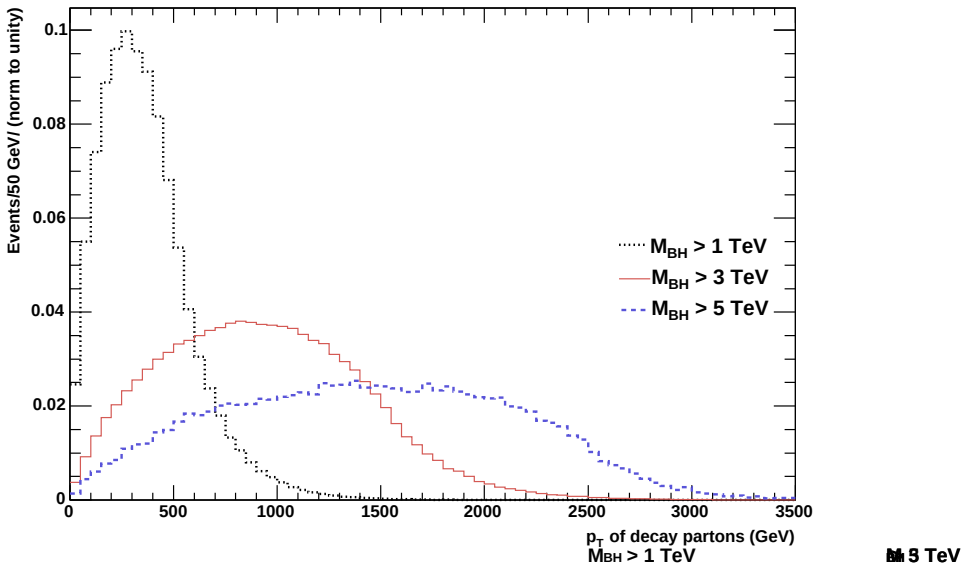

Figure 4.11: p_T spectra of primary partons, leptons and gauge bosons emitted by black holes with three different production thresholds: $M_{BH}^{min} \geq 1$ TeV (black-dotted), ≥ 3 TeV (red-solid) and ≥ 5 TeV (blue-dashed). In all cases $M_{BH}^{min} = M_P$ and $n = 3$. The bin integral of all the distributions is normalised to unity.

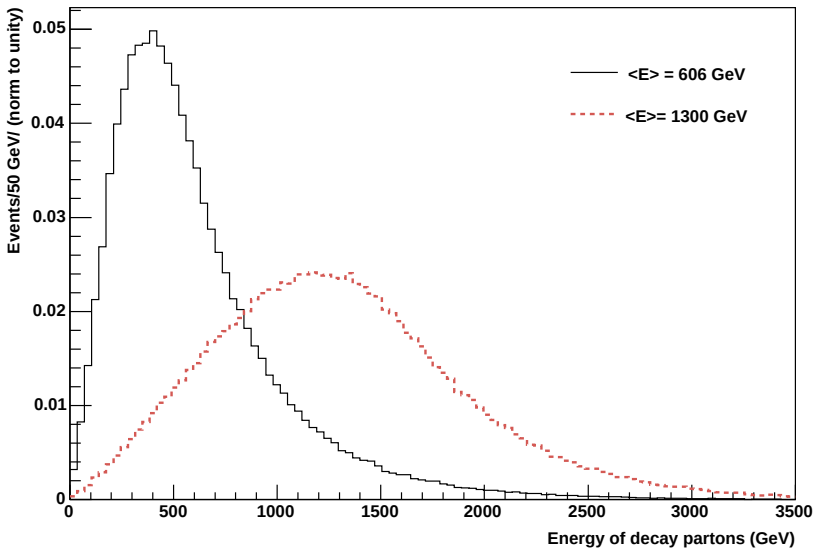

Figure 4.12: Total energy spectra of decay particles from black holes generated with (M_P, M_{BH}^{min}, n) =(1,1,3). The black-solid line shows the fixed temperature, blackbody distribution. The red-dashed line shows the varying temperature, greybody distribution.

black hole with respect to the fundamental Planck mass and increase with the black hole mass. The average total event multiplicity for black holes generated with different production thresholds and fixed $M_P = 1$ TeV, is shown in Figure 4.14 in the case of three and seven extra dimensions. A slight decrease in event multiplicity is observed for increasing numbers of extra dimensions. Average total multiplicities are listed in Table 4.8, along with average jet, lepton photon multiplicities. Table 4.8 indicates that if the fundamental Planck mass is as low as ∼1 TeV, then black hole events will yield multiplicities of ∼10-20, the large majority of which will be jets. Due to the relatively high degree of sphericity, such high multiplicity events should be experimentally manageable with good jet separation and electron/photon isolation. Further full simulation studies are required to verify this, but are sadly out of scope for this thesis.

Table 4.8 further indicates a much larger ratio of hadronic to leptonic activity than the predicted ratio of roughly 5:1. For all topologies, the ratio $\langle N_{jet}\rangle/\langle N_{lep}\rangle$ is found to be ~ 23. This result reveals the weakness of `ATLFAST`. As described in Section 3.3, after the removal of electron and photon clusters `ATLFAST` labels all unidentified clusters as jets. This does not reflect a true experimental situation and a proper handle on black hole jet topologies can only be attained through further full simulation studies[1].

Table 4.9 lists average multiplicities obtained when the lower threshold for black hole production is set to the fundamental Planck scale. Again, the events are seen to be dominated by jets. In such cases, the average total multiplicity will be lower as the majority of black holes will have masses close to the fundamental Planck mass. This will be true for any value of M_P, and consequently event multiplicities are roughly constant for increasing M_P (and n).

[1]From the experimental viewpoint, a jet is not defined in strict terms. Jet reconstruction and topologies are sensitive to the jet algorithms employed. Black hole events may require refined algorithms.

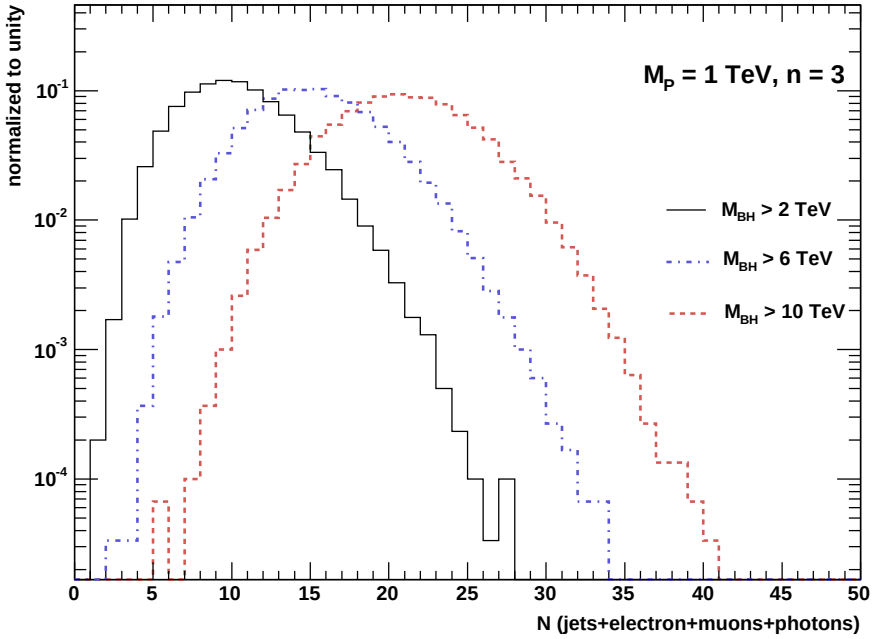

Figure 4.13: Multiplicity distributions for various lower production thresholds and $(M_P, n) = (1, 3)$.

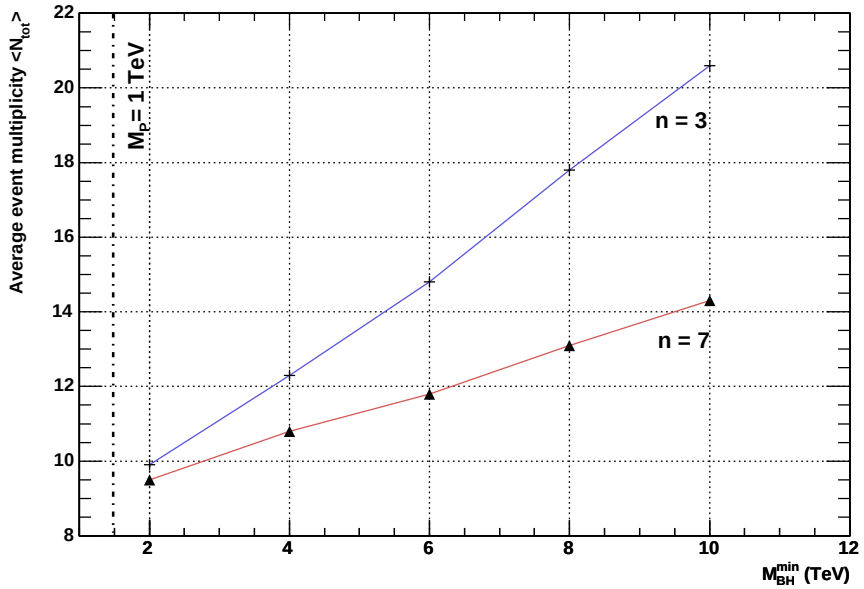

Figure 4.14: Average multiplicity as a function of the lower production threshold M_{BH}^{min} with $M_P = 1$ TeV, for $n = 2$ (blue-cross) and $n = 7$ (red-triangle).

	$M_{BH} \geq 2$ TeV		$M_{BH} \geq 4$ TeV		$M_{BH} \geq 6$ TeV		$M_{BH} \geq 8$ TeV		$M_{BH} \geq 10$ TeV	
	$n=3$	$n=7$	$n=3$	$n=7$	$n=3$	$n=7$	$n=3$	$n=7$	$n=3$	$n=7$
$\langle N_{tot} \rangle$	9.9	9.5	12.3	10.8	14.8	11.8	17.8	13.1	20.6	14.3
$\langle N_{jet} \rangle$	9.3	8.9	11.5	10.1	13.9	11.1	16.7	12.3	19.4	13.5
$\langle N_{lep} \rangle$	0.4	0.3	0.5	0.4	0.6	0.4	0.7	0.5	0.8	0.5
$\langle N_{pho} \rangle$	0.2	0.3	0.3	0.3	0.3	0.3	0.4	0.3	0.4	0.3

Table 4.8: Average jet, lepton, photons and total event multiplicities for various lower production thresholds and fixed $M_P = 1$ TeV.

$M_{BH}^{min} = M_P$	$M_{BH} > 1$ TeV		$M_{BH} > 3$ TeV		$M_{BH} > 5$ TeV		$M_{BH} > 7$ TeV	
	$n=2$	$n=7$	$n=2$	$n=7$	$n=2$	$n=7$	$n=2$	$n=7$
$\langle N_{tot} \rangle$	8.8	8.6	8.0	8.0	7.5	7.5	7.1	7.2
$\langle N_{jet} \rangle$	8.3	8.1	7.6	7.6	7.1	7.1	6.8	6.9
$\langle N_{lep} \rangle$	0.3	0.3	0.2	0.2	0.2	0.1	0.1	0.1
$\langle N_{pho} \rangle$	0.2	0.2	0.2	0.2	0.2	0.2	0.2	0.2

Table 4.9: Average jet, lepton, photon and total event multiplicities for various M_P. In all cases $M_{BH}^{min} = M_P$.

4.2.2 Event shape

High multiplicity black holes events will tend to have spherical event shapes[1]. A measure for the spherical character of an event is provided by the event shape variable R_2. R_2 is defined through a Fox-Wolfram moment ratio:

$$R_2 \equiv \frac{H_2}{H_0} \tag{4.3}$$

where the Fox-Wolfram moments are given as

$$H_k \equiv \sum_{i,j} \frac{|p_i||p_j|}{E_{vis}^2} P_k(cos\phi_{i,j}). \tag{4.4}$$

In Equation 4.4, p_i and p_j are the momenta of particles i and j respectively evaluated in the black hole rest frame where the two are separated by an opening

[1]Large mass black holes will have very small boosts. Less massive black holes are likely to have a moderate boost factor. Low boosts and high multiplicity, together provide for a high sphericity.

angle $\phi_{i,j}$. $P_k(x)$ are the Legendre polynomials and E_{vis} is the total visible energy of the event in the rest frame of the black hole.

The event shape variable R_2 will range from 0 to 1 ($0 \leq R_2 \leq 1$) and tend to zero ($R_2 \to 0$) for highly spherical event topologies. By contrast $R_2 \to 1$ represents back-to-back like event topologies.

Figure 4.15 shows R_2 distributions for black hole events generated with different lower thresholds and fixed (M_P, n) =(1,2). Figure 4.16 show the same distributions with (M_P, n) =(1,7). Large mass black holes are seen to be more spherical than black holes with masses close to the fundamental Planck mass. For higher values of n, events become less spherical, an effect which is more pronounced for large mass black holes. The spherical event shapes may be related to the magnitude of the event multiplicity and the black hole boost. Large mass black hole events enjoy larger multiplicities and smaller boosts than low mass black holes, and are consequently more spherical. As the multiplicity drops with increasing n, events become somewhat less spherical with increasing numbers of extra dimensions. Figure 4.17 explicitly shows the relation between the total event multiplicity and the event shape variable R_2. Events with multiplicities in excess of ∼15 are seen to have very spherical topologies ($R_2 \lesssim 0.2$). Black holes with masses close to the fundamental Planck mass, typically produce events with lower multiplicities and far less spherical event topologies. Even so, such low multiplicity events are found to be separable from SM hard QCD processes, as shown in Figure 4.18.

4.2.3 Sum p_T and p_T^{miss}

The high energies associated with black hole production allow for fairly energetic ($\sim$ 1 TeV) decay products, as shown in in the parton level distribution in Figure 4.12. Since black hole decays are dominated by jets, the majority of this energy should be observable as a large total transverse momentum in the ATLAS calorimetry. Figure 4.19 shows the total transverse momentum ($\sum p_T$) distributions for various black hole production thresholds and SM QCD. The $\sum p_T$ is seen to increase with black hole mass (and peak roughly a the production threshold).

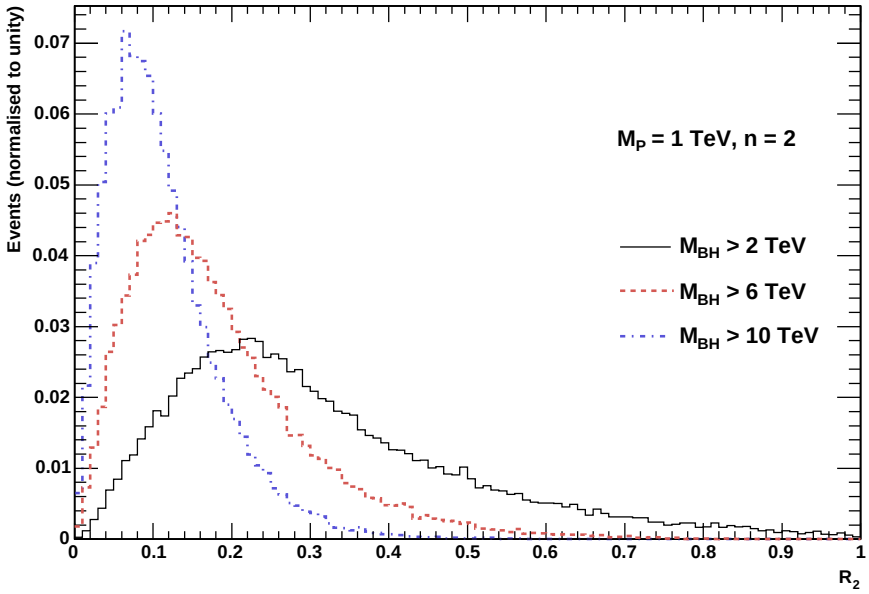

Figure 4.15: R_2 distributions for various production thresholds and fixed (M_p, n) =(1,2).

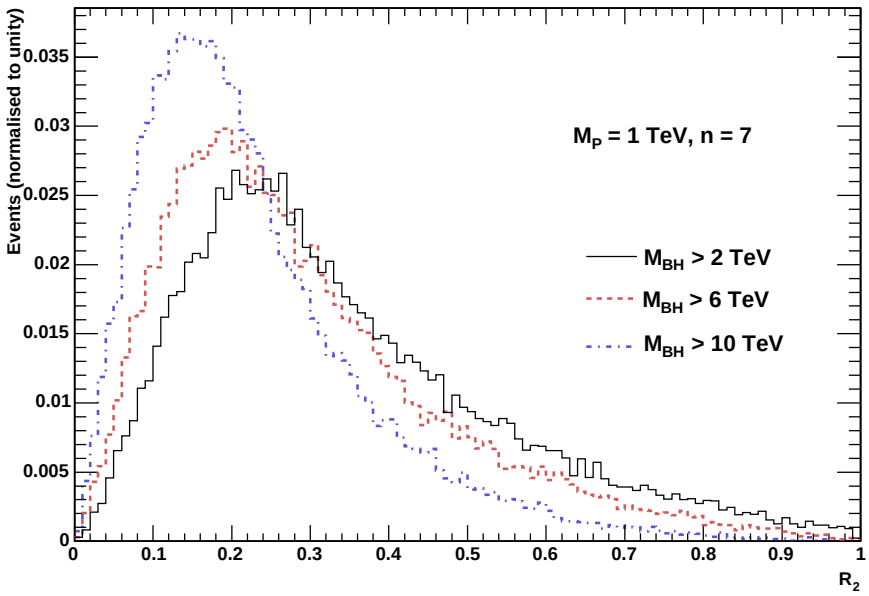

Figure 4.16: R_2 distributions for various production thresholds and fixed (M_p, n) =(1,7).

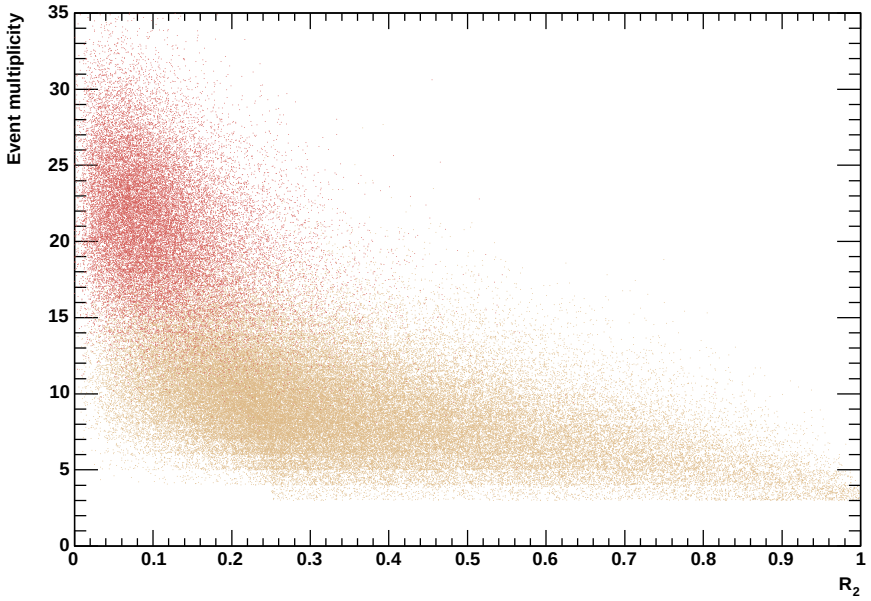

Figure 4.17: Relation between event multiplicity and R_2 for two different production thresholds: M_{BH}^{min} =10 TeV (red) and M_{BH}^{min} =1 TeV (yellow). In both cases $(M_P, n) = (1, 2)$.

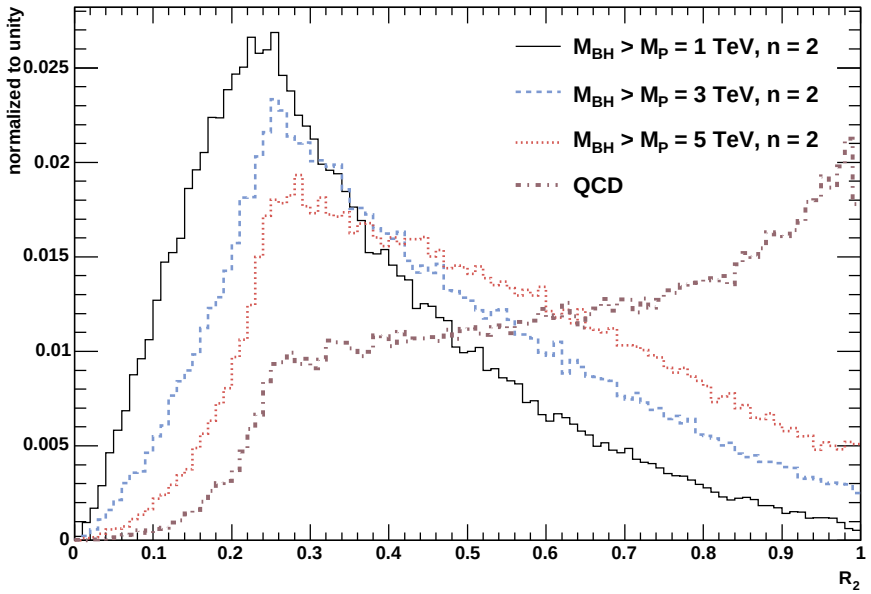

Figure 4.18: R_2 distributions for various production thresholds and hard QCD. In all distributions, $M_{BH}^{min} = M_P$.

Although, neutrinos have only $\sim 5\%$ probability of being emitted, some black holes may occasionallly emit neutrinos which carry away a significant portion of the black hole energy. As can be seen from Figure 4.20, the p_T^{miss} may at times be on the order of several TeV and exceed expectations from SUSY processes. However, the large majority of black hole events ($\sim 90\%$) are seen to have $p_T^{miss} < 100\text{GeV}$[1].

4.3 The ATLAS sensitivity to black holes

The feasibility of detecting black holes produced in particle collisions at the LHC is evaluated in (1). The authors of (1) developped their own generator[2] for this purpose with a less sophisticated modelling of the black hole decay than that offered by `CHARYBDIS`. The former notably does not take into account the effects of

- The time variation of the Hawking temperature T_H.
- Greybody modified emission spectra.
- The black hole recoil against emitted particles.

The following analysis makes use of `CHARYBDIS` to perform a study along the lines of (1). The first part (Section 4.3.3) of the analysis attempts to reproduce the results (1) with all special features of `CHARYBDIS` switched off. The second part (Section 4.4) of the analysis attempts to evaluate the impact of a time evolving Hawking temperature T_H and greybody factors on the ATLAS sensitivity to black holes at the LHC.

[1] Although not considered in this analysis, it is of course possible that the black holes also decay to SUSY particles, whereby a larger fraction of events would be characterised by a sizeable p_T^{miss}.

[2] The features of this generator are described in (1).

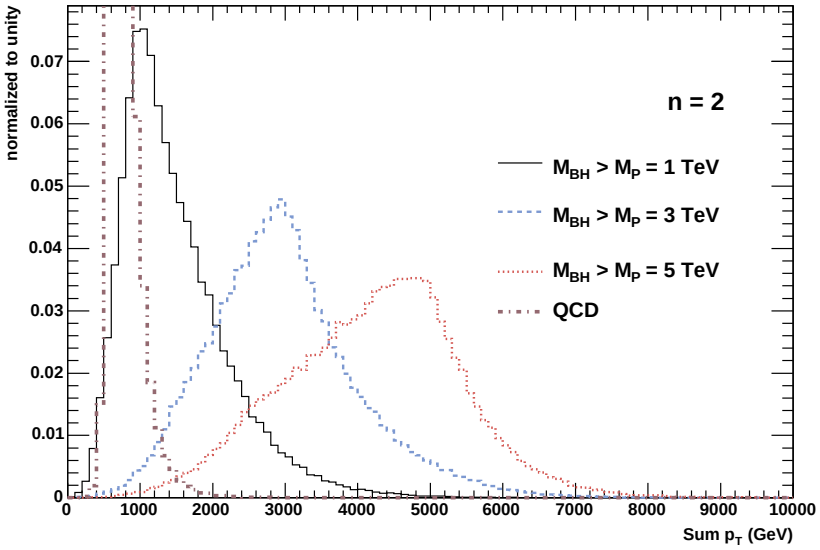

Figure 4.19: The distribution of $\sum p_T$ for various production thresholds and hard QCD.

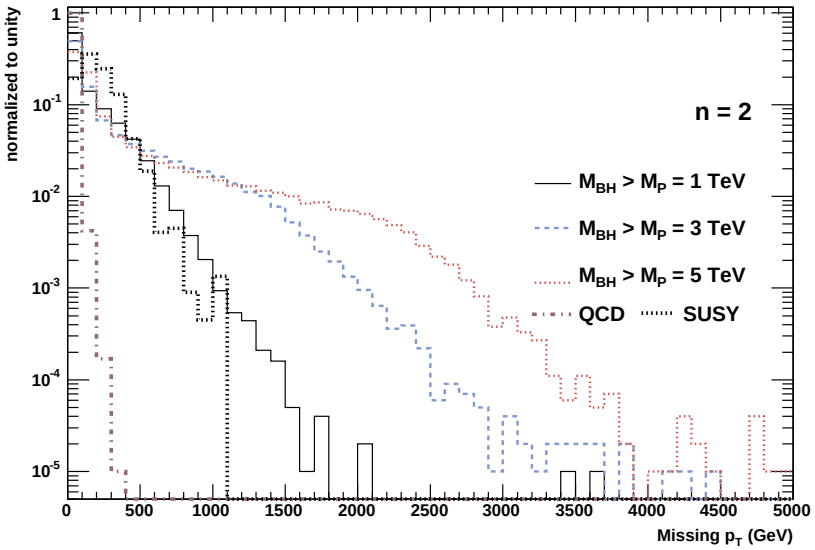

Figure 4.20: The distribution of p_T^{miss} for various black hole production thresholds, hard QCD and SUSY.

MINMSS	MPLNCK	Black hole production threshold set to M_P
MAXMSS	14000.	Upper limit on the black hole mass ($M_{BH}^{gen} \leq 14$TeV)
TIMVAR	.FALSE.	Fixed Hawking temperature T_H
GRYBDY	.FALSE.	Blackbody emission spectra
MSSDEC	3	Decay to all SM particles, including Higgs
KINCUT	.FALSE.	NBODY decay of remnant when $M_{BH} < M_P$
NBODY	2	2-body decay of remnant

Table 4.10: CHARYBDIS settings used in the generation of signal samples.

4.3.1 Event Generation

The simulation tools employed in this analysis are described in Chapter 3. All black hole events were generated with CHARYBDIS 1001 interfaced to PYTHIA 6.224 and passed through ATLFAST 1.10 for detector response simulations. SM background processes were generated in a similar fashion using PYTHIA 6.224 and ATLFAST 1.10. ATLFAST settings were as described in Section 3.3. In most cases, data in excess of 10 fb^{-1} was generated, which corresponds to one year of LHC running at low luminosity.

4.3.1.1 Signal samples

For consistency and to enable comparison, signal samples were generated across the same parameter space employed in (1). The parameter space is spanned by the fundamental Planck mass M_P and the number of extra dimensions n:

$$(M_P(\text{TeV}), \text{n}) = \{1,3,4,5,6,7\} \times \{2,3,5,7\} \quad (4.5)$$

$$= \{(1,2);(1,3);(1,5);(1,7);(3,2);...\} \quad (4.6)$$

CHARYBDIS options were adjusted to most closely resemble the generator described in (1). The settings used in the generation of all signal samples are listed in Table 4.10

Remaining options were all set to default values, as described in (29). Notice that, for consistency with (1), the lower threshold for black hole production was set to the fundamental Planck mass such that the semi-classical model is employed

also in the invalid regime $M_{BH} \sim M_P$. The significance of the this choice of parameters is further discussed in Section 4.5.1.

Details about generated signal samples are given in Table 4.11 with cross sections obtained from the output of PYTHIA. Table 4.11 indicates that cross sections for black hole production at LHC are fairly large for new physics standards, even for more massive black holes ($M_{BH} > 5$TeV). The cross sections show a strong dependence on the value of the fundamental Planck scale M_P.

For $M_P = 1$ TeV, the cross sections are particularly large and comparable to SM hard QCD processes (see Table 4.12). If $M_P \sim 1$ TeV, these numbers indicate that the LHC will qualify as a black hole factory. At an integrated luminosity of 10 fb^{-1}, these cross sections correspond to data on the order of 100 million events for each point $(1, n)$. Even though a million events were generated at each of these points, the scale factors are still very large[1].

4.3.1.2 Background samples

As discussed in Section 4.2, black hole events are characterised by several hard jets and possibly a few hard prompt leptons. SM processes involving final state jets and leptons are therefore selected as potential backgrounds to black hole events at the LHC. Details about the generated background samples employed in this analysis are listed in Table 4.12 along with their corresponding PYTHIA subprocess codes.

As in (1), kinematical cuts were applied at generation level:

- CKIN(1):
  The lower limit for the center-of-mass energy of the incoming partons was set to 50 GeV for all the generated background samples ($\sqrt{(}\hat{s}) \geq 50$ GeV)

- CKIN(3):
  Various lower limits for the transverse momentum $\hat{p}_T^{min}$ in the rest frame of the incoming partons were imposed on generated background samples. The cuts are listed in Table 4.12.

[1] With the fast simulation it is of course possible to increase the statistics in these points. However, given the number of (M_P, n) points considered, this was not done.

M_P (TeV)	n	σ (fb)	N_{gen}	Scale factor
1	2	2.41×10^7	10^6	240.7
1	3	2.11×10^7	10^6	211.5
1	5	2.12×10^7	10^6	212.3
1	7	2.34×10^7	10^6	233.7
3	2	4.10×10^4	5×10^5	0.821
3	3	3.70×10^4	5×10^5	0.740
3	5	3.81×10^4	5×10^5	0.762
3	7	4.24×10^4	5×10^5	0.848
4	2	4650	10^5	0.465
4	3	4230	10^5	0.423
4	5	4380	10^5	0.438
4	7	4880	10^5	0.488
5	2	625	10^5	0.06
5	3	572	10^5	0.06
5	5	594	10^5	0.06
5	7	671	10^5	0.07
6	2	88.1	10^5	0.009
6	3	81.1	10^5	0.008
6	5	84.7	10^5	0.008
6	7	95.0	10^5	0.009
7	2	11.8	10^5	0.001
7	3	11.0	10^5	0.001
7	5	11.4	10^5	0.001
7	7	12.8	10^5	0.001

Table 4.11: Signal samples with cross sections, number of generated events (N_{gen}) and scale factors. In all of the above, the effects of time variation and greybody factors is switched off.

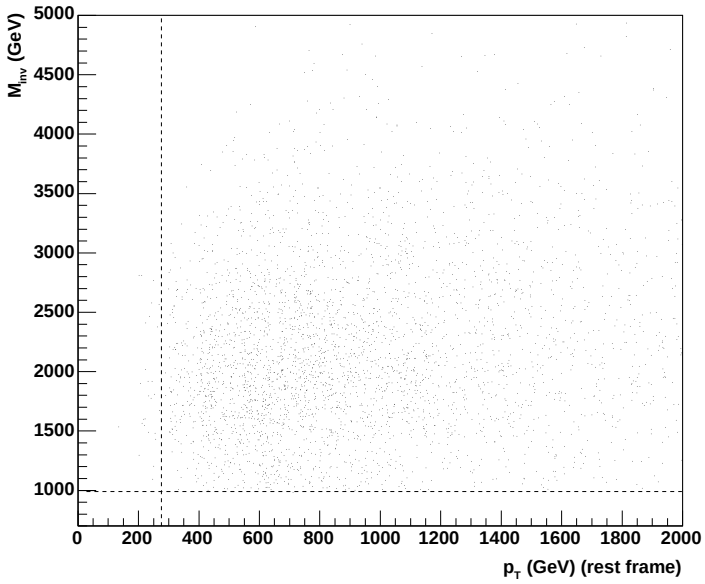

Figure 4.21: Effect of a kinematical cut (`CKIN(3)`) at 280 GeV (vertical line) on the transverse momentum in the rest frame of the incoming partons for hard QCD events. The cut is seen to produce reconstructed invariant masses in TeV range after selection criteria. (The horizontal line represents a cut on the reconstructed invariant mass). See text for details on the reconstruction.

The kinematical cuts are the same as those quoted in (1). Figure 4.21 shows that the `CKIN(3)` cut for hard QCD is well optimised for the mass points (M_P, n) listed in Table 4.11. A harder cut would ease the generation of large statistics, but would also quickly remove background.

Note that $b\bar{b}$ events were added to the list of background samples presented in (1).

Only backgrounds arising from Standard Model processes are listed in Table 4.12. Potential backgrounds arising from new physics, such as *e.g.* SUSY or graviton production, are not considered in this analysis[1]. New physics backgrounds are expected to be small at the LHC compared to Standard Model QCD processes and may at least to good approximation be neglected.

[1] To verify that SUSY processes form a negligible contribution to the background, a sample of SUSY processes was generated with `PYTHIA` and passed through the event selection.

Process	MSUB	$\hat{p}_T^{min}$ (GeV)	σ (fb)	N_{gen}	Scale factor
Hard QCD	11,12,13,28,53,68	280.0	1.29×10^7	1.4×10^8	0.917
$t\bar{t}$	81,82	10.0	4.88×10^5	5×10^6	0.973
$W^{\pm}W^{\mp}$	25	240.0	468	10^6	0.257
$W^{\pm}Z^0$	23	10.0	2.57×10^4	10^6	0.105
Z^0Z^0	22	10.0	1.05×10^4	3×10^6	0.705
$\gamma\gamma$	18,114	10.0	2.12×10^5	3×10^6	0.929
$\gamma W^{\pm}, \gamma\gamma^*, \gamma Z^0$	19,20	10.0	277×10^50	10^6	0.736
$W^{\pm}q$	16,31	240.0	7.37×10^4	10^6	0.315
Z^0q, γ^*q	15,30	240.0	3.16×10^4	10^6	0.235
γq	14,29,115	240.0	2.36×10^4	10^6	0.235
$b\bar{b}$	81,82	240.0	8.65×10^4	10^6	0.862

Table 4.12: Background samples and cross sections. MSUB refers to the PYTHIA subprocesses. To restrict the simulation to $t\bar{t}$ and $b\bar{b}$ events, subprocesses 81 and 82 were run with the parameter setting MSEL=6 and MSEL=5 for $t\bar{t}$ and $b\bar{b}$, respectively.

It should be noted that transplanckian black hole production is a non-perturbative process which is expected to suppress perturbative physics. In the transplanckian energy regime, SM backgrounds are therefore expected to be smaller than indicated in Table 4.12. However, no suppression factors are employed in this analysis.

4.3.2 Event Selection and Mass reconstruction

In order to perform studies on black holes produced at the LHC, it is crucial to efficiently separate potential black hole events from background processes. This is achieved by identifying kinematic properties and experimental observables unique to black hole events and applying these to filter away unwanted background. Once this is done, the mass of the black hole is easily reconstructed by summing up the four-momenta of all particles passing the selection filter.

The experimental signatures of black hole events are discussed in Sections 1.3.4 and 4.2. These form the basis for determining the relevant cuts to apply

in the selection of black hole events and rejection of background. To enable comparison, this analysis makes use of the same selection cuts employed in (1). These selection criteria are described below.

1. *Criteria 1:* ***ISR***
   As discussed in Section 3.1, the incoming partons will normally radiate gluons or photons before colliding. Such emissions are labeled *Initial State Radiation* (ISR) and do not partake in the hard scattering interaction. Particles arising from ISR and from the proton fragments of the hard scattering will "pollute" the black hole signal and lead to an overestimation of the black hole mass if included in the reconstruction (1). Accurate reconstruction therefore requires the removal of these particles. Since ISR particles typically have small p_T and large $|\eta|$ (1), their removal is achieved by applying the following requirements to all *particles* in a given event:

   - $p_T > 30$ GeV for $e^{\pm}$ and μ
   - $p_T > 50$ GeV for γ and $jets$
   - $|\eta| < 2.5$

2. *Criteria 2:* ***Multiplicity and Energy***
   Black hole events are characterized by high multiplicities and high Σp_T. Therefore, from particles passing the ISR-cut, at least four particles (≥ 4) are required to have an energy in excess of 300 GeV ($E > 300$ GeV). These requirements serve to select events with many highly energetic jets, leptons and photons. To further suppress SM backgrounds, an additional requirement is imposed whereby at least one of the four energetic particle with E > 300 GeV must be either an electron(/positron) or a photon. Inclusive electron and photon final states have low backgrounds at high $\sqrt{\hat{s}}$ (33). The largest contributions come from the γq processes listed in Table 4.12. Although Table 4.9 indicates that electrons and photons account for only $\sim 5\%$ of the final state particles, the large black hole production cross sections listed in Table 4.11 suggest that events short of final state electrons and photons can readily be sacrificed in return for a more precise

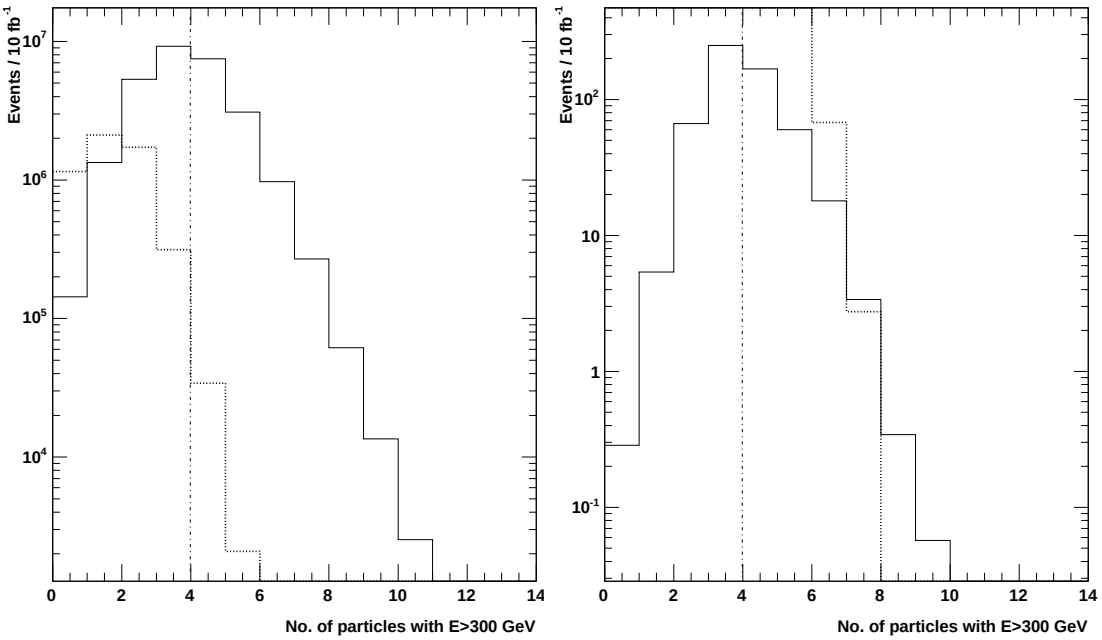

Figure 4.22: Number of energetic particles with E>300 GeV for $(M_P, n) = (1, 3)$ (left) and (5,3) (right) with 10 fb^{-1} of integrated luminosity. Black hole events are shown with solid lines and background distributions with dashed lines. (The background distribution is the same in both plots.) The vertical line marks the cut on energetic particles.

black hole mass reconstruction[1]. This is particularly true for mass points with $M_P = 1$TeV.

Figure 4.22 shows the number of energetic particles (E >300 GeV) for signal and background at mass points (1,3) and (5,3) for 10 fb^{-1} of integrated luminosity. The cut is seen to be very effective and removes a significant fraction of the background. The requirement that the multiplicity of energetic particles exceed three also serves to exclude events were the remnant decay is very dominant.

3. *Criteria 3:* ***Event shape***

[1]It is of course possible to also use muons. However, the muon resolution deteriorates fast with increasing muon momenta and muons are therefore less ideal.

Since black hole events are expected to have fairly spherical event topologies, low sphericity backgrounds are excluded from the event selection by introducing a cut on the event shape variable R_2, as defined in Equation 4.3. As discussed in Section 4.2.2, the event shape variable R_2 will range from 0 to 1 and tend to zero ($R_2 \to 0$) for highly spherical event topologies. Figure 4.18 shows the R_2 distributions for signal and hard QCD background before any cuts are applied. The requirement $R_2 < 0.8$ is seen to remove "back-to-back" backgrounds from hard QCD events and black hole events with dominant remnant decays.

R_2-distributions of signal and background after the application of cuts 1-3 are shown in Figure 4.23.

Mass points with M_P =1 TeV are associated with large black hole production cross sections and the background R_2 distribution is seen to vanish under the large signal. The requirement $R_2 < 0.8$ will serve to remove more signal events, than background. Even so, black hole events with $R_2 > 0.8$ typically have low multiplicities and dominant remnant decays, as indicated in Figure 4.17. To stay within the limits of the semi-classical approximation, the cut is retained also for low M_P topologies. For higher values of M_P the cross section is smaller and the signal is to a larger degree swamped in background. Requiring R_2 <0.8 will serve to remove highly non-spherical background events, leaving the majority of the signal still submerged in the remaining background.

4. *Criteria 4:* ***Missing transverse momenta***
   Since black holes are believed to Hawking radiate mainly to SM particles on the brane, the visible decay products should allow for an adequate reconstruction of the black hole mass. The average fraction of the total energy carried away by neutrinos is $\sim 5\%$[1]. The graviton emission probability is similarly small, and will therefore not contribute greatly to the black hole p_T^{miss}-distribution (33). As discussed in Section 4.2.3, it is of course possible

[1]See Table 4.2 for theoretical particle emissivities.

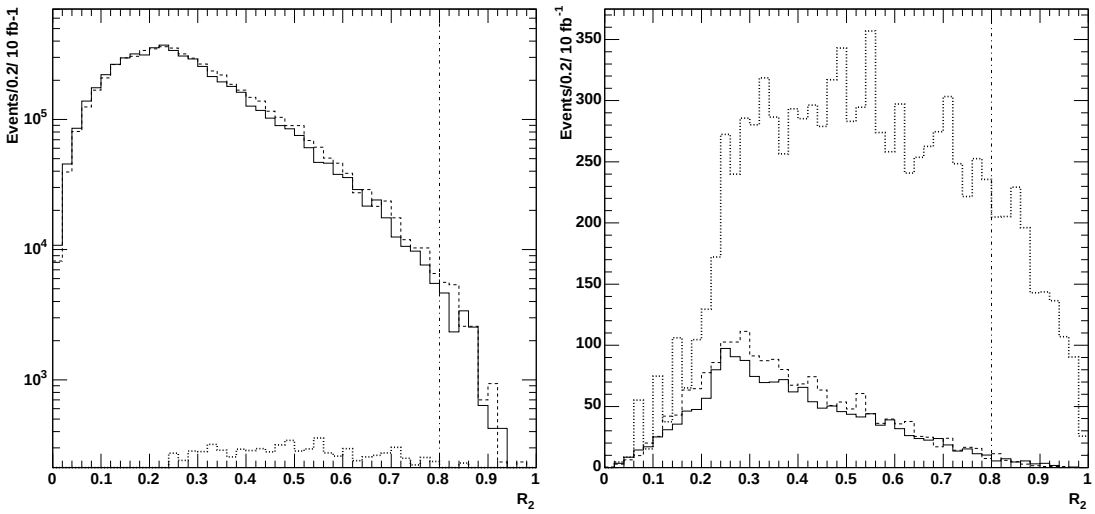

Figure 4.23: R_2-distributions after selection criteria 1-2. Left: (M_P, n) =(1,3)(solid) and (1,7)(dashed) with background (dotted). Right: (M_P, n) =(4,3)(solid) and (4,7)(dashed) with background (dotted). Vertical lines mark the cut $R_2 < 0.8$.

that occasional black hole events may be characterised by missing energies several TeV large. However, the large majority of events will have low missing transverse momentum.

Therefore, in order to obtain an accurate reconstruction of the black hole mass, only events with $p_T^{miss} < 100\text{GeV}$ were selected[1].

5. *Criteria 5:* ***Invariant mass reconstruction*** ***($M_{BH}^{rec} \geq M_P$)***

The black hole four-momentum is reconstructed simply by summing over the four-momenta of all particles passing the above selection criteria 1 through 4:

$$p_{BH} = \sum_r p_r \tag{4.7}$$

[1]The authors of (1) have studied the impact of E_T^{miss} on the reconstructed black hole mass and found that neutrino dominant decays lead to an underestimation of the black hole mass.

where n = electrons, muons, photons and jets. The mass of the black hole is then reconstructed using

$$M_{BH}^{rec} = \sqrt{p_{BH}^2} \tag{4.8}$$

Even though this analysis stretches the theory beyond its valid regime ($M_{BH} \gg M_P$) allowing for the production of semi-classical black holes with masses down to the fundamental Planck mass ($M_{BH}^{gen} \geq M_P$), a reconstructed mass smaller than the fundamental Planck mass ($M_{BH}^{rec} < M_P$) would be unphysical. A lower cut-off on the reconstructed black hole mass is therefore required at $M_{BH}^{rec} = M_P$. However, since M_P is an unknown parameter, the ATLAS sensitivity is evaluated at five different cut-offs (M_{BH}^{cut}) for each reconstructed black hole event:

$$M_{BH}^{rec} \geq M_{BH}^{cut} = \{1, 2, 3, 4, 5\}(\text{TeV}) \tag{4.9}$$

Figure 4.24 shows the reconstructed mass distributions with $M_{BH}^{cut} = 1$ TeV for various values of M_P and fixed $n = 5$ after the application of all the aforementioned selection cuts and an integrated luminosity of 10 fb^{-1}. The figure is indicative of all values of n. For M_P =1 TeV, the signal is seen as a several order of magnitude excess over the background. Even with a limited understanding of the background, a signal should be clearly visible. This is true also for M_P =3 TeV, although the effect is less dramatic. For $M_P \gtrsim 5$ TeV, the signal may be harder to disentangle at 10 *fbi* without are proper understanding of the SM background at high energies. One should also recall that SM processes are expected to be suppressed in the transplanckian energy regime. It is therefore difficult to make accurate predictions from the distributions shown in Figure 4.24.

4.3.2.1 Quality of the reconstruction

Disregarding the background, the quality of the reconstructed black hole invariant mass was found to be determined largely by ISR effects and the p_T^{miss} of the event. Although the particles arising from ISR emissions are removed by *Criteria 1* as described in Section 4.3.2, some gluon emissions are very energetic and give rise

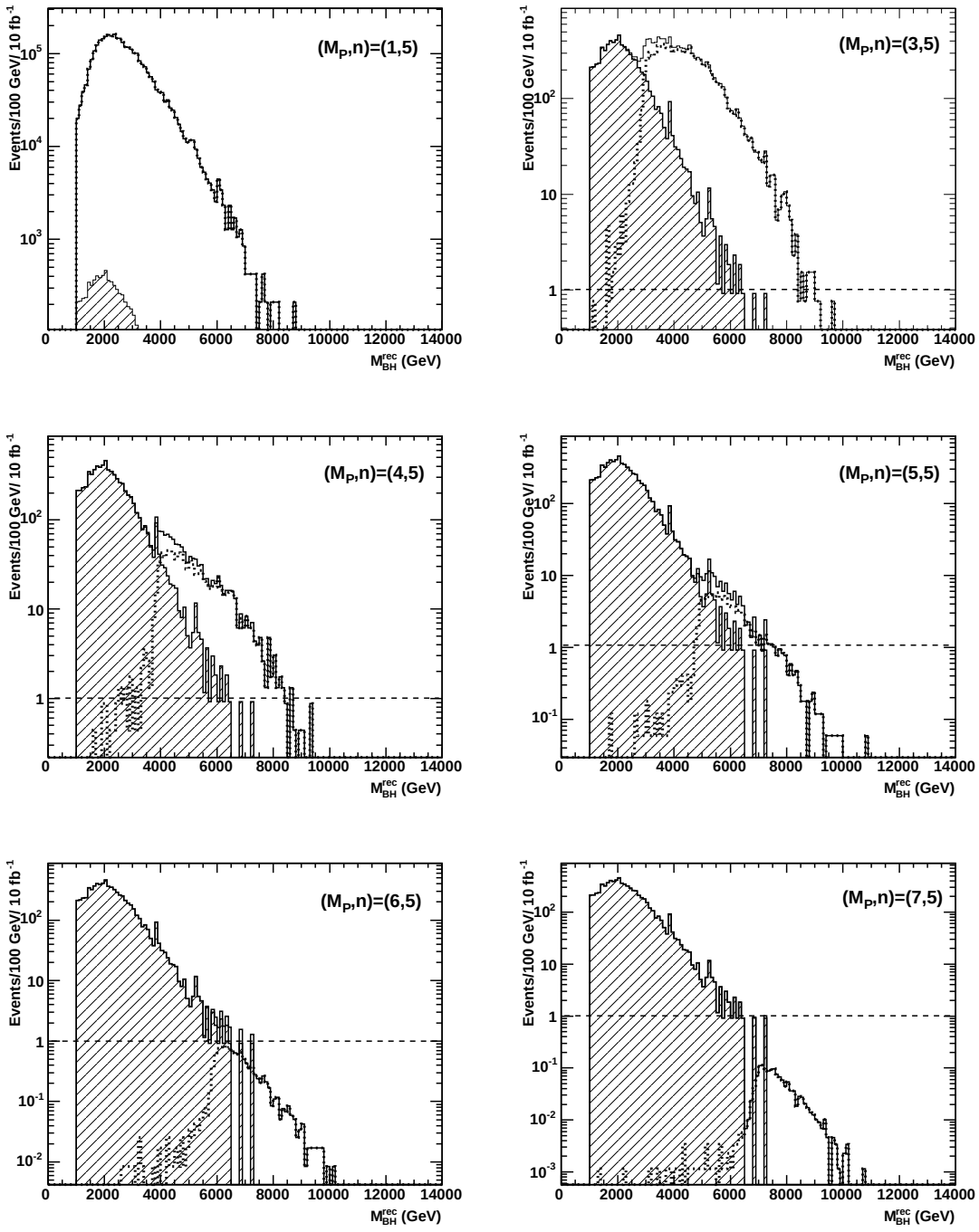

Figure 4.24: Reconstructed black hole mass distributions with $M_{BH}^{cut} = 1$ TeV for mass points $(M_P, n) = \{1, 3, 4, 5, 6, 7\} \times \{5\}$ at an integrated luminosity of 10 fb^{-1}. *Solid*: sum of signal and background; *shaded*: background only; *dotted*: signal only.

to high p_T jets ($\sim$ 100 GeV) which pass the event selection. Such high energy ISR emissions therefore lead to an overestimation of the reconstructed invariant mass. Figure 4.25 shows scatter plots of the reconstructed black hole mass versus the generated black hole mass for mass points (M_P, n) = (1,2) (left) and (5,2) (right). The diagonal lines mark the points $M_{BH}^{rec} = M_{BH}^{gen}$. The horisontal lines show the proper cut-off M_{BH}^{cut} on the reconstructed mass, however this cut-off is omitted in all of these scatter plots. The top plots show that for $M_P = 1$ TeV, the reconstructed mass is sometimes overestimated by as much as ~ 1 TeV. The overestimation is typically smaller for higher values of M_P because ISR emissions then account for a smaller fraction of the total energy of the event. The center plots show the same distributions with ISR effects switched off. ISR effects are seen to account for the overestimation of the black hole mass. Points below the diagonal signify reconstructed black hole events with neutrino dominant decays. Such events typically lead to an underestimation of the black hole mass. In the top (and center) plots, the black hole mass is reconstructed with the requirement $p_T^{miss} < 100$ GeV. The bottom two plots show the same mass points with no requirements on the missing transverse momentum. A softer cut on the p_T^{miss} of the event will contribute to an underestimation of the black hole mass. The underestimation is more marked for $M_P = 5$ TeV, because a larger fraction of events at these points have large missing transverse momentum, as indicated in the p_T^{miss} distributions in Figure 4.20.

4.3.3 Sensitivity

The sensitivity provides a measure of the ATLAS detector's potential to discover black hole events at the LHC. The conditions for conclusive discovery are usually taken as

$$\frac{S}{\sqrt{B}} \geq 5.0 \quad \text{and} \quad S \geq 10 \tag{4.10}$$

where S and B are the number of signal and background events passing the selection criteria, respectively. In other words, discovery is declared only when the number of signal events exceeds the error in the number of background events by no less than a factor five. The numbers S and B required to achieve $\frac{S}{\sqrt{B}} = 5$

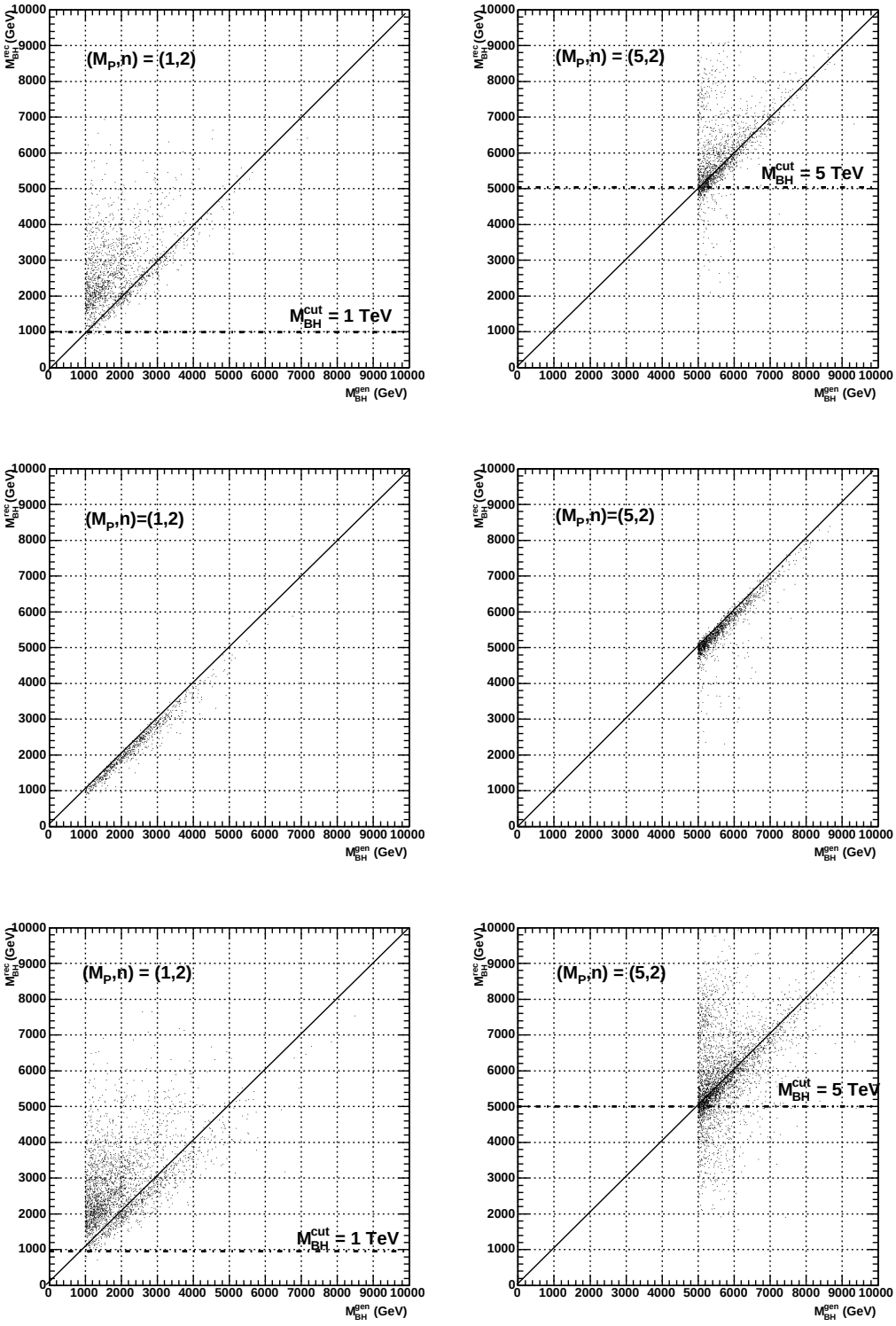

Figure 4.25: Reconstructed black hole mass (M_{BH}^{rec}) vs. generated black hole mass (M_{BH}^{gen}) for mass points (M_P, n) =(1,2) and (5,2). See text for detail.

may be translated into a specific luminosity required for discovery. The discovery luminosity in turn provides an estimate for the time of LHC running required before a 5σ discovery of black holes can be declared.

The discovery luminosity is here determined with a simple counting experiment, along the lines of (1). (The feasibility of such an experiment is discussed in Section 4.5.5). The procedure is straighforward and may be summarised in four steps:

1. Signal and background samples are both normalised to an integrated luminosity of 10 fb^{-1}, and passed through the event selection described in Section 4.3.2.

2. The number of signal and background events passing all the selection criteria are counted separately and the efficiencies of the selection cuts evaluated.

3. The values obtained are used to compute the *significance* $\frac{S}{\sqrt{B}}$.

4. Finally the integrated discovery luminosity $\int \mathcal{L}_D \, dt$ is evaluated.

The above steps are repeated across all points of the parameter space

$$(M_P, n) = \{1, 3, 4, 5\} \times \{2, 3, 5, 7\}. \tag{4.11}$$

The procedure is detailed below along with all results obtained.

4.3.3.1 Number of Signal (S) and Background (B) events

To determine the background associated with each lower cut-off $M_{BH}^{cut} = \{1, 2, 3, 4, 5\}$ (TeV), the number of background events passing all the selection criteria were simply counted. Table 4.13 presents the number of background events retained after the application of selection cuts for each lower cut-off M_{BH}^{cut}. The efficiencies

$$\varepsilon^{M_{BH}^{cut}} = \frac{\text{events reconstructed}}{\text{events in generated}} \tag{4.12}$$

give the fraction of the total number of events at 10 fb^{-1} that successfully pass all selection criteria.

For lower values of M_{BH}^{cut} the efficiencies are found to be $\sim 10^{-5}$ corresponding to a total number of background events in the order of 10^3. For $M_{BH}^{cut} \leq 3$ TeV the total number of background events is found to be larger than the values quoted in (1), by a factor $\sim 2.5 - 3$. As expected, the background from direct photon production (γq) is seen to have higher efficiencies ($\sim 10^{-3} - 10^{-4}$) than the other processes, however the cross section for γq processes is roughly five hundred times smaller than that of the more dominant hard QCD. For $M_{BH}^{cut} >$ 3 TeV the efficiencies are seen to vanish for most background processes and the total number of background events is of the order 10^1-10^2 and factor 2-3 times larger than the values quoted in (1).

The number of signal events passing the selection criteria were evaluated in a similar manner at each mass point $(M_P, n) = \{1, 3, 4, 5, 6, 7\} \times \{2, 3, 5, 7\}$ and the corresponding efficiencies were computed at each value of the lower cut-off M_{BH}^{cut}. The results are listed in Tables 4.14 and C.3.

At most mass points signal events are found to have efficiencies of roughly $10^{-2}(\sim 1\%)$ for all values of M_{BH}^{cut}. For mass points with $M_P = 1$ TeV, efficiencies are found to be somewhat lower ($\sim 10^{-3} - 10^{-4}$) for $M_{BH}^{cut} \geq 3$ TeV. This is to be expected as most of the events generated at these mass points will result in black hole masses around $\sim$1 TeV. Black hole events generated with a lower production threshold $M_{BH}^{min} = 1$ TeV are therefore more likely to be rejected by higher cut-offs on the reconstructed invariant mass.

4.3.3.2 Significance and integrated discovery luminosity

The significance $\frac{S}{\sqrt{B}}$ of signals at each mass point $(M_P, n) = \{1, 3, 5, 6, 7\} \times \{2, 3, 5, 7\}$ is straightforwardly computed using the values listed in Table 4.13 and Tables 4.14 and C.3. The results are listed in Table C.4 and C.5.

It is seen that mass points with high cross sections (M_P =1 TeV) enjoy large signal to background ratios, on the order $\sim 10^4$. The significance decreases with the black hole cross section, but is also seen to peak when $M_{BH}^{cut} = M_P + 1$ TeV. This may be due to the black hole invariant mass distributions typically peaking at values slightly above M_P, while the background falls off exponentially as indicated in Figure 4.24. For all mass points with M_P <6 TeV, $\frac{S}{\sqrt{B}} \gg 5$ at

Background	qq		$t\bar{t}$		$W^{\pm}W^{\mp}$	
σ (fb)	1.28×10^7		4.88×10^5		467	
M_{BH}^{cut} (TeV)	B	$\varepsilon^{M_{BH}^{cut}}$	B	$\varepsilon^{M_{BH}^{cut}}$	B	$\varepsilon^{M_{BH}^{cut}}$
1.0	7.16×10^3	5.553×10^{-5}	85.6	1.8×10^{-5}	0.188	4×10^{-5}
2.0	4.10×10^3	3.182×10^{-5}	19.5	4.0×10^{-6}	0.094	2×10^{-5}
3.0	1.11×10^3	8.586×10^{-6}	2.92	6×10^{-7}	0.047	1×10^{-5}
4.0	248	1.92×10^{-6}	0	0	0	0
5.0	52.5	4.1×10^{-7}	0	0	0	0
Background	$W^{\pm}Z^0$		Z^0Z^0		$\gamma\gamma$	
σ (fb)	2.57×10^4		1.05×10^4		2.12×10^5	
M_{BH}^{cut} (TeV)	B	$\varepsilon^{M_{BH}^{cut}}$	B	$\varepsilon^{M_{BH}^{cut}}$	B	$\varepsilon^{M_{BH}^{cut}}$
1.0	0	0	0.210	2×10^{-6}	0	0
2.0	0	0	0.210	2×10^{-6}	0	0
3.0	0	0	0	0	0	0
4.0	0	0	0	0	0	0
5.0	0	0	0	0	0	0
Background	$\gamma W^{\pm}, \gamma\gamma^*, \gamma Z^0$		$W^{\pm}q$		Zq, γ^*q	
σ (fb)	2.77×10^5		7.37×10^4		3.16×10^4	
M_{BH}^{cut} (TeV)	B	$\varepsilon^{M_{BH}^{cut}}$	B	$\varepsilon^{M_{BH}^{cut}}$	B	$\varepsilon^{M_{BH}^{cut}}$
1.0	0.929	3×10^{-7}	36.1	4.9×10^{-5}	19.0	6×10^{-5}
2.0	0	0	18.4	2.5×10^{-5}	6.31	2×10^{-5}
3.0	0	0	4.42	6×10^{-6}	3.16	1×10^{-5}
4.0	0	0	0.736	1×10^{-6}	3.16	1×10^{-5}
5.0	0	0	0	0	3.16	1×10^{-5}
Background	γq		$b\bar{b}$		TOTAL	
σ (fb)	2.36×10^4		8.65×10^4			
M_{BH}^{cut} (TeV)	B	$\varepsilon^{M_{BH}^{cut}}$	B	$\varepsilon^{M_{BH}^{cut}}$	B	
1.0	389	1.656×10^{-3}	13.8	1.6×10^{-5}	7.70×10^3	
2.0	220	9.34×10^{-4}	6.04	7×10^{-6}	4.37×10^3	
3.0	56.9	2.42×10^{-4}	0	0	1.13×10^3	
4.0	11.5	4.9×10^{-5}	0	0	263	
5.0	1.18	5×10^{-6}	0	0	56.8	

Table 4.13: Number of background events (B) passing all selection criteria. Selection efficiencies $\varepsilon^{M_{BH}^{cut}}$ are quoted for each lower cut-off M_{BH}^{cut}. The numbers correspond to an integrated luminosity of 10 fb^{-1}.

(M_P, n)	(1,2)		(1,3)		(1,5)		(1,7)	
σ (fb)	2.41×10^7		2.11×10^7		2.12×10^7		2.24×10^7	
M_{BH}^{cut} (TeV)	S	$\varepsilon^{M_{BH}^{cut}}$	S	$\varepsilon^{M_{BH}^{cut}}$	S	$\varepsilon^{M_{BH}^{cut}}$	S	$\varepsilon^{M_{BH}^{cut}}$
1.0	5.084×10^6	2.112×10^{-2}	4.116×10^6	1.9692×10^{-2}	3.971×10^6	1.8703×10^{-2}	4.312×10^6	1.8449×10^{-2}
2.0	3.860×10^6	1.604×10^{-2}	3.114×10^6	1.4864×10^{-2}	2.942×10^6	1.3857×10^{-2}	3.165×10^6	1.3543×10^{-2}
3.0	1.583×10^6	6.57×10^{-3}	1.315×10^6	6.218×10^{-3}	1.214×10^6	5.716×10^{-3}	1.304×10^6	4.579×10^{-3}
4.0	5.158×10^5	2.143×10^{-3}	4.205×10^5	1.988×10^{-3}	3.843×10^5	1.810×10^{-3}	4.106×10^5	1.757×10^{-3}
5.0	1.461×10^5	6.07×10^{-4}	1.115×10^5	5.27×10^{-4}	1.062×10^5	5.00×10^{-4}	1.094×10^5	3.68×10^{-4}
(M_P, n)	(3,2)		(3,3)		(3,5)		(3,7)	
σ (fb)	4.11×10^4		3.70×10^4		3.81×10^4		4.24×10^4	
M_{BH}^{cut} (TeV)	S	$\varepsilon^{M_{BH}^{cut}}$	S	$\varepsilon^{M_{BH}^{cut}}$	S	$\varepsilon^{M_{BH}^{cut}}$	S	$\varepsilon^{M_{BH}^{cut}}$
1.0	1.300×10^4	1.5843×10^{-2}	1.1289×10^4	1.5251×10^{-2}	1.153×10^4	1.5005×10^{-2}	1.286×10^4	1.5155×10^{-2}
2.0	1.299×10^4	1.5826×10^{-2}	1.1275×10^4	1.5232×10^{-2}	1.151×10^4	1.4984×10^{-2}	1.285×10^4	1.5141×10^{-2}
3.0	1.242×10^4	1.5132×10^{-2}	1.074×10^4	1.4505×10^{-2}	1.100×10^4	1.4325×10^{-2}	1.221×10^4	1.439×10^{-2}
4.0	7699	9.382×10^{-3}	6608	8.927×10^{-3}	6728	8.759×10^{-3}	7396	8.717×10^{-3}
5.0	3245	3.955×10^{-3}	2793	3.773×10^{-3}	2844	3.703×10^{-3}	3142	3.703×10^{-3}
(M_P, n)	(4,2)		(4,3)		(4,5)		(4,7)	
σ (fb)	4648		4233		4376		4883	
M_{BH}^{cut} (TeV)	S	$\varepsilon^{M_{BH}^{cut}}$	S	$\varepsilon^{M_{BH}^{cut}}$	S	$\varepsilon^{M_{BH}^{cut}}$	S	$\varepsilon^{M_{BH}^{cut}}$
1.0	922.2	1.984×10^{-2}	853.8	2.017×10^{-2}	910.6	2.081×10^{-2}	997.6	2.043×10^{-2}
2.0	921.7	1.983×10^{-2}	853.8	2.017×10^{-2}	908.9	2.077×10^{-2}	996.6	2.041×10^{-2}
3.0	918.0	1.975×10^{-2}	847.0	2.000×10^{-2}	901.5	2.060×10^{-2}	993.2	2.041×10^{-2}
4.0	858.5	1.847×10^{-2}	776.8	1.835×10^{-2}	828.4	1.893×10^{-2}	932.2	1.909×10^{-2}
5.0	457.4	9.84×10^{-3}	402.6	9.51×10^{-3}	424.9	9.71×10^{-3}	481.0	9.85×10^{-3}

Table 4.14: Number of signal events (S) passing all selection criteria for each mass point $(M_P, n) = \{1, 3, 4\} \times \{2, 3, 5, 7\}$.Selection efficiencies $\varepsilon^{M_{BH}^{cut}}$ are quoted for each lower cut-off M_{BH}^{cut}. Numbers correspond to 10 fb^{-1} of integrated luminosity.

(M_P, n)	(5,2)		(5,3)		(5,5)		(5,7)	
σ (fb)	625		572		594		671	
M_{BH}^{cut} (TeV)	S	$\varepsilon^{M_{BH}^{cut}}$	S	$\varepsilon^{M_{BH}^{cut}}$	S	$\varepsilon^{M_{BH}^{cut}}$	S	$\varepsilon^{M_{BH}^{cut}}$
1.0	107.3	1.718×10^{-2}	95.15	1.665×10^{-2}	102.5	1.725×10^{-2}	121.3	1.809×10^{-2}
2.0	107.3	1.218×10^{-2}	94.98	1.662×10^{-2}	102.4	1.723×10^{-2}	121.3	1.809×10^{-2}
3.0	106.6	1.706×10^{-2}	94.47	1.653×10^{-2}	101.9	1.715×10^{-2}	120.8	1.801×10^{-2}
4.0	105.5	1.689×10^{-2}	95.64	1.531×10^{-2}	101.0	1.699×10^{-2}	119.2	1.777×10^{-3}
5.0	95.64	1.531×10^{-2}	85.84	1.502×10^{-2}	90.38	1.521×10^{-2}	108.1	1.612×10^{-2}
(M_P, n)	(6,2)		(6,3)		(6,5)		(6,7)	
σ (fb)	88.1		81.1		84.7		95.0	
M_{BH}^{cut} (TeV)	S	$\varepsilon^{M_{BH}^{cut}}$	S	$\varepsilon^{M_{BH}^{cut}}$	S	$\varepsilon^{M_{BH}^{cut}}$	S	$\varepsilon^{M_{BH}^{cut}}$
1.0	13.03	1.479×10^{-2}	11.54	1.424×10^{-2}	12.35	1.457×10^{-2}	14.63	1.541×10^{-2}
2.0	13.02	1.478×10^{-2}	11.54	1.424×10^{-2}	12.35	1.457×10^{-2}	14.63	1.541×10^{-2}
3.0	13.00	1.475×10^{-2}	11.50	1.419×10^{-2}	12.31	1.453×10^{-2}	14.57	1.534×10^{-2}
4.0	12.93	1.467×10^{-2}	11.43	1.410×10^{-2}	12.25	1.446×10^{-2}	14.52	1.529×10^{-2}
5.0	12.71	1.442×10^{-2}	11.29	1.393×10^{-2}	12.13	1.431×10^{-2}	14.34	1.510×10^{-3}
(M_P, n)	(7,2)		(7,3)		(7,5)		(7,7)	
σ (fb)	11.8		10.9		11.4		12.8	
M_{BH}^{cut} (TeV)	S	$\varepsilon^{M_{BH}^{cut}}$	S	$\varepsilon^{M_{BH}^{cut}}$	S	$\varepsilon^{M_{BH}^{cut}}$	S	$\varepsilon^{M_{BH}^{cut}}$
1.0	1.487	1.256×10^{-2}	1.345	1.232×10^{-2}	1.572	1.224×10^{-2}	1.640	1.277×10^{-2}
2.0	1.487	1.256×10^{-2}	1.345	1.232×10^{-2}	1.572	1.224×10^{-2}	1.640	1.277×10^{-2}
3.0	1.485	1.254×10^{-2}	1.343	1.230×10^{-2}	1.572	1.224×10^{-2}	1.640	1.277×10^{-2}
4.0	1.480	1.250×10^{-2}	1.332	1.220×10^{-2}	1.563	1.217×10^{-2}	1.638	1.276×10^{-2}
5.0	1.468	1.240×10^{-2}	1.320	1.209×10^{-2}	1.551	1.208×10^{-2}	1.624	1.265×10^{-2}

Table 4.15: Number of signal events (S) passing all selection criteria for each mass point $(M_P, n) = \{5, 6, 7\} \times \{2, 3, 5, 7\}$. Selection efficiencies $\varepsilon^{M_{BH}^{cut}}$ are quoted for each lower cut-off M_{BH}^{cut}. Numbers correspond to 10 fb^{-1} of integrated luminosity.

an integrated luminosity of 10 fb^{-1}, crudely indicating that black hole events are produced in large numbers and should be discernible within a relatively modest time of LHC running.

The discovery luminosity $\int \mathcal{L}_D \, dt$ specifies the luminosity required for discovery. The conventional discovery condition employed in this sensitivity study is given by (4.10). A step-by-step procedure for computing the discovery luminosity is listed below:

- The number of black hole events produced after a given time of LHC running ($N_{BH}(t)$) is proportional to the production cross section and the integrated collider luminosity:

$$N_{BH}(t) = \sigma_{pp\to BH} \times \int \mathcal{L}_{LHC} \, dt \tag{4.13}$$

- Let N_{S_G} (N_{B_G}) and S_G (B_G) be total number of signal (background) events generated and the number of retained signal (background) events after selection cuts, respectively. The efficiencies listed in Tables 4.14 and C.3 are then given by:

$$\varepsilon^{M_{BH}^{cut}} = \frac{S_G}{N_{S_G}} \tag{4.14}$$

  (and similarly for the background efficiencies listed in Table 4.13).

- If $S_{5\sigma} = fS_G$ ($B_{5\sigma} = fB_G$) is the number of signal (background) events after selection cuts required for a 5σ discovery and f is a multiplicative factor, then the number of generated events $N_{5\sigma}$ required for a 5σ discovery can be found as:

$$N_{5\sigma} = \frac{S_{5\sigma}}{\varepsilon^{M_{BH}^{cut}}} = \frac{fS_G}{\varepsilon^{M_{BH}^{cut}}} \tag{4.15}$$

- The number $N_{5\sigma}$ may then be translated into the corresponding beam luminosity given by:

$$\int \mathcal{L}_D \, dt = \frac{N_{5\sigma}}{\sigma_{pp\to BH}} = \frac{1}{\sigma_{pp\to BH}} \frac{fS_G}{\varepsilon^{M_{BH}^{min}}} \tag{4.16}$$

  where $\sigma_{pp\to BH}$ is the cross section of the process in question.

The multiplication factor f is found by way of the conditions for a 5σ discovery, given by Equation (4.10):

$$5 = \frac{S_{5\sigma}}{\sqrt{B_{5\sigma}}} = \frac{fS_G}{\sqrt{fB_G}} = \frac{S_G}{\sqrt{B_G}}\sqrt{f} \quad \Longrightarrow \quad f = \left(\frac{5\sqrt{B_G}}{S_G}\right)^2 \tag{4.17}$$

If $S_{5\sigma}$ comes out less than 10 ($S_{5\sigma}$ <10), the appropriate multiplication factor is given by:

$$S_{5\sigma} = fS_G \geq 10 \Longrightarrow f \geq f_{min} = \frac{10}{S_G} \tag{4.18}$$

Integrated discovery luminosities were evaluated for mass points $(M_P, n) = \{1, 3, 4, 5\} \times \{2, 3, 5, 7\}$ and only in cases where $M_{BH}^{cut} \geq M_P$. The results are listed in Tables C.4 and C.5. Figure 4.26 shows the integrated discovery luminosity as a function of the fundamental Planck mass M_P and the number of extra dimensions n for the two cases $M_{BH}^{cut} = M_P$ and $M_{BH}^{cut} = M_P + 1$ TeV.
The discovery potential is found to depend very weakly on n and very strongly on M_P. This behavior is expected since the black hole production cross section

$$\sigma_{pp\to BH} \approx \pi r_H^2 \sim \frac{1}{M_P^2}\left(\frac{M_{BH}}{M_P}\right)^{\frac{2}{n+1}} \tag{4.19}$$

depends strongly on the value of M_P[1] and less so on the value of n. The authors of (1) have proposed that the strong dependency of $\int \mathcal{L}_D\, dt$ on M_P may be used to determine the value of M_P experimentally by observing how early discovery is achieved.

The results presented in Table C.4 and C.5 are found to be in fair agreement with values quoted in (1). Slightly lower discovery luminosities (factor ~ 0.15) are observed for mass points (M_P, n)=$\{1\} \times \{2, 3, 5, 7\}$ because `CHARYBDIS` provides cross sections roughly twice as large for processes at $M_P = 1$ TeV.

[1] This dependency is especially marked when $\frac{M_{BH}}{M_P} \approx 1$ as is typically the case when the lower threshold for black hole production is set equal to the fundamental Planck mass.

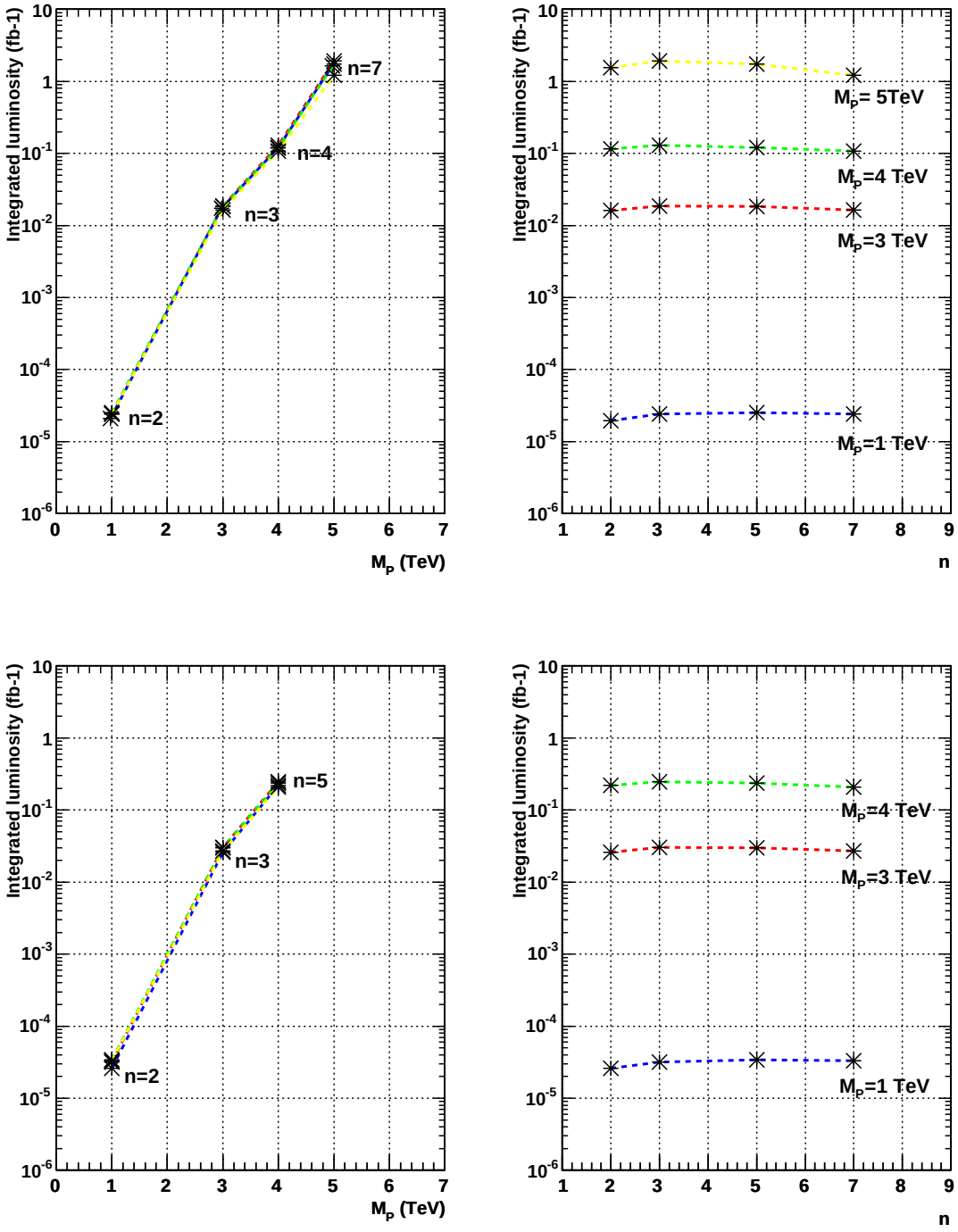

Figure 4.26: The discovery luminosity as a function of M_P and n. The top pair show points evaluated at $M_{BH}^{cut} = M_P$, while the bottom pair show points evaluated at $M_{BH}^{cut} = M_P + 1$ TeV.

(M_P, n)	(1,2)		(1,3)		(1,5)		(1,7)	
σ (fb)	2.41×10^7		2.11×10^7		2.12×10^7		2.24×10^7	
M_{BH}^{cut} (TeV)	$S/\sqrt{B}$	$\int \mathcal{L}_D dt(\text{fb}^{-1})$	$S/\sqrt{B}$	$\int \mathcal{L}_D dt(\text{fb}^{-1})$	$S/\sqrt{B}$	$\int \mathcal{L}_D dt(\text{fb}^{-1})$	$S/\sqrt{B}$	$\int \mathcal{L}_D dt(\text{fb}^{-1})$
1.0	5.79×10^4	1.96×10^{-5}	4.75×10^4	2.41×10^{-5}	4.53×10^4	2.52×10^{-5}	4.91×10^4	2.42×10^{-5}
2.0	5.84×10^4	2.59×10^{-5}	4.76×10^4	3.19×10^{-5}	4.45×10^4	3.40×10^{-5}	4.79×10^4	3.30×10^{-5}
3.0	4.71×10^4	6.32×10^{-5}	3.91×10^4	7.62×10^{-5}	3.61×10^4	8.25×10^{-5}	3.88×10^4	8.00×10^{-5}
4.0	3.18×10^4	1.9×10^{-4}	2.59×10^4	2.4×10^{-4}	2.37×10^4	2.6×10^{-4}	2.53×10^4	2.5×10^{-4}
5.0	1.94×10^4	6.8×10^{-4}	1.48×10^4	9.0×10^{-4}	1.41×10^4	9.42×10^{-4}	1.45×10^4	9.5×10^{-4}
(M_P, n)	(3,2)		(3,3)		(3,5)		(3,7)	
σ (fb)	4.11×10^4		3.70×10^4		3.81×10^4		4.24×10^4	
M_{BH}^{cut} (TeV)	$S/\sqrt{B}$	$\int \mathcal{L}_D dt(\text{fb}^{-1})$	$S/\sqrt{B}$	$\int \mathcal{L}_D dt(\text{fb}^{-1})$	$S/\sqrt{B}$	$\int \mathcal{L}_D dt(\text{fb}^{-1})$	$S/\sqrt{B}$	$\int \mathcal{L}_D dt(\text{fb}^{-1})$
1.0	148		129		131		147	
2.0	197		171		174		185	
3.0	369	1.61×10^{-2}	319	1.86×10^{-2}	327	1.83×10^{-2}	363	1.64×10^{-2}
4.0	475	2.59×10^{-2}	407	3.03×10^{-2}	415	3.00×10^{-2}	456	2.71×10^{-2}
5.0	431	6.15×10^{-2}	371	7.16×10^{-2}	377	7.09×10^{-2}	417	6.37×10^{-2}
(M_P, n)	(4,2)		(4,3)		(4,5)		(4,7)	
σ (fb)	4648		4233		4376		4883	
M_{BH}^{cut} (TeV)	$S/\sqrt{B}$	$\int \mathcal{L}_D dt(\text{fb}^{-1})$	$S/\sqrt{B}$	$\int \mathcal{L}_D dt(\text{fb}^{-1})$	$S/\sqrt{B}$	$\int \mathcal{L}_D dt(\text{fb}^{-1})$	$S/\sqrt{B}$	$\int \mathcal{L}_D dt(\text{fb}^{-1})$
1.0	10.5		9.73		10.4		13.36	
2.0	13.9		12.9		13.7		15.1	
3.0	27.3		25.2		26.8		29.5	
4.0	52.9	0.116	47.9	0.129	51.1	0.121	57.5	0.107
5.0	60.7	0.219	53.4	0.248	56.4	0.235	63.8	0.208

Table 4.16: The significance $\frac{S}{\sqrt{B}}$ at mass points $(M_P, n) = \{1, 3, 4\} \times \{2, 3, 5, 7\}$ with 10 fb^{-1} of integrated luminosity. The discovery luminosity $\int \mathcal{L}_D \, dt$ is evaluated for all points where $M_{BH}^{cut} \geq M_P$ within the restricted parameter space $(M_P, n) = \{1, 3, 4, 5\} \times \{2, 3, 5, 7\}$.

(M_P, n)	(5,2)		(5,3)		(5,5)		(5,7)	
σ (fb)	625		572		594		671	
M_{BH}^{cut} (TeV)	$S/\sqrt{B}$	$\int \mathcal{L}_D dt(\text{fb}^{-1})$	$S/\sqrt{B}$	$\int \mathcal{L}_D dt(\text{fb}^{-1})$	$S/\sqrt{B}$	$\int \mathcal{L}_D dt(\text{fb}^{-1})$	$S/\sqrt{B}$	$\int \mathcal{L}_D dt(\text{fb}^{-1})$
1.0	1.22		1.08		1.17		1.38	
2.0	1.62		1.44		1.55		2.83	
3.0	3.17		3.03		3.00		3.55	
4.0	6.51		5.79		6.22		7.35	
5.0	12.7	1.55	11.4	1.192	12.0	1.74	14.3	1.22
(M_P, n)	(6,2)		(6,3)		(6,5)		(6,7)	
σ (fb)	88.1		81.1		84.7		95.0	
M_{BH}^{cut} (TeV)	$S/\sqrt{B}$	$\int \mathcal{L}_D dt(\text{fb}^{-1})$	$S/\sqrt{B}$	$\int \mathcal{L}_D dt(\text{fb}^{-1})$	$S/\sqrt{B}$	$\int \mathcal{L}_D dt(\text{fb}^{-1})$	$S/\sqrt{B}$	$\int \mathcal{L}_D dt(\text{fb}^{-1})$
1.0	0.148		0.132		0.141		0.167	
2.0	0.197		0.175		0.187		0.221	
3.0	0.387		0.342		0.366		0.433	
4.0	0.797		0.755		0.755		0.895	
5.0	1.69		1.61		1.61		1.90	
(M_P, n)	(7,2)		(7,3)		(7,5)		(7,7)	
σ (fb)	11.8		10.9		11.4		12.8	
M_{BH}^{cut} (TeV)	$S/\sqrt{B}$	$\int \mathcal{L}_D dt(\text{fb}^{-1})$	$S/\sqrt{B}$	$\int \mathcal{L}_D dt(\text{fb}^{-1})$	$S/\sqrt{B}$	$\int \mathcal{L}_D dt(\text{fb}^{-1})$	$S/\sqrt{B}$	$\int \mathcal{L}_D dt(\text{fb}^{-1})$
1.0	1.69×10^{-2}		1.53×10^{-2}		1.79×10^{-2}		1.87×10^{-2}	
2.0	2.25×10^{-2}		2.03×10^{-2}		2.38×10^{-2}		2.48×10^{-2}	
3.0	4.42×10^{-2}		3.40×10^{-2}		4.68×10^{-2}		4.88×10^{-2}	
4.0	9.13×10^{-2}		8.21×10^{-2}		9.64×10^{-2}		0.101	
5.0	0.195		0.175		0.206		0.215	

Table 4.17: The significance $\frac{S}{\sqrt{B}}$ at mass points $(M_P, n) = \{5, 6, 7\} \times \{2, 3, 5, 7\}$ with 10 fb^{-1} of integrated luminosity. The discovery luminosity $\int \mathcal{L}_D \, dt$ is evaluated for all points where $M_{BH}^{cut} \geq M_P$ within the restricted parameter space $(M_P, n) = \{5\} \times \{2, 3, 5, 7\}$.

4.4 The impact of new effects and revised discovery luminosities

The effect of greybody factors and the time variation of the Hawking temperature T_H on the parton level emission spectra of black holes is discussed in Section 4.1.3.5. In this section the sensitivity analysis presented in Section 4.3.3 is repeated with the effects of time variation and greybody factors included to provide an update on the ATLAS sensitivity study presented in (1).

New signal samples were generated across the same parameter space $(M_P, n) = \{1, 3, 4, 5, 6, 7\} \times \{2, 3, 5, 7\}$. The switches `TIMVAR` and `GRYBDY` were both set to `.TRUE.`, all other parameter settings were as given in Table 4.10. The production cross sections for all samples are listed in Table 4.18 and seen to agree with the values listed in Table 4.11 to two significant figures. Table 4.18 also compares `CHARYBDIS` cross sections with the cross section quoted in (1). `CHARYBDIS` is seen to give slightly larger cross sections ($\sim 25\% - 150\%$) for $M_P < 5$TeV and slightly lower cross section ($\sim 5\% - 48\%$) for $M_P > 5$TeV.

The simulated data was normalised to an integrated luminosity of 10 fb^{-1} and the same procedure outlined in Section 4.3.3 was employed to evaluate the impact of a time-evolving Hawking temperature and greybody factors on the ATLAS sensitivity to black holes. This study was performed with slightly lower statistics in signal samples with large cross sections ($M_P \leq 3$ TeV) and in the hard QCD background. The comparison made in this section is done against a different set of signal (and background) samples with new effects switched off, than those presented in Section 4.3.1. The relevant tables which to compare, are given in Appendix C.

4.4.1 Impact of new effects

Deviations from the results presented in Section 4.3.3 are expected to be small, since the discovery luminosity is governed largely by the black hole production cross section and the value of the fundamental Planck mass M_P. However, the event selection uses hard, prompt $e^{\pm}$ and γ for black hole event triggering. The

M_P, n	$\sigma_{Charybdis}$ (fb)	σ_{Atl} (fb)		M_P, n	$\sigma_{Charybdis}$ (fb)	σ_{Atl} (fb)	
1,2	2.40×10^{7}	9.45×10^{6}	2.5	5,2	6.27×10^{2}	6.62×10^{2}	0.9
1,3	2.12×10^{7}	8.26×10^{6}	2.3	5,3	5.72×10^{2}	6.03×10^{2}	0.9
1,5	2.12×10^{7}	8.06×10^{6}	2.6	5,5	5.96×10^{2}	6.25×10^{2}	1.0
1,7	2.34×10^{7}	8.24×10^{6}	2.8	5,7	6.66×10^{2}	6.99×10^{2}	1.0
3,2	4.10×10^{4}	2.55×10^{4}	1.6	6,2	8.81×10^{1}	1.25×10^{2}	0.7
3,3	3.71×10^{4}	2.29×10^{4}	1.6	6,3	8.09×10^{1}	1.14×10^{2}	0.7
3,5	3.82×10^{4}	2.34×10^{4}	1.6	6,5	8.46×10^{1}	1.19×10^{2}	0.7
3,7	4.24×10^{4}	2.60×10^{4}	1.6	6,7	9.52×10^{1}	1.33×10^{2}	0.7
4,2	4.65×10^{3}	3.74×10^{3}	1.2	7,2	1.18×10^{1}	2.29×10^{1}	0.5
4,3	4.26×10^{3}	3.38×10^{3}	1.3	7,3	1.09×10^{1}	2.10×10^{1}	0.5
4,5	4.40×10^{3}	3.49×10^{3}	1.3	7,5	1.14×10^{1}	2.20×10^{1}	0.5
4,7	4.90×10^{3}	3.89×10^{3}	1.3	7,7	1.29×10^{1}	2.47×10^{1}	0.5

Table 4.18: Signal samples and cross sections with the effects of time variation and greybody factors switched on. σ_{Atl} refer to the cross sections quoted in (1). The numbers in the rightmost columns on either side show the ratio $\sigma_{Charybdis}/\sigma_{Atl}$.

black hole discovery potential will therefore be sensitive to the number of black hole final states with energetic electrons and photons.

The effect of both time variation and greybody factors on the parton level energy spectra of emitted particles is discussed in Section 4.1.3.5.

Table 4.2 indicates that the introduction of greybody factors results in a ∼5% increase in the emission probability of charged leptons and a ∼15% decrease in the emission probability of photons.

Figure 4.27 shows the parton level energy spectra of electrons and positrons emitted by black holes generated at mass points $(M_P, n) = (1,3)$ and $(5,3)$ with the new effects switched on and off. The effect of the time variation is to harden the spectrum. The greybody factors however will soften the spectrum, such that the net result is to leave the energy distribution largely unaltered. Even so, an increase in the number of energetic $e^{\pm}$ is observed due to the slight increase in the probability for emission. A 19% increase in the number of electrons emitted

is observed for mass point (1,3), while a 53% increase is seen for (5,3)[1].

Figure 4.28 shows the parton level energy spectra for photons at the same mass points (1,3) and (5,3). In the case of photons, both the time variation and greybody factors serve to harden the energy spectra, thereby increasing the fraction of prompt photons with E>300 GeV. The reduced emission probability however leads to a ∼35% reduction in the number of emitted photons.

Figure 4.29 shows the detector level ratio of the number of energetic electrons and photons with new effects included to the same number of energetic electrons and photons with new effects omitted. In the time-varying, greybody model of the black hole decay, the number of events with at least one energetic (E>300 GeV) electron is increased by $\sim$ 10%. At the same time, a $\sim$ 25% reduction in the number of events with one energetic photon is observed. At mass point (5,3), there is a $\sim$ 35% increase in events with one energetic electron and $\sim$ 20% reduction in events with one energetic photon. All in all, a net decrease in the number of energetic electrons and photons is observed.

4.4.2 Updated discovery luminosities

The event selection criteria were identical to those described in Section 4.3.3. Figure 4.30 shows the number of energetic particles (E>300 GeV) at mass points (M_P, n) =(1,3) and (5,3). The distributions are largely unchanged in face of the new effects, and only a slight attenuation in the multiplicity of energetic signal particles is observed.

The number of signal (S') events passing all the selection criteria are listed in Tables 4.20 and 4.21.

The discovery luminosities with the new data sample, were evaluated as described in Section 4.3.3. Tables 4.22 and 4.23 presents the significance $\frac{S'}{\sqrt{B}}$ at each mass point $(M_P, n) = \{1, 3, 4, 5, 6, 7\} \times \{2, 3, 5, 7\}$ with the updated integrated discovery luminosity $\int \mathcal{L}'_D \, dt$ computed in each case of $M_{BH}^{cut} \geq M_P$.

The new discovery luminosities are presented in Figure 4.31 as a function of M_P and n. The dotted lines show $\int \mathcal{L}'_D \, dt$ with time-evolution and greybody

[1]Even though the theoretical emissivities predict an increase of only ∼5%, the difference between the generated emissivities may very well be much larger as is apparent from Table 4.2.

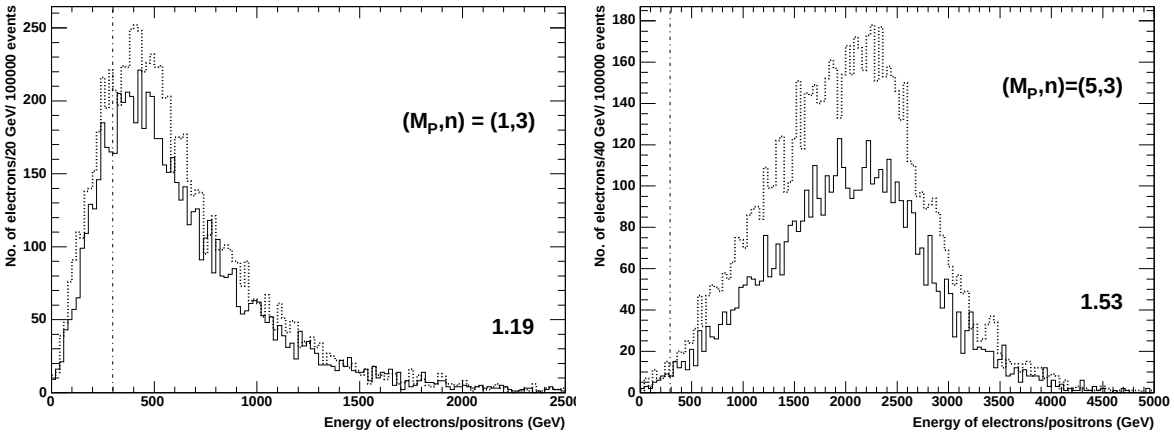

Figure 4.27: Parton level energy spectra of primary $e^{\pm}$ from black holes generated at mass points (M_P, n) =(1,3) (left) and (5,3) (right) with the effects of time variation of T_H and greybody factors included (dotted) and omitted (solid). The numbers in the lower right corners show the ratio of the bin integrals of the dotted and solid histograms. The straight line marks the selection cut at 300 GeV.

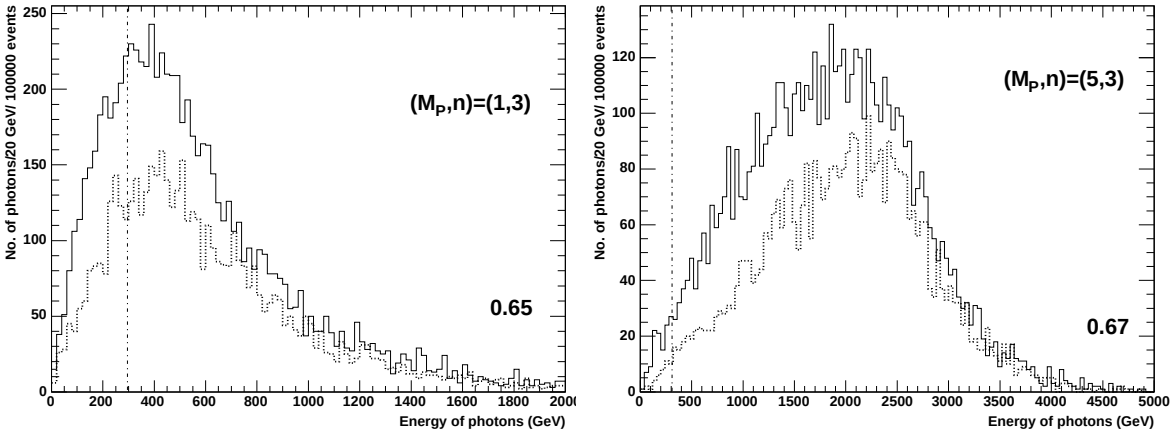

Figure 4.28: Parton level energy spectra of primary γ from black holes generated at mass points (M_P, n) =(1,3) (left) and (5,3) (right) with the effects of time variation of T_H and greybody factors included (dotted) and omitted (solid). The numbers in the lower right corners show the ratio of the bin integrals of the dotted and solid histograms. The straight line marks the selection cut at 300 GeV.

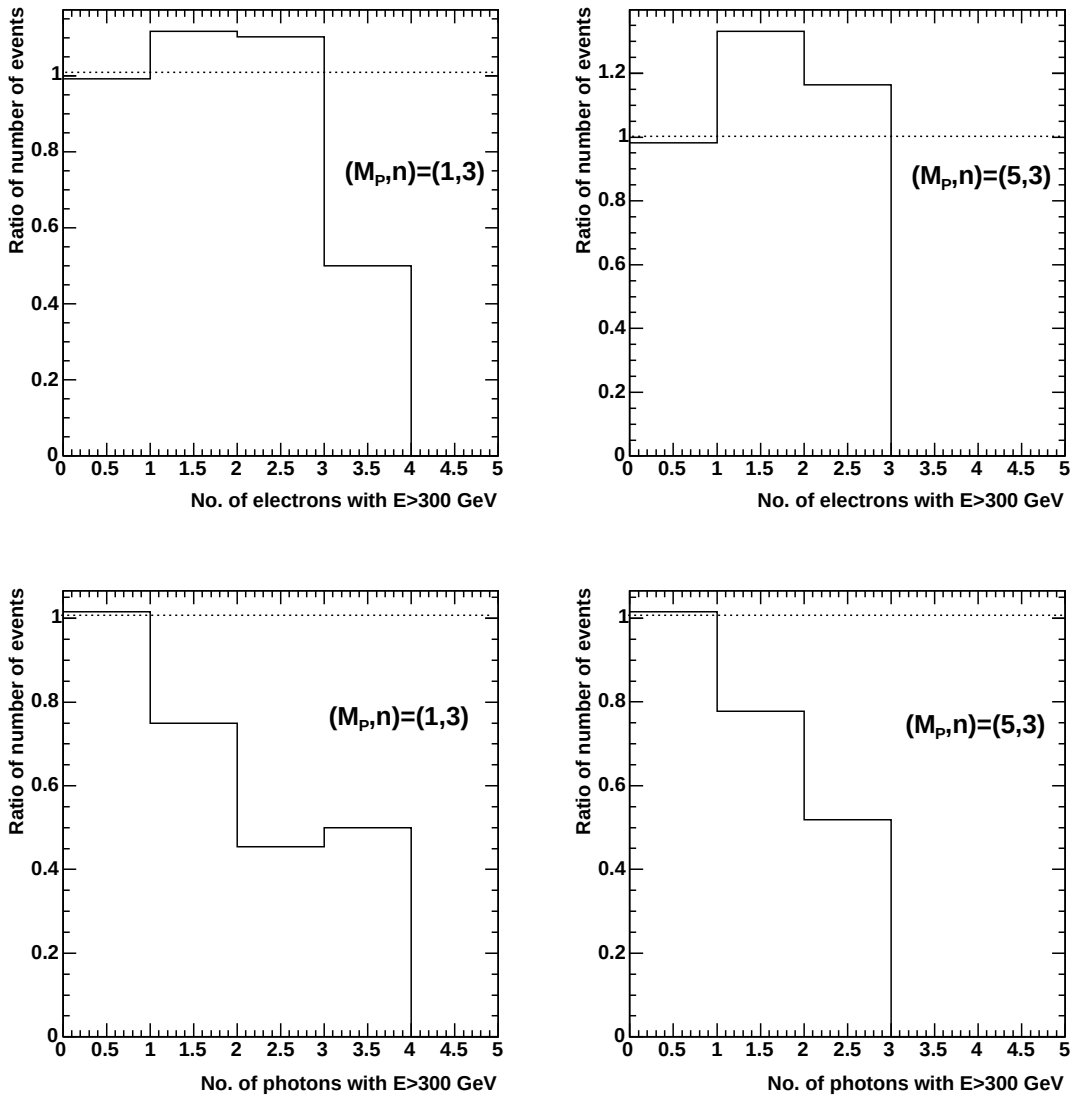

Figure 4.29: Multiplicity distributions of energetic electrons (top) and photons (bottom) with new effects switched on divided by the same distributions with new effects switched off.

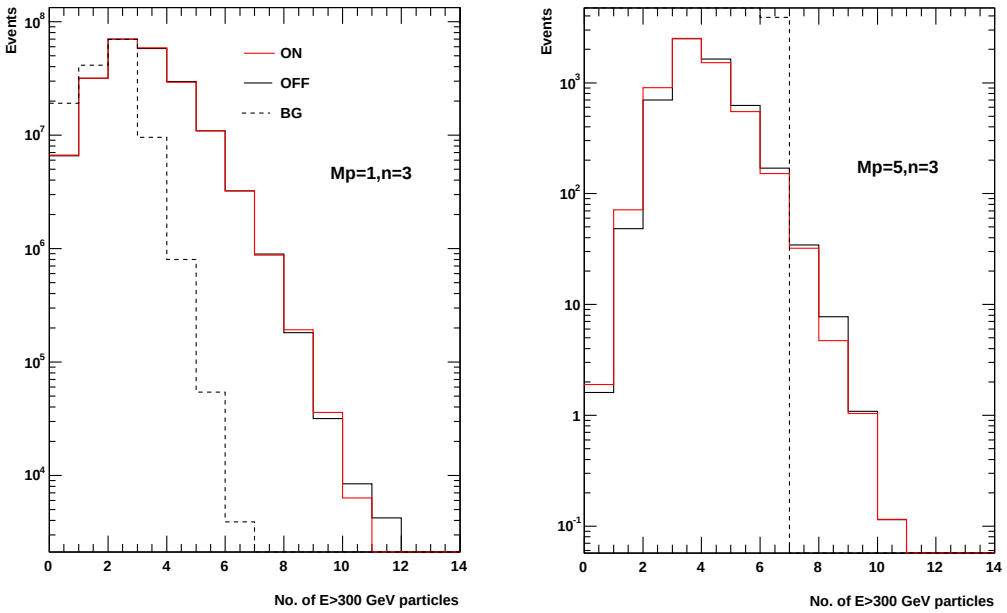

Figure 4.30: Number of energetic particles with E>300 GeV for $(M_P, n) = \{(1,3),(5,3)\}$ with 10 fb^{-1} of data. The solid lines show the signal distribution with the greybody effects and time variation switched on (red) and off (black). The dashed line shows the background distribution.

effects switched on, while the black lines show the values of Tables C.4 and C.5 with new effects switched off.

A slight increase in the discovery luminosity is observed for all mass points (M_P, n) as expected from the net reduction in the number of final states with energetic electrons and photons.

The average ratio $\langle \frac{\int \mathcal{L}_D' \, dt}{\int \mathcal{L}_D \, dt} \rangle$ of the discovery luminosities with new effects included to the corresponding luminosities with new effects omitted, are listed in Table 4.19 for each value of M_P. A time-varying, greybody model of the black hole decay is found to raise the discovery luminosity with respect to a fixed-temperature, blackbody model by $\sim 11\%$ for $M_P = 1$ TeV and $\sim 27\%$ for $M_P \geq 3$ TeV.

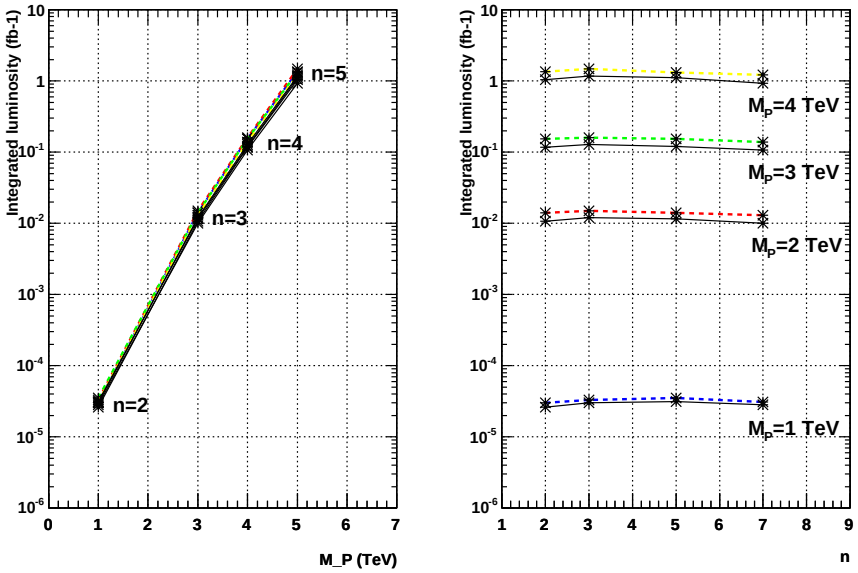

Figure 4.31: Modified discovery luminosities as a function of M_P and n with a varying-temperature, greybody model of the black hole decay. Solid lines show the corresponding luminosities with a fixed-temperature, blackbody model of the black hole decay.

M_P (TeV)	$\langle \frac{\int \mathcal{L}_D^{'} \, dt}{\int \mathcal{L}_{D \; dt} \, dt} \rangle$
1	1.11
3	1.27
4	1.28
5	1.27

Table 4.19: Average ratio of $\int \mathcal{L}_D^{'} \, dt$ to $\int \mathcal{L}_D \, dt$ for various values of M_P.

(M_P, n)	(1,2)		(1,3)		(1,5)		(1,7)	
σ (fb)	2.40×10^7		2.12×10^7		2.12×10^7		2.34×10^7	
M_{BH}^{cut} (TeV)	S'	$\varepsilon^{M_{BH}^{cut}}$	S'	$\varepsilon^{M_{BH}^{cut}}$	S'	$\varepsilon^{M_{BH}^{cut}}$	S'	$\varepsilon^{M_{BH}^{cut}}$
1.0	3.339×10^6	1.390×10^{-2}	3.005×10^6	1.419×10^{-2}	2.830×10^6	1.333×10^{-2}	3.263×10^6	1.397×10^{-2}
2.0	2.616×10^6	1.089×10^{-2}	2.343×10^6	1.106×10^{-2}	2.163×10^6	1.019×10^{-2}	2.518×10^6	1.078×10^{-2}
3.0	1.148×10^6	4.78×10^{-3}	9.87×10^5	4.66×10^{-3}	8.90×10^5	4.19×10^{-3}	1.068×10^6	4.57×10^{-3}
4.0	3.70×10^5	1.54×10^{-3}	2.97×10^5	1.40×10^{-3}	3.38×10^5	1.59×10^{-3}	3.74×10^5	1.60×10^{-3}
5.0	8.2×10^4	3.4×10^{-4}	9.5×10^4	4.5×10^{-4}	1.02×10^5	4.8×10^{-4}	8.6×10^4	3.7×10^{-4}
(M_P, n)	(3,2)		(3,3)		(3,5)		(3,7)	
σ (fb)	4.10×10^4		3.71×10^4		3.82×10^4		4.24×10^4	
M_{BH}^{cut} (TeV)	S'	$\varepsilon^{M_{BH}^{cut}}$	S'	$\varepsilon^{M_{BH}^{cut}}$	S'	$\varepsilon^{M_{BH}^{cut}}$	S'	$\varepsilon^{M_{BH}^{cut}}$
1.0	7420	1.812×10^{-2}	6893	1.860×10^{-2}	7373	1.932×10^{-2}	8179	1.930×10^{-2}
2.0	7412	1.810×10^{-2}	6882	1.857×10^{-2}	7365	1.930×10^{-2}	8171	1.928×10^{-2}
3.0	7076	1.728×10^{-2}	6560	1.770×10^{-2}	7041	1.845×10^{-2}	7815	1.844×10^{-2}
4.0	4681	1.143×10^{-2}	4088	1.103×10^{-2}	4556	1.194×10^{-2}	5103	1.204×10^{-2}
5.0	2007	4.90×10^{-3}	1772	4.78×10^{-3}	2065	5.41×10^{-3}	2310	5.45×10^{-3}
(M_P, n)	(4,2)		(4,3)		(4,5)		(4,7)	
σ (fb)	4654		4257		4395		4897	
M_{BH}^{cut} (TeV)	S'	$\varepsilon^{M_{BH}^{cut}}$	S'	$\varepsilon^{M_{BH}^{cut}}$	S'	$\varepsilon^{M_{BH}^{cut}}$	S'	$\varepsilon^{M_{BH}^{cut}}$
1.0	627.4	1.532×10^{-2}	688.8	1.618×10^{-2}	708.9	1.613×10^{-2}	789.9	1.613×10^{-2}
2.0	627.4	1.532×10^{-2}	688.4	1.617×10^{-2}	708.0	1.611×10^{-2}	788.9	1.611×10^{-2}
3.0	621.6	1.518×10^{-2}	682.8	1.604×10^{-2}	703.2	1.600×10^{-2}	783.5	1.600×10^{-2}
4.0	574.5	1.403×10^{-2}	630.5	1.481×10^{-2}	650.5	1.480×10^{-2}	724.8	1.480×10^{-2}
5.0	299.8	7.32×10^{-3}	335.9	7.89×10^{-3}	357.8	8.14×10^{-3}	398.6	8.14×10^{-3}

Table 4.20: Number of signal events (S') passing all selection criteria for each mass point $(M_P, n) = \{1, 3, 4\} \times \{2, 3, 5, 7\}$. Selection efficiencies $\varepsilon^{M_{BH}^{cut}}$ are quoted for each lower cut-off M_{BH}^{cut}. The data is normalised to an integrated luminosity of $\int \mathcal{L}\, dt$=10 fb^{-1}.

(M_P, n)	(5,2)		(5,3)		(5,5)		(5,7)	
σ (fb)	627		574		596		666	
M_{BH}^{cut} (TeV)	S'	$\varepsilon^{M_{BH}^{cut}}$	S'	$\varepsilon^{M_{BH}^{cut}}$	S'	$\varepsilon^{M_{BH}^{cut}}$	S'	$\varepsilon^{M_{BH}^{cut}}$
1.0	83.82	1.337×10^{-2}	76.63	1.335×10^{-2}	84.53	1.418×10^{-2}	93.12	1.399×10^{-2}
2.0	83.82	1.337×10^{-2}	76.63	1.335×10^{-2}	84.47	1.417×10^{-2}	93.12	1.399×10^{-2}
3.0	83.38	1.330×10^{-2}	76.28	1.329×10^{-2}	84.23	1.413×10^{-2}	92.85	1.395×10^{-2}
4.0	81.81	1.305×10^{-2}	75.13	1.309×10^{-2}	83.10	1.394×10^{-2}	91.72	1.378×10^{-3}
5.0	74.35	1.186×10^{-2}	67.85	1.182×10^{-2}	75.94	1.274×10^{-2}	82.27	1.236×10^{-2}
(M_P, n)	(6,2)		(6,3)		(6,5)		(6,7)	
σ (fb)	88.1		80.9		84.6		95.2	
M_{BH}^{cut} (TeV)	S'	$\varepsilon^{M_{BH}^{cut}}$	S'	$\varepsilon^{M_{BH}^{cut}}$	S'	$\varepsilon^{M_{BH}^{cut}}$	S'	$\varepsilon^{M_{BH}^{cut}}$
1.0	9.661	1.097×10^{-2}	9.049	1.118×10^{-2}	10.04	1.187×10^{-2}	11.16	1.172×10^{-2}
2.0	9.661	1.097×10^{-2}	9.041	1.117×10^{-2}	10.04	1.187×10^{-2}	11.15	1.171×10^{-2}
3.0	9.617	1.092×10^{-2}	9.009	1.113×10^{-2}	10.00	1.183×10^{-2}	11.13	1.169×10^{-2}
4.0	9.547	1.084×10^{-2}	8.944	1.105×10^{-2}	9.918	1.173×10^{-2}	11.05	1.160×10^{-2}
5.0	9.415	1.069×10^{-2}	8.855	1.094×10^{-2}	9.782	1.157×10^{-2}	10.84	1.138×10^{-3}
(M_P, n)	(7,2)		(7,3)		(7,5)		(7,7)	
σ (fb)	11.8		10.9		11.4		12.9	
M_{BH}^{cut} (TeV)	S'	$\varepsilon^{M_{BH}^{cut}}$	S'	$\varepsilon^{M_{BH}^{cut}}$	S'	$\varepsilon^{M_{BH}^{cut}}$	S'	$\varepsilon^{M_{BH}^{cut}}$
1.0	1.095	9.28×10^{-3}	1.051	9.67×10^{-3}	1.094	9.58×10^{-3}	1.363	1.061×10^{-2}
2.0	1.095	9.28×10^{-3}	1.051	9.67×10^{-3}	1.094	9.58×10^{-3}	1.363	1.061×10^{-2}
3.0	1.092	9.25×10^{-3}	1.050	9.66×10^{-3}	1.094	9.58×10^{-3}	1.363	1.061×10^{-2}
4.0	1.067	9.21×10^{-3}	1.047	9.63×10^{-3}	1.087	9.52×10^{-3}	1.356	1.055×10^{-2}
5.0	1.076	9.12×10^{-3}	1.028	9.46×10^{-3}	1.072	9.39×10^{-3}	1.343	1.045×10^{-2}

Table 4.21: Number of signal events (S') passing all selection criteria for each mass point $(M_P, n) = \{5, 6, 7\} \times \{2, 3, 5, 7\}$. Selection efficiencies $\varepsilon^{M_{BH}^{cut}}$ are quoted for each lower cut-off M_{BH}^{cut}. The data is normalised to an integrated luminosity of $\int \mathcal{L}\, dt$=10 fb^{-1}.

(M_P, n)	(1,2)		(1,3)		(1,5)		(1,7)	
σ (fb)	2.41×10^7		2.11×10^7		2.12×10^7		2.24×10^7	
M_{BH}^{cut} (TeV)	$S'/\sqrt{B}$	$\int \mathcal{L}'_D dt(\text{fb}^{-1})$	$S'/\sqrt{B}$	$\int \mathcal{L}'_D dt(\text{fb}^{-1})$	$S'/\sqrt{B}$	$\int \mathcal{L}'_D dt(\text{fb}^{-1})$	$S'/\sqrt{B}$	$\int \mathcal{L}'_D dt(\text{fb}^{-1})$
1.0	4.43×10^4	3.0×10^{-5}	3.99×10^4	3.3×10^{-5}	3.75×10^4	3.5×10^{-5}	4.33×10^4	3.1×10^{-5}
2.0	4.92×10^4	3.8×10^{-5}	4.41×10^4	4.3×10^{-5}	4.07×10^4	4.6×10^{-5}	4.73×10^4	4.0×10^{-5}
3.0	3.12×10^4	8.7×10^{-5}	2.68×10^4	1.0×10^{-4}	2.42×10^4	1.1×10^{-4}	2.90×10^4	9.4×10^{-5}
4.0	7.45×10^4	2.7×10^{-4}	5.97×10^4	3.4×10^{-4}	6.80×10^4	3.0×10^{-4}	7.52×10^4	2.7×10^{-4}
5.0	4.60×10^4	1.2×10^{-3}	5.37×10^4	5.4×10^{-3}	5.74×10^4	9.8×10^{-4}	4.87×10^4	1.2×10^{-3}
(M_P, n)	(3,2)		(3,3)		(3,5)		(3,7)	
σ (fb)	4.11×10^4		3.70×10^4		3.81×10^4		4.24×10^4	
M_{BH}^{cut} (TeV)	$S'/\sqrt{B}$	$\int \mathcal{L}'_D dt(\text{fb}^{-1})$	$S'/\sqrt{B}$	$\int \mathcal{L}'_D dt(\text{fb}^{-1})$	$S'/\sqrt{B}$	$\int \mathcal{L}'_D dt(\text{fb}^{-1})$	$S'/\sqrt{B}$	$\int \mathcal{L}'_D dt(\text{fb}^{-1})$
1.0	98.4		91.5		97.8		109	
2.0	139		129		139		154	
3.0	192	1.4×10^{-2}	178	1.5×10^{-2}	191	1.4×10^{-2}	212	1.3×10^{-2}
4.0	942	2.1×10^{-2}	823	2.4×10^{-2}	917	2.2×10^{-2}	1027	2.0×10^{-2}
5.0	1130	5.0×10^{-2}	997	5.6×10^{-2}	1162	4.8×10^{-2}	1300	4.3×10^{-2}
(M_P, n)	(4,2)		(4,3)		(4,5)		(4,7)	
σ (fb)	4648		4233		4376		4883	
M_{BH}^{cut} (TeV)	$S'/\sqrt{B}$	$\int \mathcal{L}'_D dt(\text{fb}^{-1})$	$S'/\sqrt{B}$	$\int \mathcal{L}'_D dt(\text{fb}^{-1})$	$S'/\sqrt{B}$	$\int \mathcal{L}'_D dt(\text{fb}^{-1})$	$S'/\sqrt{B}$	$\int \mathcal{L}'_D dt(\text{fb}^{-1})$
1.0	8.32		9.14		9.40		10.5	
2.0	11.8		12.9		13.3		14.8	
3.0	16.9		18.6		19.1		21.3	
4.0	116	0.1531	127	0.1586	131	0.1537	146	0.1380
5.0	169	0.2935	189	0.2977	201	0.2795	224	0.2509

Table 4.22: Significance $\frac{S'}{\sqrt{B'}}$ and integrated discovery luminosity $\int \mathcal{L}'_D \, dt$ for mass points $(M_P, n) = \{1, 3, 4\} \times \{2, 3, 5, 7\}$ with 10 fb^{-1} of integrated luminosity.

(M_P, n)	(5,2)		(5,3)		(5,5)		(5,7)	
σ (fb)	625		572		594		671	
M_{BH}^{cut} (TeV)	$S'/\sqrt{B}$	$\int \mathcal{L}'_D dt(\text{fb}^{-1})$	$S'/\sqrt{B}$	$\int \mathcal{L}'_D dt(\text{fb}^{-1})$	$S'/\sqrt{B}$	$\int \mathcal{L}'_D dt(\text{fb}^{-1})$	$S'/\sqrt{B}$	$\int \mathcal{L}'_D dt(\text{fb}^{-1})$
1.0	1.11		1.02		1.12		1.24	
2.0	1.58		1.44		1.59		1.75	
3.0	2.27		2.07		2.29		2.52	
4.0	16.5		15.1		16.7		18.5	
5.0	41.9	1.345	38.2	1.474	42.7	1.317	46.3	1.216
(M_P, n)	(6,2)		(6,3)		(6,5)		(6,7)	
σ (fb)	88.1		81.1		84.7		95.0	
M_{BH}^{cut} (TeV)	$S'/\sqrt{B}$	$\int \mathcal{L}'_D dt(\text{fb}^{-1})$	$S'/\sqrt{B}$	$\int \mathcal{L}'_D dt(\text{fb}^{-1})$	$S'/\sqrt{B}$	$\int \mathcal{L}'_D dt(\text{fb}^{-1})$	$S'/\sqrt{B}$	$\int \mathcal{L}'_D dt(\text{fb}^{-1})$
1.0	0.128		0.120		0.133		0.194	
2.0	0.182		0.170		0.189		0.276	
3.0	0.261		0.245		0.272		0.396	
4.0	1.92		1.80		2.00		2.90	
5.0	5.30		4.98		5.51		8.28	
(M_P, n)	(7,2)		(7,3)		(7,5)		(7,7)	
σ (fb)	11.8		10.9		11.4		12.8	
M_{BH}^{cut} (TeV)	$S'/\sqrt{B}$	$\int \mathcal{L}'_D dt(\text{fb}^{-1})$	$S'/\sqrt{B}$	$\int \mathcal{L}'_D dt(\text{fb}^{-1})$	$S'/\sqrt{B}$	$\int \mathcal{L}'_D dt(\text{fb}^{-1})$	$S'/\sqrt{B}$	$\int \mathcal{L}'_D dt(\text{fb}^{-1})$
1.0	1.45×10^{-2}		1.39×10^{-2}		1.45×10^{-2}		1.81×10^{-2}	
2.0	2.06×10^{-2}		1.98×10^{-2}		2.06×10^{-2}		2.56×10^{-2}	
3.0	2.97×10^{-2}		2.85×10^{-2}		2.97×10^{-2}		3.71×10^{-2}	
4.0	0.219		0.211		0.219		0.272	
5.0	0.606		0.579		0.604		0.756	

Table 4.23: Significance $\frac{S'}{\sqrt{B'}}$ and integrated discovery luminosity $\int \mathcal{L}'_D \, dt$ for mass points $(M_P, n) = \{5, 6, 7\} \times \{2, 3, 5, 7\}$ with 10 fb^{-1} of integrated luminosity.

4.4.3 Conclusion

Sections 4.3.3 and 4.4 explored the black hole discovery potential with the ATLAS detector at the LHC, using the `CHARYBDIS` black hole generator and the `ATLFAST` fast simulation programme.

Using the fixed temperature, blackbody approximation to the black hole decay, the luminosity required for a 5σ discovery was found to be $< 1\text{fb}^{-1}$ for all mass points with $M_P < 5\text{TeV}$. These results suggest that if the fundamental Planck mass i sufficiently low, black holes may be one of the earliest signs of new physics observed at the LHC:

- if $M_P < 5$ TeV, discovery is achieved within less than one month of LHC running at low luminosity ($\int \mathcal{L} < 1\text{fb}^{-1}$)
- if $M_P < 4$ TeV, discovery is achieved within one day of LHC running at low luminosity ($\int \mathcal{L}1 < 0.1\text{fb}^{-1}$)
- if $M_P < 3$ TeV, discovery is achieved within only a few hours of LHC running at low luminosity

The discovery luminosity was also evaluated with a lower cut-off on the reconstructed black hole mass of $M_{BH}^{cut} = M_P + 1\text{TeV}$ to avoid the uncertainties of the regime of quantum gravity. In such cases, the numbers are increased by $\sim 30\%$ for $M_P = 1$ TeV, $\sim 60\%$ for $M_P = 3$ TeV and $\sim 90\%$ for $M_P = 4$ TeV. Even so, these values still suggest that discovery is achieved within a modest time of LHC running. However, these numbers should be treated with care, and their validity is discussed further in Section 4.5.

The discovery luminosities show a strong dependence on the fundamental Planck mass and a weak dependence on the dimensionality of spacetime. These dependencies are expected and reflect directly the variation in the black hole production cross section with respect to these parameters. The black hole cross section depends strongly on M_P and the sensitivity analysis suggests that the value of M_P is the determining factor for whether black holes will be discovered at the LHC.

Since the discovery luminosity is governed principally by the black hole cross section, modifications and improvements to the black hole decay spectra are not expected to modify these values significantly. However, since the black hole event triggering is sensitive to the number of final state events with energetic $e^{\pm}$ and γ, the combined effect of a time-evolving Hawking temperature and greybody modified spectra was studied and found to raise the discovery luminosity by

- $\sim$11% for mass points with M_P =1 TeV
- $\sim$27% for mass points with $M_P \geq$3 TeV$< M_P \leq$ 5 TeV

The slight increase may be attributed to a net decrease in the number of final states with energetic $e^{\pm}$ and γ. This reduction follows from the greybody modified photon emission probability.

4.5 Evaluation of Results

At this point, it is appropriate with a few comments concerning the scope and validity of the results presented in this chapter. Apart from the variety of different extra dimension models, there are a number of uncertainties which plague the theory of black hole production and decay presented in Section 1.3, some of which may affect the observability of black holes at the LHC and in particular the results of presented in this thesis. The LHC will provide a window into kinematic regions which remain unexplored to date. The lack of detailed understanding of physics at the highest energies offered by the LHC introduces yet other uncertainties to the results of this thesis.

The aim of this section is to highlight some of these uncertainties and where appropriate identify where partial improvements to the studies presented in this chapter can be made without further theoretical work.

4.5.1 Sensitivity results and the semi-classical limit

It is important to note that the sensitivity study presented in Section 4.3.3 was performed using simulated data with no lower threshold for black hole production

other than the fundamental Planck mass M_P. As was previously pointed out, the validity of the theory of black hole production and decay presented in Section 1.3 is restricted to the semi-classical regime $M_{BH} \gg M_P$. In the limit $M_{BH} \sim M_P$, the semi-classical approximation is expected to break down and quantum gravity effects become increasingly important. An analysis which makes use of the semi-classical calculation of the black hole cross section should arguably limit itself to the semi-classical regime. However, to retain consistency with (1), all signal samples used in the sensitivity study presented in Section 4.3.3 include generated black hole masses across the full region $M_{BH}^{gen} \geq M_P$, with the large majority of events at each point (M_P, n) having masses $M_{BH}^{gen} \sim M_P$.

In order to stay within the limits of the semi-classical regime, the discovery luminosity was evaluated also using the harder cut $M_{BH}^{cut} \geq M_P + 1\text{TeV}$ on the reconstructed black hole mass. This requirement was seen to produce a slight increase in the discovery luminosity. However, since the signal samples were generated with a black hole production threshold at M_P, they therefore still contain black holes with masses $M_{BH}^{rec} < M_P + 1\text{TeV}$. This is important because while the black hole is cross section strongly dependent on the value of M_P, it is also sensitive to the black hole production threshold through the ratio M_{BH}/M_P, as seen from Equation 4.19. It is perhaps a matter of discussion where the lower threshold should be set to stay within the confines of the semi-clasical approximation. It has been proposed that if $M_P = 1\text{TeV}$, then requiring $M_{BH}^{min} \leq 5\text{TeV}$ should render black hole analyses within safe limits of the semi-classical domain (11; 35). Such a requirement would give cross sections order of magnitude smaller than those listed in Tables 4.11 and 4.18. Table 4.24 compares cross sections obtained with three different production thresholds $M_{BH}^{min} = 1$ TeV, 5 TeV and 10 TeV, for fixed (M_P, n) =(1,3). The last two cross sections are seen to differ from the first by 3 and 7 orders of magnitude, respectively.

Using the cut-off M_{BH}^{cut} =5 TeV, Table C.4 predicts a discovery luminosity for black holes with (M_{BH}, M_P, n)=(5,1,3) on the order $\sim 0.1\text{pb}^{-1}$. However, judging from the production cross section for such black holes given in Table 4.24 the same data in Table C.4 indicate a discovery luminosity on the order $\sim 10\text{pb}^{-1}$.

Signal samples generated entirely within the semi-classical domain will give smaller cross sections for each mass point listed in Table 4.11. An analysis re-

M_P (TeV)	n	M_{BH}^{min} (TeV)	M_{BH}^{max} (TeV)	σ_{BH} (fb)
1	3	1	14	2.12×10^7
1	3	5	14	3.19×10^4
1	3	10	14	2.06

Table 4.24: Black hole cross sections with different lower thresholds M_{BH}^{min} relative to M_P =1 TeV.

stricted to the theoretically valid regime is therefore expected to give a more modest discovery potential.

However, one should remember that any production threshold different from the fundamental Planck mass will be artificial. Even though the semi-classical model may no longer be valid when $M_{BH} \sim M_P$, black hole production is not excluded in this region.

It is also worth noting that the Planck scale should be low for semi-classical black hole production to occur at the LHC. Judging from the experimental constraints on M_P presented in Section 1.2.3, it is likely that if black hole production occurs at the LHC, it will at the limit of the semi-classical approximation or perhaps entirely within the regime of quantum gravity.

4.5.2 Black hole production and decay

The sensitivity results presented in Section 4.3.3 were derived using the geometric cross section $\sigma_{BH} = F(n)\pi r_S^2$. The validity of this cross sections and possible suppression factors (37) have been widely debated in the literature. The consensus opinion seems to agree on its validity, however form factors $F(n)$ of order 1 are expected to modify the cross-section slightly. These have been calculated using numerical simulations (38). Throughout this thesis $F(n) = 1$ has been used, however the results of (38) may be introduced by hand to improve the sensitivity analysis.

Other issues are harder to improve on without further theoretical work (6). In particular, the `CHARYBDIS` black hole model assumes that all the energy of the incoming partons is captured in the black hole. A better understanding of transplanckian inelastic scattering and the amount of energy trapped behind

the horizon, may moderate the black hole discovery potential (39). It is also possible that the balding and spin-down phases will modify the energy spectrum of the decay, which may have a small effect on the discovery potential. Graviton emission to the bulk has been completely neglected in this thesis. Some estimates suggest that the fraction of energy emitted into the bulk may be as large as 50% (35). If this is combined with black hole decays to SUSY particles, it is likely that the p_T^{miss} distributions will be significantly modified with fewer events passing the selection requirement $p_T^{miss} < 100$ GeV.

It is also possible that other exotic processes will have signatures similar to black hole events, thus making it harder to distinguish the latter (40).

4.5.3 Parton distribution functions

Black hole production occurs in transplanckian scattering processes with large momentum transfers (Q^2) and where the colliding partons carry a large momentum fraction x of the momenta of the incoming protons. Our current understanding of the high Q^2, large x regions is limited and based on extrapolations from lower energy data obtained from current colliders, such as the Tevatron. The validity of such an extrapolation is questionable and the evolution equations may be significantly modified with the onset of TeV-scale gravity (15; 35). This will impact the cross section estimates for both black holes and SM background.

It is known that the CTEQ5L distributions used in this analysis underestimate the gluon contribution at high x. These modfications are incorporated into the new CTEQ6 distributions. A more detailed study of the black hole cross section dependence on different PDF's would be desireable. Any modifications to the black hole cross sections would necessarily impact the sensitivity results presented in this thesis.

4.5.4 QCD background

The uncertainties in the PDF's affect not only the black hole cross section, but also limits our understanding of the SM QCD background at the LHC. Hard QCD scattering processes have large cross sections at the LHC and is one of the dominant backgrounds to black hole events, as indicated in Table 4.13. For mass

points $(1, n)$, the black hole and hard QCD cross sections are comparable and a signal is clearly observed as an order of magnitude excess over the background. However, for higher values of M_P a more detailed understanding of the black hole cross section is required before black hole discovery can be declared. The scenario presented in Section 4.3.3 is also somewhat artificial. Transplanckian black hole production is a non-perturbative process which suppresses perturbative physics. Direct comparison to SM backgrounds will therefore be misleading.

4.5.5 Counting experiment

The black hole discovery potential at ATLAS was evaluated with a simple counting experiment and as such places an inordinate degree of trust on the Monte Carlo simulation. The many uncertainties, especially in the estimation of the QCD background, make such counting experiments less optimal at the LHC.

A better approach would be to fit the signal and background distributions shown in Figure 4.24, and use these fits to evaluate the black hole discovery potential. An initial attempt at this was made, but for lack of time, an analyses based on this approach could not be completed.

It should also be noted that such a fitting procedure would rely on the low end of the reconstructed mass distribution where $M_{BH}^{rec} \sim M_P$. In this region, the semi-classical model breaks down and quantum gravity effects become increasingly important. To develop a fitting procedure which avoids the uncertainties of this regime, is a considerably more difficult task.

The study presented in Sections 4.3.3 and 4.4 focused on the black hole discovery potential and not on the feasibility of measuring black hole properties. An underlying assumption has been that the excess over the SM background are black hole events. This assumption would need to be verified before discovery can be declared. Such verification would most likely have to be obtained through measurements of certain properties of the excess events and their interrelations. Intial studies were performed to this end, but could not be completed for lack of time.

4.5.6 Detector simulation

The entire study presented in this thesis has relied on he ATLFAST parametrization of the ATLAS detector. Given the large statistics required for many of the mass points (M_P, n) and background processes considered, the fast simulation has been indispensible. A similar study with fully simulated and reconstructed black hole events would be extremely time consuming. However, ATLFAST was developped primarily for the study of various SM and Higgs processes and is not optimized for the high enegy, high multiplicity characteristics of black hole events. In particular, the jet reconstruction algorithms are likely to be poor. Full simulation studies are therefore called for to validate the ATLFAST results. As such, black hole events provide an excellent means for exploring the performance of the ATLAS detector at high energies. They "probe" the electromagnetic and hadronic energy scales and require efficient and accurate jet reconstruction and tracking algorithms. Such studies are currently under way within the ATLAS collaboration (41).

A full simulation study would also be able to shed some light on effects that are likely to modify electron and photon efficiencies, such as jets faking electron signature or jets containing leading π^0 faking photon signature. Such effects would impact the sensitivity study presented in Section 4.3.3, as electrons and photons are used for black hole event triggering.

Chapter 5

Summary

Despite the many successes of the SM, there are strong reasons to believe that new physics will be revealed after the LHC becomes operational in 2007. One possibility is provided by extra dimension models where the fundamental Planck mass may be as low as a few TeV. If the fundamental Planck mass is sufficiently low, transplanckian energies will be accessible to the LHC and miniature black holes could be produced in hard scattering interactions.

This thesis has explored aspects of black hole production and decay within the context of the ATLAS experiment. A significant amount of time was invested in the interface of the `CHARYBDIS` black hole generator to the `PYTHIA` Monte Carlo program. This work led to the disclosure of an error in the `PYTHIA` subroutine `PYSHOW`.

A parton level study was subsequently performed to study the performance of the generator, as well as the nature of the black hole decay with different model parameters. A choice of parameters giving a low multiplicity of decay particles was found to significantly constrain the decay and alter expected event characteristics. The black hole events were then studied on the detector level, using the `ATLFAST` fast simulation of the ATLAS detector. Depending somewhat on the lower threshold for black hole production relative to the fundamental Planck mass and other model parameters, typical features of black hole events were found to include: large multiplicities ($\sim 8-20$), spherical event shapes, high $\sum p_T$ and low p_T^{miss}.

The black hole discovery potential at ATLAS was evaluated for various values of M_P and n, using a simple counting experiment. The results indicate that if $M_P < 5\text{TeV}$, the integrated luminosity for discovery is less than 1fb^{-1}. The sensitivity study was performed with both a fixed-temperature, blackbody approximation to the black hole decay and a more complete model with a time-evolving Hawking temperature and greybody emission spectra. The latter was evaluated found to raise the discovery luminosity with respect to the former by roughly $\sim 27\%$ for $M_P > 1\text{TeV}$.

Finally, various shortcoming of the analysis were highlighted and some possible improvements suggested.

Appendix A

A Note on Conventions

Several different definitions of the (fundamental) Planck mass are in use. While some conventions are directly related by constants of $\mathcal{O}(1)$, others vary with the number of extra dimensions n. Throughout this thesis, care has been taken to employ the default definition of the Planck mass as prescribed by the `MSSDEF`(=2) parameter of the `CHARYBDIS` black hole generator. This definition corresponds to the convention of Dimopoulos and Landsberg (19):

$$M_{P(4+n)}^{n+2} = \frac{1}{G_{(4)}} \frac{1}{(2\pi R)^n} \tag{A.1}$$

and whenever required, quoted results have been converted accordingly.

Appendix B

PYTHIA event listings

If no other mention is made, all listings below refer to the same event. The event is one that PYTHIA failed to handle.

B.1 Listing of black hole decay products

The output below provides a listing of the black hole decay products as they are fed into the HEPEUP common block. (To obtain the listing, a call to the PYTHIA function PYLIST(7) was introduced in the CHARYBDIS subroutine CHEVNT). Entries 1 and 2 are the black hole forming partons. All subseqent entries refer to particles of the black hole decay: entry number 3 refers to the first decay product, entry number 4 refers to the second, and so on.

```
          Event listing of user process at input (simplified)

    I IST     ID Mothers   Colours    p_x      p_y      p_z       E        m

    1 -1       2   0   0  500    0    0.000    0.000 3737.378 3737.378    0.000
    2 -1       1   0   0  502    0    0.000    0.000-4129.313 4129.313    0.000

    3  1      22   1   2  500    0  -93.308  107.164  195.945  242.043    0.000

          Event listing of user process at input (simplified)
```

I	IST	ID	Mothers		Colours		p_x	p_y	p_z	E	m
1	-1	2	0	0	500	0	0.000	0.000	3737.378	3737.378	0.000
2	-1	1	0	0	502	0	0.000	0.000	-4129.313	4129.313	0.000
3	1	22	1	2	500	0	-93.308	107.164	195.945	242.043	0.000
4	1	6	1	2	0	504	63.709	657.675	-132.408	696.241	175.000

.

.

etc

.

.

Event listing of user process at input (simplified)

I	IST	ID	Mothers		Colours		p_x	p_y	p_z	E	m
1	-1	2	0	0	500	0	0.000	0.000	3737.378	3737.378	0.000
2	-1	1	0	0	502	0	0.000	0.000	-4129.313	4129.313	0.000
3	1	22	1	2	500	0	-93.308	107.164	195.945	242.043	0.000
4	1	6	1	2	0	504	63.709	657.675	-132.408	696.241	175.000
5	1	21	1	2	0	0	416.929	129.264	656.578	788.438	0.000
6	1	3	1	2	0	0	287.173	44.857	2.155	290.664	0.500
7	1	-15	1	2	502	0	-151.646	-443.230	-514.978	696.172	1.777
8	1	1	1	2	0	0	162.338	-429.606	-385.432	599.560	0.330
9	1	3	1	2	0	0	-294.387	219.442	350.225	507.422	0.500
10	1	21	1	2	0	0	23.957	255.515	-44.930	260.539	0.000
11	1	16	1	2	504	0	-13.290	-327.192	-9.059	327.587	0.000
12	1	-24	1	2	0	0	-2.133	-177.222	-128.564	233.266	80.450
13	1	-15	1	2	506	0	547.511	-28.124	-625.379	831.662	1.777
14	1	21	1	2	0	513	-451.123	151.439	285.632	555.006	0.000
15	1	-2	1	2	508	0	-341.749	395.843	-256.148	582.319	0.330
16	1	6	1	2	510	0	-110.804	56.233	18.636	215.434	175.000

B.2 HEPEUP listing

The listing below shows the output of the HEPEUP common block after all particles shown in Appendix B.1 have been entered. The two last entries represent the decay products of the black hole remnant. In the below, IDUP gives the particle PDG code. PUP(5,I) represent the lab frame momentum (P_x, P_y, P_z, E, M) of the particle in units of GeV.

HEPEUP
User Process Event Common Block

NUP = 18
IDPRUP = 1
XWGTUP = 49.37526
SCALUP =7856.92090
AQEDUP = 0.00000
AQCDUP = 0.00000

IDUP	ISTUP	VTIMUP	SPINUP	MOTHUP(1)	MOTHUP(2)	ICOLUP(1)	ICOLUP(2)	PUP(1)	PUP(2)	PUP(3)	PUP(4)	PUP(5)
2	-1	0.0000	0.0000	0	0	501	0	0.00000	0.00000	3737.3778	3737.37778	0.00000
1	-1	0.0000	0.0000	0	0	504	0	0.00000	0.00000	-4129.3127	4129.31269	0.00000
22	1	0.0000	0.0000	1	2	0	0	-93.30814	107.16353	195.9449	242.04303	0.00000
6	1	0.0000	0.0000	1	2	500	0	63.70857	657.67452	-132.4077	696.24089	175.00000
21	1	0.0000	0.0000	1	2	501	500	416.92931	129.26429	656.5780	788.43772	0.00000
3	1	0.0000	0.0000	1	2	503	0	287.17342	44.85664	2.1554	290.66404	0.50000
-15	1	0.0000	0.0000	1	2	0	0	-151.64562	-443.22990	-514.9784	696.17168	1.77700
1	1	0.0000	0.0000	1	2	506	0	162.33841	-429.60591	-385.4316	599.56034	0.33000
3	1	0.0000	0.0000	1	2	509	0	-294.38726	219.44202	350.2255	507.42171	0.50000
21	1	0.0000	0.0000	1	2	504	503	23.95744	255.51463	-44.9300	260.53865	0.00000
16	1	0.0000	0.0000	1	2	0	0	-13.29048	-327.19222	-9.0588	327.58731	0.00000
-24	1	0.0000	0.0000	1	2	0	0	-2.13290	-177.22215	-128.5638	233.26613	80.45000
-15	1	0.0000	0.0000	1	2	0	0	547.51143	-28.12429	-625.3790	831.66206	1.77700
21	1	0.0000	0.0000	1	2	507	506	-451.12321	151.43865	285.6318	555.00569	0.00000
-2	1	0.0000	0.0000	1	2	0	507	-341.74862	395.84320	-256.1478	582.31930	0.33000
6	1	0.0000	0.0000	1	2	511	0	-110.80360	56.23340	18.6357	215.43426	175.00000
-6	1	0.0000	0.0000	1	2	0	509	72.61022	-242.61789	-287.4217	421.15549	175.00000
-3	1	0.0000	0.0000	1	2	0	511	-115.78897	-369.43852	483.2126	619.18218	0.50000

B.3 Final PYTHIA listing

The output below shows the event listing produced by PYTHIA before aborting the simulation. Entries 5 to 22 show the particles of the HEPEUP common block

reproduced in Appendix B.2. The components of the four-momenta are seen to differ due to ISR effects, sometimes by as much as > 100 GeV. The listing also discloses a `PYTHIA` bookkeeping error, (later corrected for in subversions 4.224 and above). The W^+ and b-quark shown in entries 33 and 34 both erroneously point to the t-quark of entry 20. The correct decay product of the t-quark are the W^+ and b-quark in entries 25 and 26.

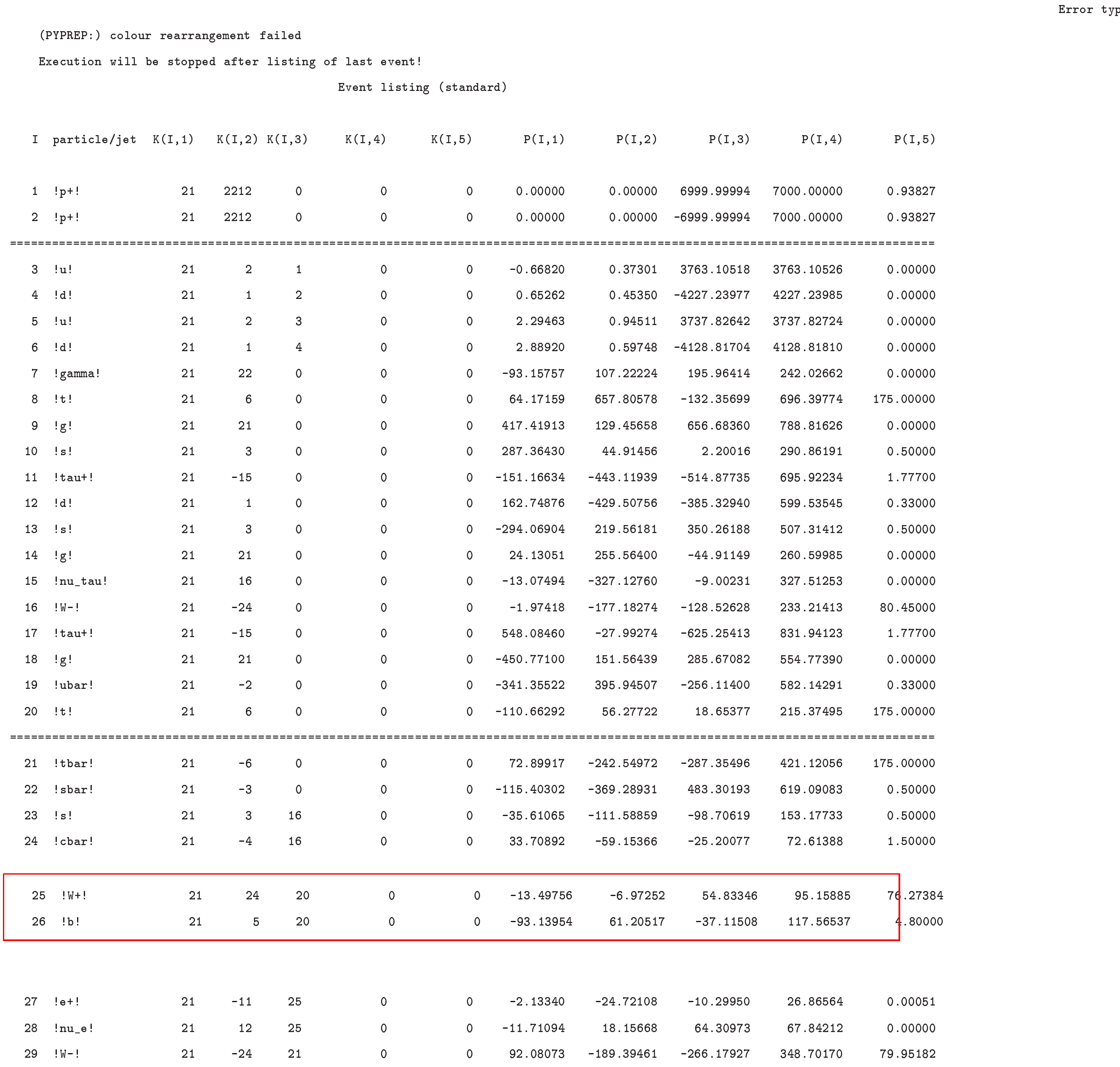

```
                                                                                                                    Error typ
 (PYPREP:) colour rearrangement failed
 Execution will be stopped after listing of last event!
                                          Event listing (standard)

 I  particle/jet  K(I,1)   K(I,2) K(I,3)     K(I,4)      K(I,5)       P(I,1)       P(I,2)       P(I,3)       P(I,4)       P(I,5)

 1  !p+!              21    2212      0          0           0      0.00000      0.00000   6999.99994   7000.00000      0.93827
 2  !p+!              21    2212      0          0           0      0.00000      0.00000  -6999.99994   7000.00000      0.93827
============================================================================================================================
 3  !u!               21       2      1          0           0     -0.66820      0.37301   3763.10518   3763.10526      0.00000
 4  !d!               21       1      2          0           0      0.65262      0.45350  -4227.23977   4227.23985      0.00000
 5  !u!               21       2      3          0           0      2.29463      0.94511   3737.82642   3737.82724      0.00000
 6  !d!               21       1      4          0           0      2.88920      0.59748  -4128.81704   4128.81810      0.00000
 7  !gamma!           21      22      0          0           0    -93.15757    107.22224    195.96414    242.02662      0.00000
 8  !t!               21       6      0          0           0     64.17159    657.80578   -132.35699    696.39774    175.00000
 9  !g!               21      21      0          0           0    417.41913    129.45658    656.68360    788.81626      0.00000
10  !s!               21       3      0          0           0    287.36430     44.91456      2.20016    290.86191      0.50000
11  !tau+!            21     -15      0          0           0   -151.16634   -443.11939   -514.87735    695.92234      1.77700
12  !d!               21       1      0          0           0    162.74876   -429.50756   -385.32940    599.53545      0.33000
13  !s!               21       3      0          0           0   -294.06904    219.56181    350.26188    507.31412      0.50000
14  !g!               21      21      0          0           0     24.13051    255.56400    -44.91149    260.59985      0.00000
15  !nu_tau!          21      16      0          0           0    -13.07494   -327.12760     -9.00231    327.51253      0.00000
16  !W-!              21     -24      0          0           0     -1.97418   -177.18274   -128.52628    233.21413     80.45000
17  !tau+!            21     -15      0          0           0    548.08460    -27.99274   -625.25413    831.94123      1.77700
18  !g!               21      21      0          0           0   -450.77100    151.56439    285.67082    554.77390      0.00000
19  !ubar!            21      -2      0          0           0   -341.35522    395.94507   -256.11400    582.14291      0.33000
20  !t!               21       6      0          0           0   -110.66292     56.27722     18.65377    215.37495    175.00000
============================================================================================================================
21  !tbar!            21      -6      0          0           0     72.89917   -242.54972   -287.35496    421.12056    175.00000
22  !sbar!            21      -3      0          0           0   -115.40302   -369.28931    483.30193    619.09083      0.50000
23  !s!               21       3     16          0           0    -35.61065   -111.58859    -98.70619    153.17733      0.50000
24  !cbar!            21      -4     16          0           0     33.70892    -59.15366    -25.20077     72.61388      1.50000

 25  !W+!              21      24     20          0           0    -13.49756     -6.97252     54.83346     95.15885     76.27384
 26  !b!               21       5     20          0           0    -93.13954     61.20517    -37.11508    117.56537      4.80000

27  !e+!              21     -11     25          0           0     -2.13340    -24.72108    -10.29950     26.86564      0.00051
28  !nu_e!            21      12     25          0           0    -11.71094     18.15668     64.30973     67.84212      0.00000
29  !W-!              21     -24     21          0           0     92.08073   -189.39461   -266.17927    348.70170     79.95182
```

```
 30  !bbar!          21    -5    21          0          0   -26.27077   -29.84165     4.78626    40.33145     4.80000
 31  !mu-!           21    13    29          0          0    83.95241   -85.14705  -127.02982   174.45519     0.10566
 32  !nu_mubar!      21   -14    29          0          0     3.66090   -96.96188  -127.84984   160.50105     0.00000

 33  !W+!            21    24    20          0          0    -2.05193   394.62249   -22.16302   403.25781    79.96589
 34  !b!             21     5    20          0          0    63.71905   229.09797  -104.03537   259.60045     4.80000

 35  !mu+!           21   -13    33          0          0    -0.22753   226.07782    23.38566   227.28425     0.10566
 36  !nu_mu!         21    14    33          0          0     1.90312   142.05953   -49.10319   150.31852     0.00000
101  (u)             14     2   119   0 119 105   0 119   0     2.29463     0.94511  3737.82642  3737.82724     0.00000
102  (d)             14     1   120   3 120 110   0 120   0     2.88920     0.59748 -4128.81704  4128.81810     0.00000
103  (gamma)         14    22     7   0   0 138   0   0 138   -93.15757   107.22224   195.96414   242.02662     0.00000
```

B.4 Effects of ISR, FSR and primordial $k_\perp$

The output below shows both a listing of the user process (call to `PYLIST(7)`) and excerpts of the final event listing (call to `PYLIST(1)`). The effects of ISR,FSR and primoridal $k_\perp$ are all switched off. The four-momental of the final listing are seen to agree perfectly with the "input" vlalues of the user process. Furthermore, the simulation did not abort, nor produce any error messages. (The event shown below therefore does not correspond to the event `PYTHIA` fails to handle).

```
          Event listing of user process at input (simplified)

  I IST     ID Mothers   Colours     p_x       p_y       p_z       E         m
  1 -1       2   0   0  500    0     0.000     0.000 3818.631 3818.631     0.000
  2 -1       2   0   0  503    0     0.000     0.000-4096.317 4096.317     0.000
  3  1     -12   1   2    0    0   307.091  -313.955   233.792  497.525     0.000
  4  1      -3   1   2  503  502   -24.995  -542.671   440.187  699.200     0.500
  5  1       4   1   2    0    0  -177.325   437.059   320.183  570.074     1.500
  6  1      21   1   2    0  505  -538.762  -146.108  -401.425  687.571     0.000
  7  1      24   1   2    0  508   -21.686   235.666  -151.689  292.388    80.450
  8  1       1   1   2  500    0  -224.081  -109.709   674.665  719.320     0.330
  9  1      21   1   2  502    0   -83.747   -59.266  -100.105  143.342     0.000
 10  1      21   1   2  508  507     4.198  -209.732   -34.360  212.570     0.000
 11  1       3   1   2    0    0   149.865   343.788   -57.575  379.428     0.500
 12  1      21   1   2  505    0    84.530-1089.577  -532.186 1215.543     0.000
 13  1      -1   1   2  507    0    33.814    47.294   253.044  259.638     0.330
```

```
 14  1     -14   1   2  509    0    1.318   -7.934 -158.864  159.068    0.000
 15  1       3   1   2  506    0  503.932  347.223 -160.982  632.793    0.500
 16  1       5   1   2  508    0  101.869  131.517 -463.860  492.812    4.800
 17  1      -3   1   2  509    0 -116.021  936.404 -138.512  953.677    0.500
-->Event # 100


                          Event listing (summary)

   I particle/jet KS     KF  orig    p_x      p_y      p_z       E        m

   1 !p+!         21    2212    0    0.000    0.000 7000.000 7000.000    0.938
   2 !p+!         21    2212    0    0.000    0.000-7000.000 7000.000    0.938
================================================================================
   3 !u!          21       2    1    0.000    0.000 3818.631 3818.631    0.000
   4 !u!          21       2    2    0.000    0.000-4096.317 4096.317    0.000
   5 !u!          21       2    3    0.000    0.000 3818.631 3818.631    0.000
   6 !u!          21       2    4    0.000    0.000-4096.317 4096.317    0.000
   7 !nu_ebar!    21     -12    0  307.091 -313.955  233.792  497.525    0.000
   8 !sbar!       21      -3    0  -24.995 -542.671  440.187  699.200    0.500
   9 !c!          21       4    0 -177.325  437.059  320.183  570.074    1.500
  10 !g!          21      21    0 -538.762 -146.108 -401.425  687.571    0.000
  11 !W+!         21      24    0  -21.686  235.666 -151.689  292.388   80.450
  12 !d!          21       1    0 -224.081 -109.709  674.665  719.320    0.330
  13 !g!          21      21    0  -83.747  -59.266 -100.105  143.342    0.000
  14 !g!          21      21    0    4.198 -209.732  -34.360  212.570    0.000
  15 !s!          21       3    0  149.865  343.788  -57.575  379.428    0.500
  16 !g!          21      21    0   84.530-1089.577 -532.186 1215.543    0.000
  17 !dbar!       21      -1    0   33.814   47.294  253.044  259.638    0.330
  18 !nu_mubar!   21     -14    0    1.318   -7.934 -158.864  159.068    0.000
  19 !s!          21       3    0  503.932  347.223 -160.982  632.793    0.500
  20 !b!          21       5    0  101.869  131.517 -463.860  492.812    4.800
  21 !sbar!       21      -3    0 -116.021  936.404 -138.512  953.677    0.500
  22 !dbar!       21      -1   11  -52.221  161.234 -104.939  199.338    0.330
  23 !u!          21       2   11   30.535   74.432  -46.750   93.050    0.330
================================================================================
  24 nu_ebar       1     -12    7  307.091 -313.955  233.792  497.525    0.000
```

```
25 (W+)         11      24   11  -21.686  235.666 -151.689  292.388   80.450
26 nu_mubar      1     -14   18    1.318   -7.934 -158.864  159.068    0.000
```

Appendix C

Discovery luminosity tables

The numbers and values listed in the following tables provide the basis for the comparison made in Section 4.4. All results refer to a fixed-temperature, black-body model of the black hole decay and an integrated luminosity of 10 fb^{-1}.

Background	qq		$t\bar{t}$		$W^{\pm}W^{\mp}$	
σ (fb)	1.28×10^7		4.88×10^5		467	
M_{BH}^{cut} (TeV)	B	$\varepsilon^{M_{BH}^{cut}}$	B	$\varepsilon^{M_{BH}^{cut}}$	B	$\varepsilon^{M_{BH}^{cut}}$
1.0	5136	4.0×10^{-5}	97.6	2.0×10^{-5}	0.14	3.0×10^{-5}
2.0	2568	2.0×10^{-5}	0	0	0.09	2.0×10^{-5}
3.0	1284	1.0×10^{-5}	0	0	0.05	1.0×10^{-5}
4.0	0	0	0	0	0	0
5.0	0	0	0	0	0	0
Background	$W^{\pm}Z^0$		Z^0Z^0		$\gamma\gamma$	
σ (fb)	2.57×10^4		1.05×10^4		2.12×10^5	
M_{BH}^{cut} (TeV)	B	$\varepsilon^{M_{BH}^{cut}}$	B	$\varepsilon^{M_{BH}^{cut}}$	B	$\varepsilon^{M_{BH}^{cut}}$
1.0	0	0	0	0	0	0
2.0	0	0	0	0	0	0
3.0	0	0	0	0	0	0
4.0	0	0	0	0	0	0
5.0	0	0	0	0	0	0
Background	$\gamma W^{\pm}, \gamma\gamma^*, \gamma Z^0$		$W^{\pm}q$		Zq, γ^*q	
σ (fb)	2.77×10^5		7.37×10^4		3.16×10^4	
M_{BH}^{cut} (TeV)	B	$\varepsilon^{M_{BH}^{cut}}$	B	$\varepsilon^{M_{BH}^{cut}}$	B	$\varepsilon^{M_{BH}^{cut}}$
1.0	0	0	7.37	1.0×10^{-5}	15.78	5.0×10^{-5}
2.0	0	0	7.37	1.0×10^{-5}	6.31	2.0×10^{-5}
3.0	0	0	7.37	1.0×10^{-5}	3.16	1.0×10^{-5}
4.0	0	0	7.37	1.0×10^{-5}	3.16	1.0×10^{-5}
5.0	0	0	0	0	3.16	1.0×10^{-5}
Background	γq		$b\bar{b}$		TOTAL	
σ (fb)	2.36×10^4		8.65×10^4			
M_{BH}^{cut} (TeV)	B	$\varepsilon^{M_{BH}^{cut}}$	B	$\varepsilon^{M_{BH}^{cut}}$	B	
1.0	407.93	1.73×10^{-3}	17.30	2.0×10^{-5}	5682.1	
2.0	228.73	9.70×10^{-4}	17.30	2.0×10^{-5}	2827.8	
3.0	58.95	2.50×10^{-4}	0	0	1353.5	
4.0	14.15	6.0×10^{-3}	0	0	24.7	
5.0	0	0	0	0	3.2	

Table C.1: Number of background events (B) passing all selection criteria. Numbers correspond to 10 fb^{-1} of integrated luminosity.

(M_P, n)	(1,2)		(1,3)		(1,5)		(1,7)	
σ (fb)	2.41×10^7		2.11×10^7		2.12×10^7		2.24×10^7	
M_{BH}^{cut} (TeV)	S	$\varepsilon^{M_{BH}^{cut}}$	S	$\varepsilon^{M_{BH}^{cut}}$	S	$\varepsilon^{M_{BH}^{cut}}$	S	$\varepsilon^{M_{BH}^{cut}}$
1.0	3.915×10^6	1.626×10^{-2}	3.323×10^6	1.572×10^{-2}	3.174×10^6	1.495×10^{-2}	3.529×10^6	1.508×10^{-2}
2.0	3.008×10^6	1.249×10^{-2}	2.490×10^6	1.178×10^{-2}	2.427×10^6	1.143×10^{-2}	2.663×10^6	1.138×10^{-2}
3.0	1.279×10^6	5.31×10^{-3}	1.030×10^6	4.870×10^{-3}	1.0318×10^6	4.86×10^{-3}	1.097×10^6	4.69×10^{-3}
4.0	4.17×10^5	1.73×10^{-3}	3.34×10^5	1.58×10^{-3}	3.67×10^5	1.73×10^{-3}	3.46×10^5	1.48×10^{-3}
5.0	1.28×10^5	5.3×10^{-4}	1.06×10^5	5.0×10^{-4}	1.06×10^5	5.0×10^{-4}	9.13×10^4	3.9×10^{-4}
(M_P, n)	(3,2)		(3,3)		(3,5)		(3,7)	
σ (fb)	4.11×10^4		3.70×10^4		3.81×10^4		4.24×10^4	
M_{BH}^{cut} (TeV)	S	$\varepsilon^{M_{BH}^{cut}}$	S	$\varepsilon^{M_{BH}^{cut}}$	S	$\varepsilon^{M_{BH}^{cut}}$	S	$\varepsilon^{M_{BH}^{cut}}$
1.0	9765	2.381×10^{-2}	8761	2.369×10^{-2}	9098	2.388×10^{-2}	10388	2.450×10^{-2}
2.0	9760	2.380×10^{-2}	8757	2.368×10^{-2}	9091	2.386×10^{-2}	10375	2.447×10^{-2}
3.0	9400	2.292×10^{-2}	8321	2.250×10^{-2}	8664	2.274×10^{-2}	9977	2.353×10^{-2}
4.0	5799	1.414×10^{-2}	5469	1.479×10^{-2}	5254	1.379×10^{-2}	6212	1.465×10^{-2}
5.0	2502	6.10×10^{-3}	2234	6.04×10^{-3}	2290	6.01×10^{-3}	2616	6.17×10^{-3}
(M_P, n)	(4,2)		(4,3)		(4,5)		(4,7)	
σ (fb)	4648		4233		4376		4883	
M_{BH}^{cut} (TeV)	S	$\varepsilon^{M_{BH}^{cut}}$	S	$\varepsilon^{M_{BH}^{cut}}$	S	$\varepsilon^{M_{BH}^{cut}}$	S	$\varepsilon^{M_{BH}^{cut}}$
1.0	922.2	1.984×10^{-2}	853.8	2.017×10^{-2}	910.6	2.081×10^{-2}	997.6	2.043×10^{-2}
2.0	921.7	1.983×10^{-2}	853.8	2.017×10^{-2}	908.9	2.077×10^{-2}	996.6	2.041×10^{-2}
3.0	918.0	1.975×10^{-2}	847.0	2.000×10^{-2}	901.5	2.060×10^{-2}	993.2	2.041×10^{-2}
4.0	858.5	1.847×10^{-2}	776.8	1.835×10^{-2}	828.4	1.893×10^{-2}	932.2	1.909×10^{-2}
5.0	457.4	9.84×10^{-3}	402.6	9.51×10^{-3}	424.9	9.71×10^{-3}	481.0	9.85×10^{-3}

Table C.2: Number of signal events (S) passing all selection criteria for each mass point $(M_P, n) = \{1, 3, 4\} \times \{2, 3, 5, 7\}$. Numbers correspond to 10 fb^{-1} of integrated luminosity.

(M_P, n)	(5,2)		(5,3)		(5,5)		(5,7)	
σ (fb)	625		572		594		671	
M_{BH}^{cut} (TeV)	S	$\varepsilon^{M_{BH}^{cut}}$	S	$\varepsilon^{M_{BH}^{cut}}$	S	$\varepsilon^{M_{BH}^{cut}}$	S	$\varepsilon^{M_{BH}^{cut}}$
1.0	107.3	1.718×10^{-2}	95.15	1.665×10^{-2}	102.5	1.725×10^{-2}	121.3	1.809×10^{-2}
2.0	107.3	1.218×10^{-2}	94.98	1.662×10^{-2}	102.4	1.723×10^{-2}	121.3	1.809×10^{-2}
3.0	106.6	1.706×10^{-2}	94.47	1.653×10^{-2}	101.9	1.715×10^{-2}	120.8	1.801×10^{-2}
4.0	105.5	1.689×10^{-2}	95.64	1.531×10^{-2}	101.0	1.699×10^{-2}	119.2	1.777×10^{-3}
5.0	95.64	1.531×10^{-2}	85.84	1.502×10^{-2}	90.38	1.521×10^{-2}	108.1	1.612×10^{-2}
(M_P, n)	(6,2)		(6,3)		(6,5)		(6,7)	
σ (fb)	88.1		81.1		84.7		95.0	
M_{BH}^{cut} (TeV)	S	$\varepsilon^{M_{BH}^{cut}}$	S	$\varepsilon^{M_{BH}^{cut}}$	S	$\varepsilon^{M_{BH}^{cut}}$	S	$\varepsilon^{M_{BH}^{cut}}$
1.0	13.03	1.479×10^{-2}	11.54	1.424×10^{-2}	12.35	1.457×10^{-2}	14.63	1.541×10^{-2}
2.0	13.02	1.478×10^{-2}	11.54	1.424×10^{-2}	12.35	1.457×10^{-2}	14.63	1.541×10^{-2}
3.0	13.00	1.475×10^{-2}	11.50	1.419×10^{-2}	12.31	1.453×10^{-2}	14.57	1.534×10^{-2}
4.0	12.93	1.467×10^{-2}	11.43	1.410×10^{-2}	12.25	1.446×10^{-2}	14.52	1.529×10^{-2}
5.0	12.71	1.442×10^{-2}	11.29	1.393×10^{-2}	12.13	1.431×10^{-2}	14.34	1.510×10^{-3}
(M_P, n)	(7,2)		(7,3)		(7,5)		(7,7)	
σ (fb)	11.8		10.9		11.4		12.8	
M_{BH}^{cut} (TeV)	S	$\varepsilon^{M_{BH}^{cut}}$	S	$\varepsilon^{M_{BH}^{cut}}$	S	$\varepsilon^{M_{BH}^{cut}}$	S	$\varepsilon^{M_{BH}^{cut}}$
1.0	1.487	1.256×10^{-2}	1.345	1.232×10^{-2}	1.572	1.224×10^{-2}	1.640	1.277×10^{-2}
2.0	1.487	1.256×10^{-2}	1.345	1.232×10^{-2}	1.572	1.224×10^{-2}	1.640	1.277×10^{-2}
3.0	1.485	1.254×10^{-2}	1.343	1.230×10^{-2}	1.572	1.224×10^{-2}	1.640	1.277×10^{-2}
4.0	1.480	1.250×10^{-2}	1.332	1.220×10^{-2}	1.563	1.217×10^{-2}	1.638	1.276×10^{-2}
5.0	1.468	1.240×10^{-2}	1.320	1.209×10^{-2}	1.551	1.208×10^{-2}	1.624	1.265×10^{-2}

Table C.3: Number of signal events (S) passing all selection criteria for each mass point $(M_P, n) = \{5, 6, 7\} \times \{2, 3, 5, 7\}$. Numbers correspond to 10 fb^{-1} of integrated luminosity.

(M_P, n)	(1,2)		(1,3)		(1,5)		(1,7)	
σ (fb)	2.41×10^7		2.11×10^7		2.12×10^7		2.24×10^7	
M_{BH}^{cut} (TeV)	$S/\sqrt{B}$	$\int \mathcal{L}_D\, dt(\text{fb}^{-1})$	$S/\sqrt{B}$	$\int \mathcal{L}_D\, dt(\text{fb}^{-1})$	$S/\sqrt{B}$	$\int \mathcal{L}_D\, dt(\text{fb}^{-1})$	$S/\sqrt{B}$	$\int \mathcal{L}_D\, dt(\text{fb}^{-1})$
1.0	5.20×10^4	2.6×10^{-5}	4.42×10^4	3.0×10^{-5}	4.22×10^4	3.2×10^{-5}	4.69×10^4	2.8×10^{-5}
2.0	5.67×10^4	3.2×10^{-5}	4.70×10^4	4.0×10^{-5}	4.57×10^4	4.1×10^{-5}	5.02×10^4	3.8×10^{-5}
3.0	3.47×10^4	7.8×10^{-5}	2.80×10^4	9.7×10^{-5}	2.80×10^4	9.7×10^{-5}	2.98×10^4	9.1×10^{-5}
4.0	8.33×10^4	2.40×10^{-4}	6.68×10^4	2.99×10^{-4}	7.35×10^4	2.72×10^{-4}	6.93×10^4	2.89×10^{-4}
5.0	7.37×10^4	1.40×10^{-4}	6.10×10^4	9.46×10^{-4}	6.13×10^4	9.42×10^{-4}	5.27×10^4	1.096×10^{-3}
(M_P, n)	(3,2)		(3,3)		(3,5)		(3,7)	
σ (fb)	4.11×10^4		3.70×10^4		3.81×10^4		4.24×10^4	
M_{BH}^{cut} (TeV)	$S/\sqrt{B}$	$\int \mathcal{L}_D\, dt(\text{fb}^{-1})$	$S/\sqrt{B}$	$\int \mathcal{L}_D\, dt(\text{fb}^{-1})$	$S/\sqrt{B}$	$\int \mathcal{L}_D\, dt(\text{fb}^{-1})$	$S/\sqrt{B}$	$\int \mathcal{L}_D\, dt(\text{fb}^{-1})$
1.0	130		116		121		138	
2.0	184		165		171		196	
3.0	255	1.064×10^{-2}	226	2.202×10^{-2}	235	1.154×10^{-2}	271	1.002×10^{-2}
4.0	1160	1.724×10^{-2}	1094	1.828×10^{-2}	1051	1.903×10^{-2}	1242	1.610×10^{-2}
5.0	1444	4.000×10^{-2}	1290	4.477×10^{-2}	1322	4.367×10^{-2}	1510	3.823×10^{-2}
(M_P, n)	(4,2)		(4,3)		(4,5)		(4,7)	
σ (fb)	4648		4233		4376		4883	
M_{BH}^{cut} (TeV)	$S/\sqrt{B}$	$\int \mathcal{L}_D\, dt(\text{fb}^{-1})$	$S/\sqrt{B}$	$\int \mathcal{L}_D\, dt(\text{fb}^{-1})$	$S/\sqrt{B}$	$\int \mathcal{L}_D\, dt(\text{fb}^{-1})$	$S/\sqrt{B}$	$\int \mathcal{L}_D\, dt(\text{fb}^{-1})$
1.0	12.3		11.3		12.1		13.3	
2.0	17.4		16.1		17.1		18.8	
3.0	24.9		23.0		24.5		27.0	
4.0	172	0.1165	155	0.1287	166	0.1207	186	0.1073
5.0	264	0.2186	232	0.2484	245	0.2353	278	0.2079

Table C.4: The significance $\frac{S}{\sqrt{B}}$ at mass points $(M_P, n) = \{1, 3, 4\} \times \{2, 3, 5, 7\}$ with 10 fb^{-1} of integrated luminosity. The discovery luminosity $\int \mathcal{L}_D\, dt$ is evaluated for all points where $M_{BH}^{cut} \geq M_P$ within the restricted parameter space $(M_P, n) = \{1, 3, 4, 5\} \times \{2, 3, 5, 7\}$.

(M_P, n)	(5,2)		(5,3)		(5,5)		(5,7)	
σ (fb)	625		572		594		671	
M_{BH}^{cut} (TeV)	$S/\sqrt{B}$	$\int \mathcal{L}_D dt(\text{fb}^{-1})$	$S/\sqrt{B}$	$\int \mathcal{L}_D dt(\text{fb}^{-1})$	$S/\sqrt{B}$	$\int \mathcal{L}_D dt(\text{fb}^{-1})$	$S/\sqrt{B}$	$\int \mathcal{L}_D dt(\text{fb}^{-1})$
1.0	1.43		0.130		1.36		1.61	
2.0	2.02		0.184		1.93		2.77	
3.0	2.90		0.264		2.77		3.28	
4.0	21.1		1.92		20.2		23.8	
5.0	55.2	1.046	50.2	1.165	52.2	1.107	62.4	0.9245

(M_P, n)	(6,2)		(6,3)		(6,5)		(6,7)	
σ (fb)	88.1		81.1		84.7		95.0	
M_{BH}^{cut} (TeV)	$S/\sqrt{B}$	$\int \mathcal{L}_D dt(\text{fb}^{-1})$	$S/\sqrt{B}$	$\int \mathcal{L}_D dt(\text{fb}^{-1})$	$S/\sqrt{B}$	$\int \mathcal{L}_D dt(\text{fb}^{-1})$	$S/\sqrt{B}$	$\int \mathcal{L}_D dt(\text{fb}^{-1})$
1.0	0.173		2.3×10^{-3}		0.164		0.194	
2.0	0.246		3.2×10^{-3}		0.233		0.276	
3.0	0.353		4.6×10^{-3}		0.335		0.396	
4.0	2.58		3.4×10^{-2}		2.45		2.90	
5.0	7.34		9.8×10^{-2}		7.00		8.28	

(M_P, n)	(7,2)		(7,3)		(7,5)		(7,7)	
σ (fb)	11.8		10.9		11.4		12.8	
M_{BH}^{cut} (TeV)	$S/\sqrt{B}$	$\int \mathcal{L}_D dt(\text{fb}^{-1})$	$S/\sqrt{B}$	$\int \mathcal{L}_D dt(\text{fb}^{-1})$	$S/\sqrt{B}$	$\int \mathcal{L}_D dt(\text{fb}^{-1})$	$S/\sqrt{B}$	$\int \mathcal{L}_D dt(\text{fb}^{-1})$
1.0	1.98×10^{-2}		1.45×10^{-5}		1.86×10^{-2}		2.18×10^{-2}	
2.0	2.80×10^{-2}		2.06×10^{-5}		2.64×10^{-2}		3.09×10^{-2}	
3.0	4.03×10^{-2}		2.97×10^{-5}		3.80×10^{-2}		4.46×10^{-2}	
4.0	0.296		2.18×10^{-4}		0.278		0.328	
5.0	0.848		6.30×10^{-4}		0.796		0.938	

Table C.5: The significance $\frac{S}{\sqrt{B}}$ at mass points $(M_P, n) = \{5, 6, 7\} \times \{2, 3, 5, 7\}$ with 10 fb^{-1} of integrated luminosity. The discovery luminosity $\int \mathcal{L}_D \, dt$ is evaluated for all points where $M_{BH}^{cut} \geq M_P$ within the restricted parameter space $(M_P, n) = \{5\} \times \{2, 3, 5, 7\}$.

Bibliography

[1] J.Tanaka, T.Yamamura, S.Asai, and J.Kanzaki, *Study of black holes at the ATLAS detector at the LHC*, hep-ph/0411095. ATL-PHYS-2003-037. 1, 4.3, 46, 2, 4.3.1.1, 4.3.1.1, 4.3.1.1, 4.3.1.2, 4.3.1.2, 4.3.2, 1, 1, 4.3.3, 4.3.3.1, 52, 4.4, 4.18, 4.5.1

[2] Y.Pylypchenko, *Study of χ_C production in pA interactions at HERA-B*. PhD thesis, University of Oslo, 2005. 1.1

[3] D. Collaboration, *A precision measurement of the mass of the top quark*, *Nature* **429** (2004) 638–642, [hep-ex/0406031]. 1.1.2, 1.1, 1.1.2

[4] S.-K. Collaboration, *Evidence for oscillation of atmospheric neutrinos*, *Phys.Rev.Lett.* **81** (1998) 1562–1567, [hep-ex/9807003]. 1.1.2

[5] S. Collaboration, *Direct evidence for neutrino flavor transformation from neutral-current interactions in the sudbury neutrino observatory*, *Phys.Rev.Lett.* **89** (2002) [nucl-ex/0204008]. 1.1.2

[6] C.M.Harris, *Physics Beyond the Standard Model: Exotic Leptons and Black Holes at Future Colliders*. PhD thesis, University of Cambridge, 2003. hep-ph/0502005. 1.2, 1.2.3, 1.3, 1, 15, 16, 1, 39, 4.1.2, 4.1.3.5, 4.5.2

[7] N.Arkani-Hamed, S.Dimopoulos, and G.Dvali, *The hierarchy problem and new dimensions at a millimeter*, *Phys.Lett.* **B429** (1998) 263–272, [hep-ph/9803315]. 1.2.2

[8] Y.Uehara, *A mini-review of constraints on extra dimensions*, *Mod.Phys.Lett* **A17** (2002) 1551–1558, [hep-ph/0203244]. 1.2.3

[9] S. et al.(Particle Data Group), *Extra dimensions*, *Phys.Rev* **B592** (2004) 1. 1.2.3

[10] M.J.Palmer, *Studies of Extra-Dimensional Models with the ATLAS Detector*. PhD thesis, University of Cambridge, 2005. 1.2.3

[11] P.Kanti, *Black Holes in Theories with Large Extra Dimensions: A Review*, *Int.J.Mod.Phys* **A19** (2004) 4899–4951, [hep-ph/0402168]. 1.3, 11, 1.3.2, 1, 1, 2, 3, 1, 15, 4.5.1

[12] S.B.Giddings and S.Thomas, *High Energy Colliders as Black Hole Factories: The End of Short Distance Physics*, *Phys.Rev.* **D65** (2000) 499–502, [hep-th/0003118]. 1.3, 1.3.3.1, 4, 18

[13] G.F.Guidice, R.Rattazzi, and J.D.Wells, *Transplanckian Collisions at the LHC and Beyond*, *Nucl.Phys.* **B630** (2002) 293–325, [hep-ph/0112161]. 1.3.1, 1.3.1

[14] R.Rattazzi, *Transplanckian collisions at future accelerators*, hep-ph/0205265. 1.3.1, 1.3.1

[15] S.Hossenfelder, *What black holes can teach us*, hep-ph/0412265. 1.3.1.1, 4, 4.5.3

[16] M.Cavagliá, *Black Hole and Brane Production in TeV Gravity: A Review*, *Int.J.Mod.Phys* **A18** (2003) 1843–1882, [hep-ph/0210296]. 11, 1.3.4

[17] R.Emparan, G.T.Horowitz, and R.C.Myers, *Black Holes Radiate Mainly on the Brane*, *Phys.Rev.Lett.* **85** (2000) 499–502. 13

[18] S.W.Hawking, *Particle creation by black holes*, *Commun.Math.Phys.* **43** (1975) 199–220. 1.3.3.2

[19] S.Dimopoulos and G.Landsberg, *Black Holes at the LHC*, *Phys.Rev.Lett* **87** (2001) 161602, [hep-ph/0106295]. 15, A

[20] F.Gianotti, *COLLIDER PHYSICS:LHC*, 2000. ATL-CONF-2000-001. 19, 2.2

[21] H.L.Lai, J.Huston, S.Kuhlmann, J.Morfin, F.Olness, J.F.Owens, J.Pumplin, and W.K.Tung, *Global QCD Analysis of Parton Structure of the Nucleon: CTEQ5 Parton Distributions*, *Eur.Phys.J.* **C12** (2000) 375–392. 2.3

[22] A. collaboration, *Atlas detector and physics performance, technical design report, vol.1*, *CERN/LHCC* **99-14** (1999). 2.4, 1

[23] C.Lester, *Model independent sparticle mass measurements at ATLAS*. PhD thesis, University of Cambridge, 2001. 2.2.2.2

[24] E.Lytken, *Prospects for Slepton Searches with ATLAS*. PhD thesis, University of Copenhagen, 2003. 1

[25] A. collaboration, *Calorimeter Performance Technical Design Report*, *CERN/LHCC* **96-40** (1997). 2.10, 2.11

[26] A. collaboration, *ATLAS Muon Spectrometer Technical Design Report*, *CERN/LHCC* **97-22** (1997). 2.13

[27] G. Collaboration, *Geant4: A simulation toolkit*, *Nuclear Instruments and Methods in Physics Research* **A506** (2003) 250–303. 3

[28] T.Sjöstrand, P.Edén, C.Friberg, L.Lönnblad, G.Miu, S.Mrenna, and E.Noorbin, *High-energy-physics Event Generation with PYTHIA 6.1*, *Comput.Phys.Commun.* **01** (2001) 238, [hep-ph/001001]. 23

[29] C.M.Harris, P.Richardson, and B. Webber, *Charybdis: A Black Hole Event generator*, *JHEP* **08** (2003) 033, [hep-ph/0307305]. 23, 26, 3.2.1, 3, 3.2.2, 1, 4.1.3.5, 4.3.1.1

[30] E.Richter-Was, D.Froidevaux, and L.Poggioli, *Atlafst 2.0: a fast simulation package for atlas*, *Tech.Rep.* (1998). ATL-PHYS-98-131. 23

[31] M. et al., *Les Houches Guidebook to Monte Carlo Generators for Hadron Collider Physics*, *Proceedings of the Workshop on Physics at TeV Colliders, Les Houches, France* (2003) [hep-ph/0403045]. 3.1

[32] G. et al., *Herwig 6: an event generation for Hadron Emission Reactions With Interfering Gluons (including supersymmetric processes)*, *JHEP* **01** (2001) 010, [hep-ph/0011363]. 3.2

[33] S.Dimopoulos and G.Landsberg *eConf* **C010630** (2001) P321. SNOWMASS-2001-P321. 3.2, 4.1.3.3, 2, 50

[34] E. et al., *Generic User Interface for Event Generators*, *Physics at TeV Colliders II Workshop, Les Houches, France* (May, 2001) [hep-ph/0109068]. 26, 32

[35] C.M.Harris, M.J.Palmer, M.A.Parker, P.Richardson, A.Sabetfakhri, and B.R.Webber, *Exploring Higher Dimensional Black Holes at the Large Hadron Collider*, hep-ph/0411022. ATL-COM-PHYS-2004-067. 27, 4.1.2, 4.1.3.5, 4.5.1, 4.5.2, 4.5.3

[36] B.K.Gjelsten, *Mass determination of supersymmetric particles in ATLAS*. PhD thesis, University of Oslo, 2005. 37

[37] M. Voloshin, *Semiclassical suppression of black hole production in particle collisions*, *Phys.Lett.* **B518** (2001) 137–142, [hep-ph/0107199]. 4.5.2

[38] H. Yoshino and Y. Nambu, *Black hole formation in the grazing collision of high-energy particles*, *Phys.Rev.* **D67** (2003) 024009, [gr-qc/0209003]. 4.5.2

[39] L.A.Anchordoqui, J.L.Feng, H.Goldberg, and A.D.Shapere, *Inelastic Black Hole Production and Large Extra Dimensions*, *Phys.Lett.* **B594** (2004) 363–367, [hep-ph/0311365]. 4.5.2

[40] S.Dimopoulos and R.Emparan, *String Balls at the LHC and Beyond*, *Phys.Lett.* **B526** (2002) 393–398, [hep-ph/0108060]. 4.5.2

[41] C. N.Brett, *Micro Black Holes in the ATLAS detector: Status Report*, May, 2005. Talk to ATLAS Exotics Working Group. 4.5.6